SANDIA REPORT

SAND2006-6180
Unlimited Release
Printed October 2006

Atomistic Modeling of Nanowires, Small-scale Fatigue Damage in Cast Magnesium, and Materials for MEMS

Ken Gall, Jiankuai Diao, Martin L. Dunn, Phil Gullett, Mark F. Horstemeyer, David C. Miller, David L. McDowell, Kevin Spark, Mellisa J. Talmage, Neil West, and Jonathan A. Zimmerman

Prepared by
Sandia National Laboratories
Albuquerque, New Mexico 87185 and Livermore, California 94550

Sandia is a multiprogram laboratory operated by Sandia Corporation,
a Lockheed Martin Company, for the United States Department of Energy's
National Nuclear Security Administration under Contract DE-AC04-94-AL85000.

Sandia National Laboratories

Issued by Sandia National Laboratories, operated for the United States Department of Energy by Sandia Corporation.

Available to DOE and DOE contractors from
U.S. Department of Energy
Office of Scientific and Technical Information
P.O. Box 62
Oak Ridge, TN 37831

Telephone: (865) 576-8401
Facsimile: (865) 576-5728
E-Mail: reports@adonis.osti.gov
Online ordering: http://www.doe.gov/bridge

Available to the public from
U.S. Department of Commerce
National Technical Information Service
5285 Port Royal Rd
Springfield, VA 22161

Telephone: (800) 553-6847
Facsimile: (703) 605-6900
E-Mail: orders@ntis.fedworld.gov
Online order: http://www.ntis.gov/help/ordermethods.asp?loc=7-4-0#online

SAND2006-6180
Unlimited Release
Printed October 2006

Atomistic Modeling of Nanowires, Small-scale Fatigue Damage in Cast Magnesium, and Materials for MEMS

Ken Gall and David L. McDowell
George Woodruff School of Mechanical Engineering
Georgia Institute of Technology
Atlanta, Georgia 30332

Jiankuai Diao, Martin L. Dunn, David C. Miller,
Mellisa J. Talmage, Kevin Spark and Neil West
Department of Mechanical Engineering
University of Colorado
Boulder, Colorado 80309

Phil Gullett
Department of Civil Engineering

Mark F. Horstemeyer
Department of Mechanical Engineering

Mississippi State University
Mississippi State, Mississippi 39762

Jonathan A. Zimmerman
Mechanics of Materials Department 8776
Sandia National Laboratories
Livermore, California 94551-0969

Abstract

Lightweight and miniaturized weapon systems are driving the use of new materials in design such as microscale materials and ultra low-density metallic materials. Reliable design of future weapon components and systems demands a thorough understanding of the deformation modes in these materials that comprise the components and a robust methodology to predict their performance during service or storage. Traditional continuum models of material deformation and failure are not easily extended to these new materials unless microstructural characteristics are included in the formulation. For example, in LIGA Ni and Al-Si thin films, the physical size is on the order of microns, a scale approaching key microstructural features. For a new potential structural material, cast Mg offers a high stiffness-to-weight ratio, but the microstructural heterogeneity at various scales requires a structure-property continuum model. Processes occurring at the nanoscale and microscale develop certain structures that drive material behavior.

The objective of the work presented in this report was to understand material characteristics in relation to mechanical properties at the nanoscale and microscale in these promising new material systems. Research was conducted primarily at the University of Colorado at Boulder to employ tightly coupled experimentation and simulation to study damage at various material size scales under monotonic and cyclic loading conditions. Experimental characterization of nano/micro damage will be accomplished by novel techniques such as in-situ environmental scanning electron microscopy (ESEM), 1 MeV transmission electron microscopy (TEM), and atomic force microscopy (AFM). New simulations to support experimental efforts will include modified embedded atom method (MEAM) atomistic simulations at the nanoscale and single crystal micromechanical finite element simulations.

This report summarizes the major research and development accomplishments for the LDRD project titled "Atomistic Modeling of Nanowires, Small-scale Fatigue Damage in Cast Magnesium, and Materials for MEMS". This project supported a strategic partnership between Sandia National Laboratories and the University of Colorado at Boulder by providing funding for the lead author, Ken Gall, and his students, while he was a member of the University of Colorado faculty.

Acknowledgements

Funding for K. Gall was provided by the DOE Presidential Early Career Award for Scientists and Engineers (PECASE) award from Sandia National Laboratories, supported by the US Department of Energy under contract DE-AC04-94Al85000.

Contents

Intentionally Left Blank

1 Introduction

This report summarizes the major research and development accomplishments for the LDRD project titled "Atomistic Modeling of Nanowires, Small-scale Fatigue Damage in Cast Magnesium, and Materials for MEMS". This project supported a strategic partnership between Sandia National Laboratories and the University of Colorado at Boulder by providing funding for the lead author, Ken Gall, and his students, while he was a member of the University of Colorado faculty.

Lightweight and miniaturized weapon systems are driving the use of new materials in design such as microscale materials and ultra low-density metallic materials. Reliable design of future weapon components and systems demands a thorough understanding of the deformation modes in these materials that comprise the components and a robust methodology to predict their performance during service or storage. Traditional continuum models of material deformation and failure are not easily extended to these new materials unless microstructural characteristics are included in the formulation. For example, in LIGA Ni and Al-Si thin films, the physical size is on the order of microns, a scale approaching key microstructural features. For a new potential structural material, cast Mg offers a high stiffness-to-weight ratio, but the microstructural heterogeneity at various scales requires a structure-property continuum model. Processes occurring at the nanoscale and microscale develop certain structures that drive material behavior.

The objective of the work presented in this report was to understand material characteristics in relation to mechanical properties at the nanoscale and microscale in these promising new material systems. Research was conducted primarily at the University of Colorado at Boulder to employ tightly coupled experimentation and simulation to study damage at various material size scales under monotonic and cyclic loading conditions. Experimental characterization of nano/micro damage will be accomplished by novel techniques such as in-situ environmental scanning electron microscopy (ESEM), 1 MeV transmission electron microscopy (TEM), and atomic force microscopy (AFM). New simulations to support experimental efforts will include modified embedded atom method (MEAM) atomistic simulations at the nanoscale and single crystal micromechanical finite element simulations.

The content of this report consists of selected articles that describe research performed for this project, and that have been published in peer-reviewed, technical journals. Chapter 2 presents the article "In-Situ Observations of High Cycle Fatigue Mechanisms in Cast AM60B Magnesium in Vacuum and Water Vapor Environments" by K. Gall, G. Biallas, H. J. Maier, P. Gullet, M. F. Horstemeyer, D. L. McDowell, and J. Fan, published in the *International Journal of Fatigue*, vol. 26, no. 1, pp. 59-70, 2004. Chapter 3 presents the article "Creep of Thin Film Au on Au/Si Microcantilevers" by K. Gall, N. West, K. Spark, M. L. Dunn, and D. Finch, published in *Acta Materialia*, vol. 52, no. 8, pp. 2133-2146, 2004. Chapter 4 presents the article "The Strength of Gold Nanowires" by K. Gall, J. Diao, and M. L. Dunn, published in *Nanoletters*, vol. 4, no. 12, pp. 2431-2436, 2004. Chapter 5 presents the article "Atomistic Simulations of the Yielding of Gold

Nanowires" by J. Diao, K. Gall, M. L. Dunn, and J. A. Zimmerman, published in *Acta Materialia*, vol. 54, pp. 643-653, 2006. Finally Chapter 6 presents the article "Incipient Yielding Behavior During Indentation for Gold Thin Films Before and After Annealing" by D. C. Miller, M. J. Talmage, and K. Gall, which has been accepted for publication in the *Journal of Materials Research.*

A complete list of papers that were written and/or published while Ken Gall was supported by the LDRD funding for this project is as follows:

D. C. Miller, W. L. Hughes, Z. L. Wang, K. Gall, and C. R. Stoldt (2006) Mechanical Effects of Galvanic Corrosion on Structural Polysilicon. In Press *Journal of MicroElectroMechanical Systems.*

M. Haftel and K. Gall (2006) Density Functional Theory Investigation of Surface-Stress Induced Phase Transformations in FCC Metal Nanowires. In Press *Physical Review B.*

D. C. Miller, M. J. Talmage, and K. Gall (2006) Incipient Yielding Behavior During Indentation for Gold Thin Films Before and After Annealing. In Press *Journal of Materials Research.*

M. K. Tripp, C. Stampfer, D. C. Miller, T. Helbling, C. F. Herrmann, C. Hierold, K. Gall, S. M. George and V. M. Bright (2006) The mechanical properties of atomic layer deposited alumina for use in micro- and nano-electromechanical systems. In Press *Sensors and Actuators A*

D. Miller, C. F. Hermann, H. J. Maier, S. M. George, C. Stoldt, and K. Gall (2006) Thermo-Mechanical Stability of Thin Film Multilayers: Part II Microstructure Evolution. In Press *Thin Solid Films.*

D. Miller, C. F. Hermann, H. J. Maier, S. M. George, C. Stoldt, and K. Gall (2006) Thermo-Mechanical Stability of Thin Film Multilayers: Part I Mechanical Behavior of Au/Cr/Si Microcantilevers. In Press *Thin Solid Films.*

C. P. Frick, K. Spark, T. Lang, and K. Gall (2006) Stress-Induced Martensitic Transformations and Shape Memory at Nanometer Scales. *Acta Materialia*, vol. 54, pp. 2223-2234.

H. S. Park, K. Gall, and J. A. Zimmerman (2006) Deformation of FCC Nanowires by Twinning and Slip. *Journal of The Mechanics and Physics of Solids,* vol. 54, pp. 1862-1881.

J. Diao, K. Gall, M. L. Dunn, and J. A. Zimmerman (2006) Atomistic Simulations of the Yielding of Gold Nanowires. *Acta Materialia*, vol. 54, pp. 643-653.

H. S. Park, K. Gall, and J. A. Zimmerman (2005) Shape Memory and Pseudoelasticity in Metal Nanowires. *Physical Review Letters*, vol. 95, 255504.

K. Gall, J. Diao, M. L. Dunn, M. Haftel, N. Bernstein, and M. J. Mehl (2005) Tetragonal Phase Transformation in Gold Nanowires, *Journal of Engineering Materials and Technology*, vol. 127, pp. 417-422.

K. Gall, G. Biallas, H. J. Maier, M. F. Horstemeyer, and D. L. McDowell (2005) Environmentally Influenced Microstructurally Small Fatigue Crack Growth in Cast Magnesium. *Materials Science and Engineering A*, vol. 396, pp. 143-154.

D. Miller, C. F. Hermann, H. J. Maier, S. M. George, C. Stoldt, and K. Gall (2005) Intrinsic Stress Development and Microstructure Evolution of Au/Cr/Si Multilayer Thin Films Subject to Annealing. *Scripta Materialia*, vol. 52, no. 9, pp. 873-879.

K. Gall, J. Diao, and M. L. Dunn (2004) The Strength of Gold Nanowires. *Nanoletters*, vol. 4, no. 12, pp. 2431-2436.

J. Diao, K. Gall, and M. L. Dunn (2004) Yield Strength Asymmetry in Metal Nanowires. *Nanoletters*, vol. 4, no. 10, pp. 1863-1867.

J. Diao, K. Gall and M. L. Dunn (2004) Surface Stress Driven Reorientation of Gold Nanowires. *Physical Review B*, vol. 70, 075413.

J. Diao, K. Gall and M. L. Dunn (2004) Atomistic Simulation of the Structure and Elastic Properties of Gold Nanowires. *Journal of the Mechanics and Physics of Solids*, vol. 52, no. 9, pp. 1935-1962.

G. Biallas, H. J. Maier, M. Essert, and K. Gall (2004) In-Situ Studies of Short Crack Growth Behavior in Cast AM60B Magnesium. *Materialprüfung (Materials Testing),* vol. 46, no. 7-8, pp. 384-388

K. Gall, N. West, K. Spark, M. L. Dunn, and D. Finch (2004) Creep of Thin Film Au on Au/Si Microcantilevers. *Acta Materialia*, vol. 52, no. 8, pp. 2133-2146.

M. F. Horstemeyer, N. Yang, K. Gall, D. L. McDowell, J. Fan, and P. Gullet (2004) High Cycle Fatigue of a Die Cast AZ91E-T4 Magnesium Alloy. *Acta Materialia,* vol. 52, no. 5, pp. 1327-1336.

K. Gall, G. Biallas, H. J. Maier, P. Gullet, M. F. Horstemeyer, and D. L. McDowell (2004) In-Situ Observations of Low-Cycle Fatigue Damage in Cast AM60B Magnesium in an Environmental Scanning Electron Microscope. *Metallurgical and Materials Transactions A*, vol. 35, no. 1, pp. 321-331.

K. Gall, G. Biallas, H. J. Maier, P. Gullet, M. F. Horstemeyer, D. L. McDowell, and J. Fan (2004) In-Situ Observations of High Cycle Fatigue Mechanisms in Cast AM60B Magnesium in Vacuum and Water Vapor Environments. *International Journal of Fatigue*, vol. 26, no. 1, pp. 59-70.

J. Diao, K. Gall and M. L. Dunn (2003) Surface-Stress-Induced Phase Transformation in Metal Nanowires. *Nature Materials*, vol. 2, no. 10, pp. 656-660.

2 In-Situ Observations of High Cycle Fatigue Mechanisms in Cast AM60B Magnesium in Vacuum and Water Vapor Environments

We present in-situ scanning electron microscopy (SEM) observations regarding the formation and propagation of small fatigue cracks in cast AM60B magnesium. Using an environmental SEM, observations were made in vacuum and in the presence of water vapor at 20 Torr. In the vacuum environment, fatigue cracks in the magnesium formed preferentially at pores, sometimes precluded by observable cyclic slip accumulation. At higher cycle numbers in the vacuum environment, additional cracks were discovered to initiate at persistent slip bands within relatively large magnesium dendrite cells. The propagation behavior of small fatigue cracks ($a < 6$ to 10 dendrite cells) was found to depend strongly on both environment and microstructure. Small fatigue cracks in the magnesium cycled under vacuum were discovered to propagate along interdendritic regions, along crystallographic planes, and through the dendrite cells. The preference to choose a given path is driven by the presence of microporosity, persistent slip bands, and slip incompatibilities between adjacent dendrite cells. Fatigue cracks formed more rapidly at certain locations in the water vapor environment compared to the vacuum environment, leading to a smaller total number of cracks in the water vapor environment. The majority of small cracks in magnesium cycled in the water vapor environment propagated straight through the dendrite cells, at a faster rate than the cracks in the vacuum. In the water vapor environment, cracks were observed to grow less frequently through interdendritic regions, even in the presence of microporosity, and cracks did not grow via persistent slip bands. The propagation behavior of slightly larger fatigue cracks ($a > 6$ to 10 dendrite cells) was found to be Mode I-dominated in both environments.

2.1 Introduction

Ongoing interest in the use of cast magnesium (Mg) alloys in the auto industry [1,2] has recently triggered substantial research effort focused on the structural properties of this metal. The very low density (1.8 g/cm^3), excellent castability, and easy machinability of Mg [2] make it a strong candidate for intricate lightweight components. One drawback of Mg-based castings is their sensitivity to various urban and industrial environments [3,4]. However, recent studies have linked the corrosion mechanisms in cast Mg to the microstructure, indicating that significant potential exists to improve their performance in corrosive environments [5-7]. Alternatively, coatings for Mg [8, 9] may be used to eliminate surface reactions and circumvent corrosion altogether. In parallel with these fundamental studies to model and prevent corrosion in cast Mg, it is necessary to examine the fatigue behavior of this class of materials. In the absence of corrosion, fatigue inevitably emerges as the dominant failure mode for Mg castings under cyclic loading conditions.

Compared to other lightweight wrought and cast materials such as aluminum and titanium alloys, very little work has been performed to characterize the fatigue mechanisms operating in cast Mg alloys. Initial studies examined the low and high cycle fatigue of cast Mg alloys to determine parameters for traditional fatigue life prediction methodologies [10-12]. The authors in [10-12] concluded that traditional fatigue life prediction tools were sometimes inaccurate for cast Mg alloys. Fatigue crack growth studies have shown that the propagation behavior of large fatigue cracks in Mg is strongly dependent on the environment [13-14]. Higher humidity environments have a tendency to reduce fatigue crack growth thresholds and increase fatigue crack growth rates. More recent studies have begun to examine the relationship between the microstructure and fatigue mechanisms in cast Mg alloys [15-18]. As observed in other cast materials, several studies have linked the formation of fatigue cracks in cast Mg to large pores [15-17]. In addition, several preliminary efforts have related the fatigue crack growth behavior to the microstructure of cast Mg using fracture surface observations [17] or specimen replication techniques [18]. Although preliminary studies have uncovered the basic microstructural aspects of the fatigue of cast Mg alloys, they have not provided detailed information on the mechanisms of crack formation and small crack propagation. In order to successfully develop microstructure- and mechanism-based models of fatigue in cast Mg alloys, it is imperative to understand these early stages of fatigue.

In the present paper we employ *in-situ* fatigue tests conducted in a scanning electron microscope equipped with a small-scale load frame (*in-situ* SEM) to examine the early stages of the fatigue process in cast AM60B Mg. The SEM has an environmental chamber and is capable of imaging at various humidity levels. Here we compare fatigue mechanisms in cast magnesium observed in a vacuum and under water vapor at 20 Torr. We focus on the formation and growth of small fatigue cracks within the microstructure in these different environments. Previous investigators [19-23] have demonstrated that *in-situ* SEM is a useful tool for investigating the behavior of small fatigue cracks. One drawback of earlier *in-situ* SEM studies has been the limitations imposed by the high vacuum required for imaging. With the advent of environmental SEM a few years ago, this is no longer an issue. In principle, it is possible to determine quantitative aspects of formation and growth behavior such as cycles to initiation, growth rates, and crack opening levels. However, in this paper we will focus on qualitative observations of operative crack formation and small crack growth mechanisms. Future investigations will consider quantitative aspects of formation and growth, although the present observations are sufficient to motivate initial micro-mechanical fatigue models for better quantification of the relevant phenomena.

2.2 Materials and Experimental Methods

A plate of AM60B magnesium with dimensions of 10 cm by 15 cm by 3 mm was cast in a permanent mold by high-pressure die-casting. The nominal composition of AM60B Mg is provided in Table 2.1.

Table 2.1. Chemical composition of AM60B Mg alloy. Values in weight percent.

Mg	**Al**	**Mn**	**Si**	**Zn**	**Fe**	**Cu**	**Ni**	**Other**
Bal.	5.5-6.5	0.25 min	0.10 max	0.22 max	0.005 max	0.010 max	0.002 max	0.003 max (total)

Flat dog-bone shaped specimens with a 8 mm gage length and a 3 mm by 1-2 mm gage cross section were machined from the plate at various spatial locations. Results will be presented here from *in-situ* tests on two specimens from similar regions of the plate where there is low overall porosity due to high cooling rates. One of the samples was cycled in high vacuum while the other sample was cycled in water vapor at 20 Torr. A third specimen was also extracted from a low porosity region to determine yield and tensile strength under monotonic loading. Numerous other samples have been tested to develop appropriate visualization parameters for *in-situ* fatigue testing of Mg. In addition, several different samples were tested to verify the generality of the present observations. Samples cycled under identical conditions all showed the same qualitative behaviors reported here.

In order to minimize the area that needs to be inspected during testing, small stress concentrations were employed in order to elevate the stresses and favor crack formation in a local region. One stress raiser, used in both fatigue samples, was a dimple with a 3 mm diameter and 120 μm maximum depth placed in the center of the specimen using a dimple grinder which produces low residual stresses. A small spot weld placed in the center of the dimple was used as an additional stress raiser in the sample to be cycled in the vacuum environment. In the sample with the spot weld, cracks were still observed to form away from the artificial defect. Clearly, this indicates that microstructural heterogeneities such as pores cause severe stress concentrations, and/or exist at locations with diminished material fatigue resistance. It should be made clear that the stress concentration in the sample cycled in high vacuum (dimple plus spot weld) was more severe than the stress concentration in the sample cycled in water vapor (dimple).

For *in-situ* observation, the surface of the Mg samples must be polished to successfully detect and track small-scale fatigue damage. A mild etching procedure, either during or after polishing, can be used to remove polishing-induced artifacts and highlight the cast Mg microstructure. However, over-etching of the cast Mg results in a deep microstructure that is unsuitable for *in-situ* observations. Due to the reactivity of Mg, numerous attempts were made to achieve the optimal surface for *in-situ* observations. The optimal preparation was achieved by first grinding with a 4,000 grit (5 μm) SiC abrasive and a 1:3 glycerine-ethanol solution. The sample was then subsequently polished with a series of 3 μm and 1 μm diamond pastes with excessive lubricant. The final polish was performed with a SiO_2 suspension (OPS), which serves as a combined mechanical polishing and chemical etching solution.

Mechanical tests were performed using a small-scale load frame fixed within an environmental SEM. The load frame has a maximum load capacity of 10 kN and a displacement range of 50 mm. The SEM was operated at an accelerating voltage of 20 kV and with two different environments during fatigue testing (a) a relatively high vacuum of $p < 10^{-3}$ Pa (7.4 x 10^{-6} Torr) and (b) water vapor at 2.7 x 10^{3} Pa (20 Torr). The water vapor at 20 Torr corresponds to 100% relative humidity at ambient room temperature conditions. Local chemical composition was determined with Energy Dispersive X-ray (EDX) analysis. *In-situ* tests conducted in the SEM do not provide significantly more resolution as compared to other techniques such as replica methods [18], but allow both EDX analysis and imaging using backscattered electrons that can provide additional microstructural information. Completely reversed ($R = \sigma_{min}/\sigma_{max} = -1$) fatigue tests were performed at a displacement rate of 20 μm/s. Gross tensile and compressive load limits were imposed and the machine was programmed to reverse the loading at these limits. The tensile test was performed at a displacement rate of 0.5 μm/s until complete fracture of the specimen. The yield and tensile strengths of the AM60B specimen machined from a low porosity region were measured to be 150 MPa and 285 MPa, respectively.

At the maximum displacement rate, the machine is capable of applying approximately 5,000 cycles per day, so a fatigue test lasting 10^{6} cycles would take 200 days. In order to accelerate the fatigue process and enhance the possibility of multiple crack formation sites, a nominal cyclic stress amplitude of 135 MPa (Amplitude 1) was applied until the first cracks could be detected. At this amplitude, the first cracks could be observed after preloading to 100 and 130 cycles in water vapor and high-vacuum environments, respectively. Following this pre-cycling, the nominal stress amplitude was decreased to 90 MPa (Amplitude 2) and kept constant during further cycling. We should mention that the pre-cycling procedure at higher amplitude will elevate local cyclic plastic strain levels, which may influence the fatigue processes operating at the subsequent lower amplitude. Extensive SEM observations were made in irregular intervals depending on the progression of fatigue damage. All SEM imaging was performed at the maximum tensile load to accentuate crack opening. The holds were conducted in displacement control, and a minimal amount of stress relaxation (1% – 2 % of max stress) occurred during the hold. In all images presented here, the loading axis is vertical on the page.

2.3 Experimental Results

The undeformed microstructure of the cast AM60B Mg is shown in Figure 2.1. For this image the material has been deeply etched to highlight different material phases and the dendritic structure. The slightly blurry appearance of the surface is an artifact of the deep etching and the enhanced contribution of backscattered electrons to the overall signal used to better reveal the microstructure. As highlighted in Figure 2.1, and confirmed by local EDX measurements, three different phases are present in the AM60B microstructure. In Figure 2.1a, two AlMnSi particles are indicated. The AlMnSi particles are dispersed throughout the microstructure and they appear brightest on the SEM micrographs due to their elevated position on the surface. A higher magnification image in Figure 1b, shows the next brightest phase, β-$Al_{12}Mg_{17}$, which occurs in the form of particles decorating the interdendritic regions. The darkest phase is the HCP α-Mg dendrite cells, which contain only trace amounts of Al, and are preferentially polished and etched (Figure 2.1b). The interdendritic regions are revealed by the brightness contrast between the β and α phases. In these regions, the Al content was found to be greater than in the α phase but less than in the β phase. The average dendrite cell size (DCS) in the material is approximately 10 microns.

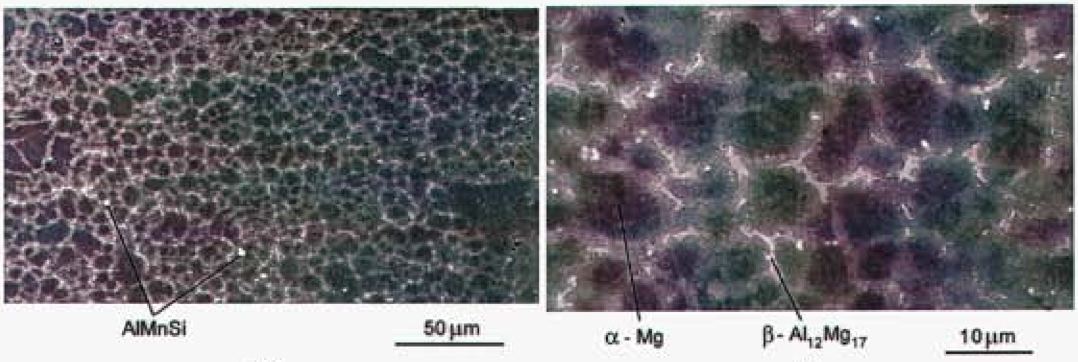

Figure 2.1. SEM image of the undeformed microstructure in AM60 Mg at (a) low and (b) high magnification. Phases are identified in the main text.

Figure 2.2 shows the fracture surfaces of samples cycled (a) in vacuum and (b) in water vapor.

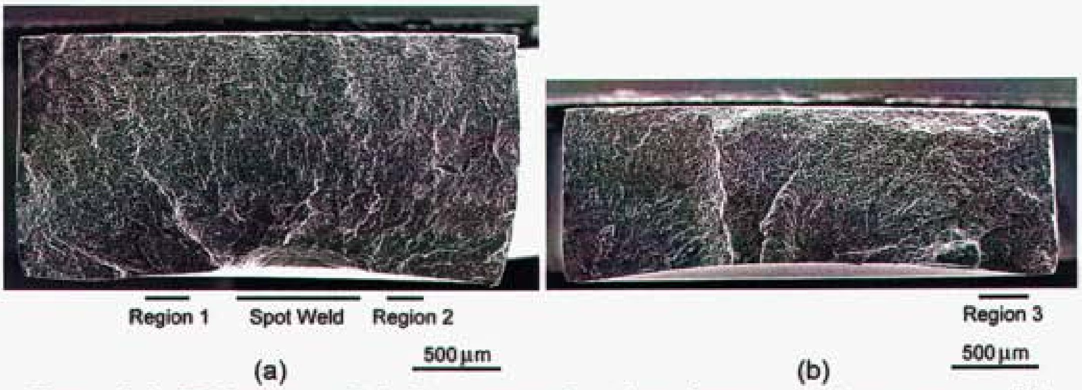

Figure 2.2. SEM images of the fracture surface from the tests in (a) vacuum and (b) water vapor. Several positions that were inspected in-situ during fatigue are indicated below the respective images.

The dimple and the spot weld are visible on the sample cycled in vacuum (Figure 2.2a), while only the dimple is present in the sample cycled in water vapor (Figure 2.2b). The dimple is observed as the gradual rounding of the specimen on the bottom of the fracture surface in Figures 2.2a and 2.2b. *In-situ* observations were made a several locations on the surface of the samples during cycling. As indicated in Figure 2.2, several of the observed locations contained cracks that ultimately linked with the final fracture path. In the sample that was cycled in a vacuum, two regions of observation are distinguished, Region 1 and Region 2. In the sample that was cycled in water vapor, a region of observation is labeled as Region 3. Several observations will be presented from other regions of the sample that did not ultimately link with the final crack that created the fracture surface. The lives of the samples cycled in vacuum and water vapor environments were 35,541 and 14,970 cycles, respectively. These numbers are not meant for direct quantitative comparison since the stress concentration in the sample cycled in vacuum was more severe that the stress concentration in the sample cycled in water vapor. However, the longer life of the sample cycle in vacuum, despite the larger stress concentration, does show that the environment has a considerable influence on the fatigue life.

Figures 2.3-2.5 present observations of the formation of fatigue cracks away from the spot weld during cycling of the sample at 90 MPa in the vacuum environment.

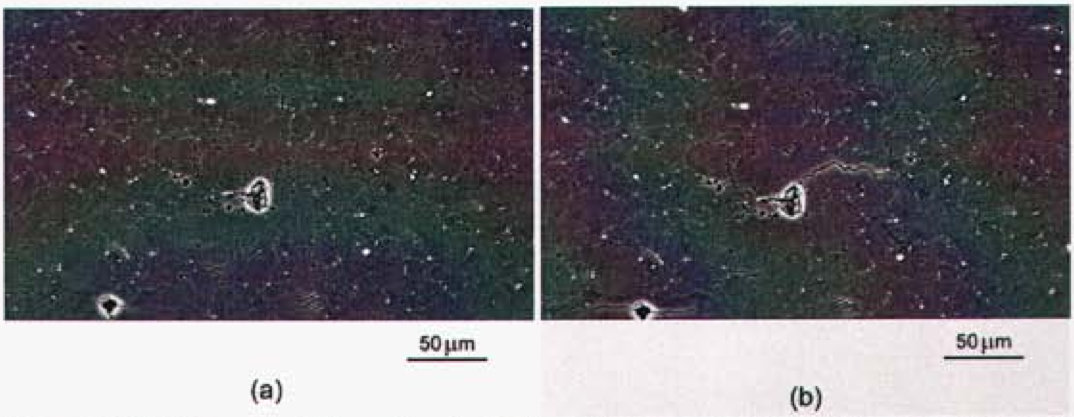

Figure 2.3. Fatigue crack formation in Region 1 in the sample tested in a vacuum at (a) 3,200 and (b) 7,300 cycles.

After 3,200 cycles at 90 MPa (plus the pre-cycling at 135 MPa), the first cracks appeared near larger pores. In Figures 2.3a and 2.3b we observe the formation of three different cracks in the vacuum environment between cycles (a) 3,200 and (b) 7,300 in a region with a rather high volume fraction of microporosity (small black spots) surrounding a large pore (Region 1). In the lower left of Figure 2.3a, a small crack has initiated on the right side of the pore by cycle 3,200. The pore in the center also has a small crack on its left side by 3,200 cycles. Also note that the large a-Mg dendrite cell in the upper right has a few persistent slip bands, but no cracks at 3,200 cycles (Figure 2.3a). At 7,300 cycles (Figure 2.3b), a rather large crack has formed on the right of the center pore, and the pore on the lower left also has cracks emanating from both sides. The intersection point between the persistent slip band in the large dendrite on the upper right and some local porosity has also formed a small crack sometime before 7,300 cycles. *None of these features existed after the pre-cycling history of 130 cycles at 135 MPa.*

In Figure 2.4 we examine another crack formation event under vacuum in a porous region (Region 2) with a smaller volume fraction of porosity at the surface. At 3,200 cycles (Figure 2.4a) the crack is not seen at the scale of observation, but numerous persistent slip bands are evident in adjacent dendrite cells. Approximately 800 cycles later (Figure 2.4b), a small crack has formed in the interdendritic region by linking small pores at the surface. After 7,300 cycles (Figure 2.4c) the crack has grown to an appreciable size.

Clearly, the driving force for the formation of the crack in Figure 2.4 is the strong slip incompatibility between adjacent grains as marked by the presence and absence of persistent slip bands. Under vacuum, cracks were also observed to form in the base Mg material rather than at a pore or within the interdendritic region. In Figure 2.5 we track the development of a fatigue crack at persistent slip bands within a rather large dendrite cell. The persistent slip bands coarsen as a function of cycling until a crack is distinctly formed between 11,000 (Figure 2.5c) and 15,700 cycles (Figure 2.5d). The precise cycle at which the crack formed is vague, but it is certain that the crack in Figure 2.5c took longer to initiate (between 11,000 and 15,700 cycles) compared to the cracks at the pores in Figures 2.3 and 2.4 (between 3,200 and 7,300 cycles).

Figure 2.4. Fatigue crack formation in Region 2 in the sample tested in a vacuum with porosity at (a) 3,200, (b) 4,000, and (c) 7,300 cycles.

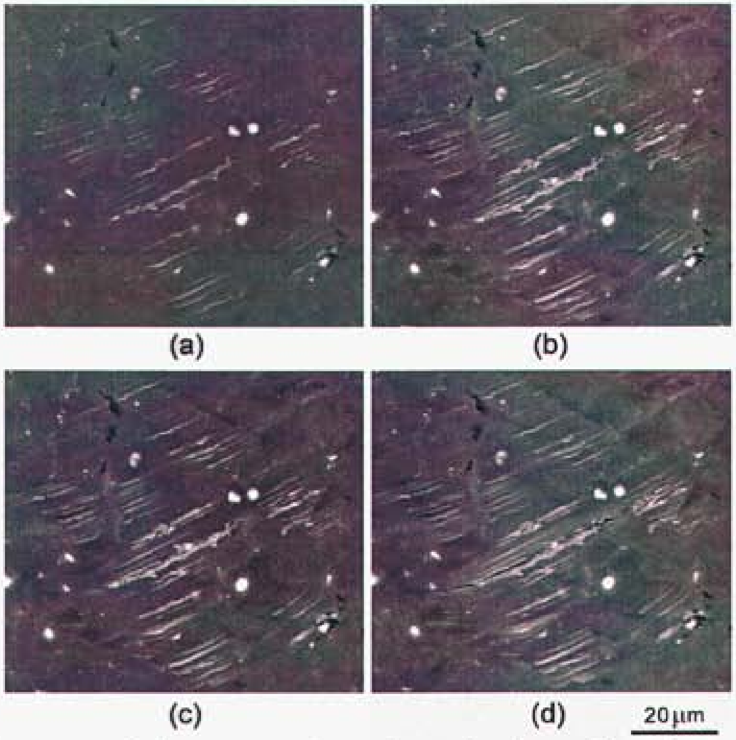

Figure 2.5. Fatigue crack formation within a large dendrite cell in the sample tested in a vacuum at persistent slip bands at (a) 3,200, (b) 7,300, (c) 11,000, and (d) 15,700 cycles.

Figures 2.6-2.8 present observations of the propagation of small fatigue cracks during cycling at 90 MPa in the vacuum environment. Figure 2.6 shows a series of images tracking the progression of the crack formed at the center pore in Figure 2.3 (Region 1). In only 11,000 cycles, the crack has progressed through the region of high microporosity (Figure 2.6b). Following initial propagation through the porosity-laden interdendritic network, by a distance of about 6-10 times the average dendrite cell size, the crack grows straight in a direction roughly perpendicular to the loading axis on both sides (Figures 2.6c-2.6e). The crack on the left of the pore ultimately takes a significant turn only to merge with a region containing a microcrack.

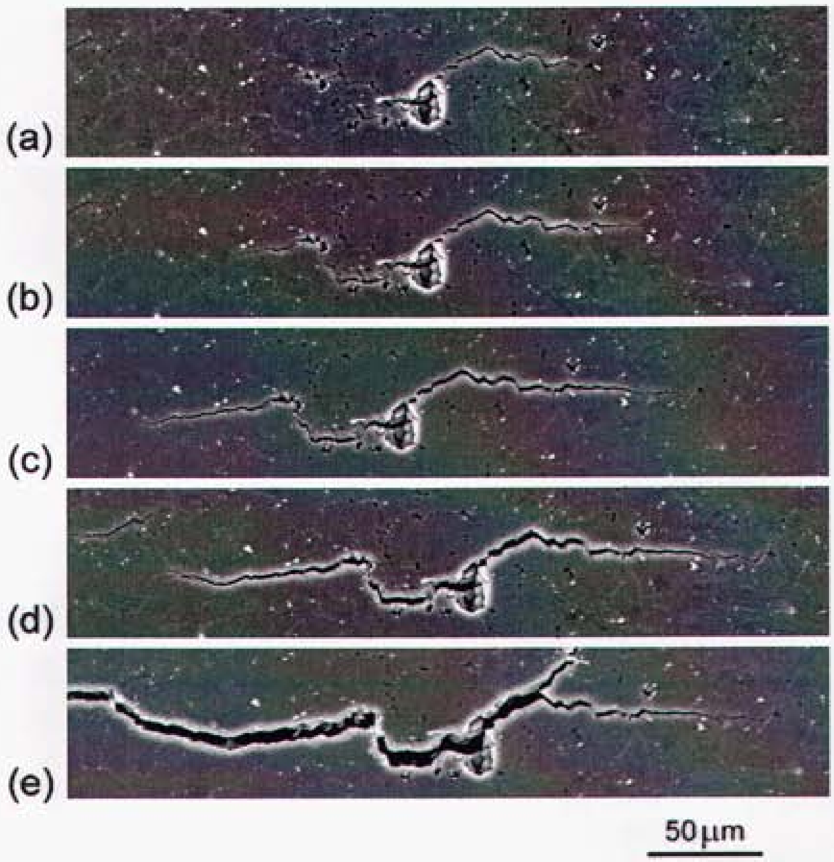

Figure 2.6. Propagation of a small fatigue crack from a pore in Region 1 in the sample tested in vacuum at (a) 7,300, (b) 11,000, (c) 19,300, (d) 22,600, (e) and 34,813 cycles.

A slightly different growth pattern is observed for the small crack formed in Region 2, as shown in Figure 2.7. The crack in Figure 2.7b is considerably smaller than the crack in Figure 2.6b at equivalent cycle numbers. Although the crack in Figure 2.7 does not have an extensive micro-porosity network to travel through during the initial stages of growth, the crack still meanders significantly through the microstructure. The meandering is linked to propagation along persistent slip bands in dendrite cells and in interdendritic regions. In fact, multiple observations of small and large fatigue cracks following persistent slip bands ahead of the crack tip were made in the vacuum environment. Figure 2.7 also indicates that propagation occurs in part along interdendritic regions between misoriented cells (PSBs in different directions or PSBs occurring in one cell and not its neighbors), again likely due to incompatibility of slip for the low symmetry HCP lattice.

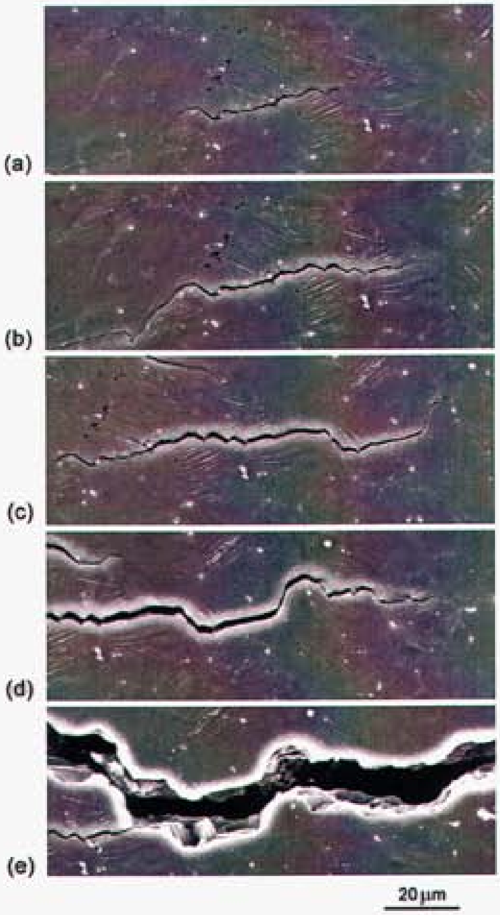

Figure 2.7. Propagation of a small fatigue crack through the microstructure in Region 2 in the sample tested in vacuum at (a) 7,300, (b) 11,000, (c) 19,300, (d) 22,600 cycles, and (e) 34,813 cycles.

Figure 2.8 presents images from the specimen tested in vacuum, i.e. the left half of the crack seen in Figure 2.6 from Region 1. The image in Figure 2.8a was created using secondary electrons, while high-contrast backscatter electron imaging created the image in Figure 2.8b. The purpose of Figure 2.8b is to generally show the location of microstructural features relative to the crack path, while Figure 2.8a shows a duplicate high-resolution image of the crack. Although the crack initially follows the interdendritic region with microporosity, it eventually propagates through the dendrite cells when it has a *half-length* roughly 3-5 times the average dendrite cell size. Small kinks in the crack growth direction seen in Figure 2.8a are linked to the impingement of the crack on interdendritic boundaries, the bright areas in Figure 2.8b. However, crystallographically favored crack paths cause larger changes in the growth direction of the cracks (Figure 2.7). Figure 2.9 presents a final set of images from Region 1 showing (a) the fracture surface top-view and (b) an in-situ view after final fracture. Aside from the major pore and surrounding micropores that promoted crack formation, minimal porosity was detected on the fracture surface in Region 1. Similarly, minimal porosity was discovered on the fracture surface in Region 2. Consequently, we can eliminate the possibility that a large pore hidden underneath the surface formed the crack that was examined *in-situ* at the surface.

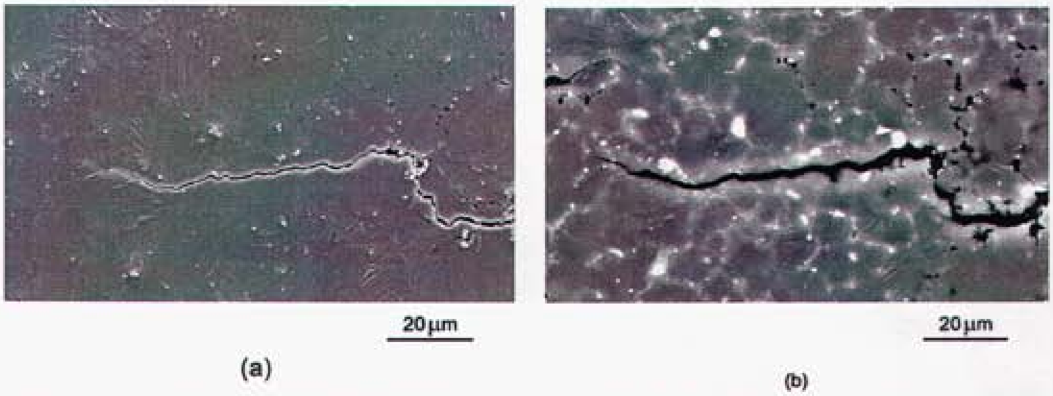

Figure 2.8. Higher magnification view of the left half of the crack in Figure 6d in Region 1 in the sample tested in vacuum. The crack was imaged using (a) secondary and (b) backscatter electrons.

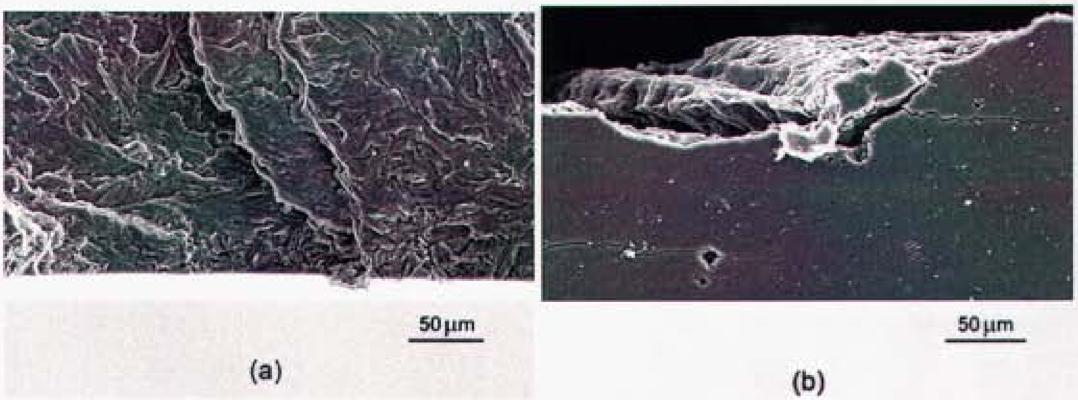

Figure 2.9. Post-mortem view of the crack in Region 1 in the sample tested in vacuum from the (a) fracture surface and (b) in-situ viewing plane.

In-situ SEM mages from the sample fatigued in the water vapor environment are shown in Figures 2.10 through 2.13. Figure 2.10a shows a small crack that formed within a dendrite cell in the cast Mg after 100 cycles at 135 MPa. Similar cracks were *not found* in the sample cycled in vacuum after 130 cycles at 135 MPa. Figure 2.10b shows the same crack after 11,000 cycles at 90 MPa, with a slightly shifted field of view. The small crack follows a predominant Mode I growth pattern through the dendrite cells, changing direction only when encountering an AlMnSi particle (Fig. 2.10b). Figure 2.11 shows a small crack formed by the linking of microporosity at (a) 353 cycles and (b) 11,000 cycles at 90 MPa in Region 3 (Figure 2.2b).

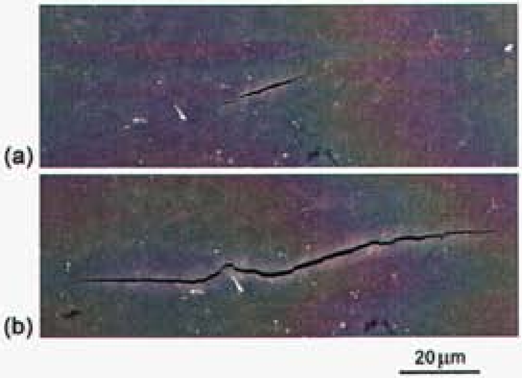

Figure 2.10. Cracks in the specimen cycled in water vapor after (a) precycling and (b) 11,000 cycles.

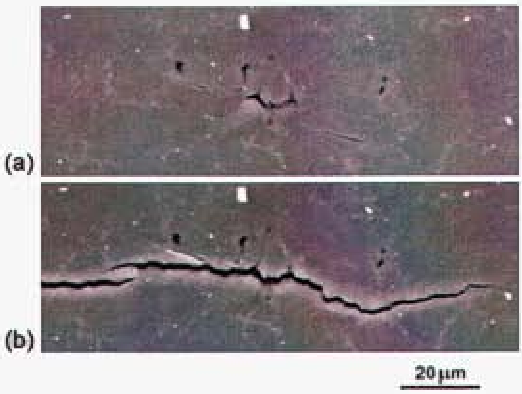

Figure 2.11. Cracks in the specimen in cycled water vapor in Region 3 after (a) 353 cycles and (b) 11,000 cycles.

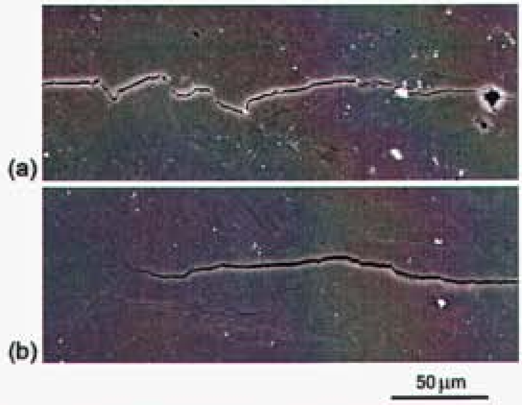

Figure 2.12. Comparison of crack profiles in a cast magnesium alloy under the following conditions (a) vacuum at 34,000 cycles and (b) water vapor at 11,000 cycles.

The crack is initially formed in a region of microporosity, and it grows both through the dendrite cells and in the interdendritic regions. The crack does not closely follow the micropores in adjacent dendrite cells. Figure 2.12 compares a typical crack in the cast magnesium alloy cycled in (a) vacuum and (b) water vapor environments, at 34,000 and

11,000 cycles, respectively. The crack in Figure 2.12a is about 300 mm long, while the crack in Figure 2.12b has a total length of about 250 mm. Despite similar microstructures, the fatigue crack in the magnesium cycled in vacuum interacts more strongly with the microstructure, as evidenced by its prolonged meandering, compared to the crack in the magnesium cycled in water vapor. Figure 2.13 is an image of the fracture surface from Region 3 (Figure 2.2b and Figure 2.11). The fracture surface shows negligible porosity away from the initiation site and highlights different regions of crack growth behavior (note the semicircular crack path).

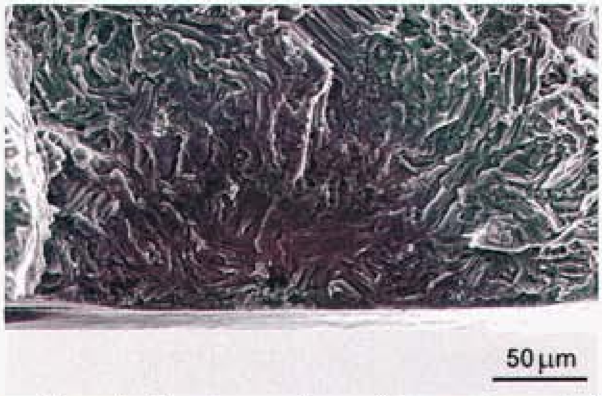

Figure 2.13. Image from the fracture surface of the specimen in Region 3 from the sample tested in water vapor.

Figure 2.14 presents crack size as a function of cycle number for various cracks in water vapor and vacuum.

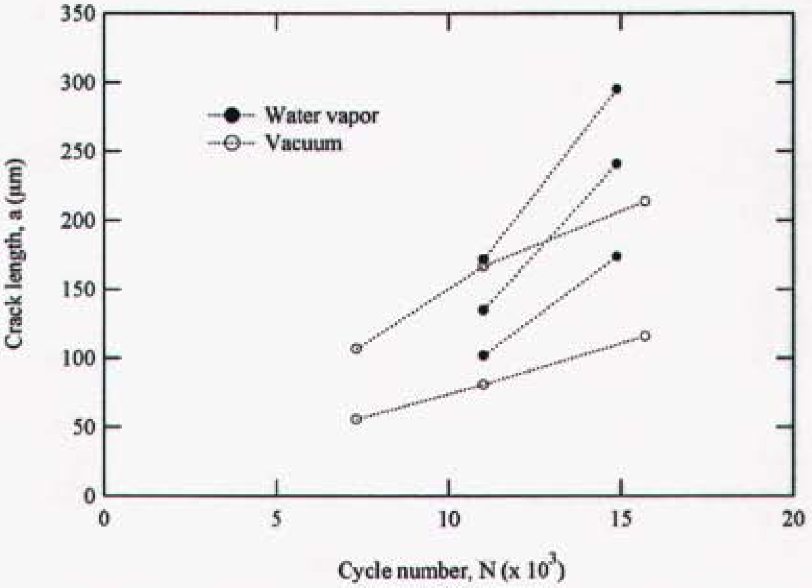

Figure 2.14. Snapshot of crack size as a function of cycle number for several cracks growing in vacuum versus water vapor.

The purpose of Figure 2.14 is to demonstrate the difference in "average" crack growth rate of cracks growing in water vapor versus vacuum. For all cracks observed, on average, the cracks grow faster in the water vapor versus vacuum. The details of this observation will depend on the applied loading conditions, absolute crack size, and local microstructural conditions. In the present work, we have not tracked the cracks at frequent cycle intervals as needed to report more detailed crack growth rate data. However, the data in Figure 2.14 is sufficient to demonstrate that the average crack growth rate of cracks in water vapor is higher than those in water vapor for the crack sizes examined.

2.4 Discussion

The purpose of this paper is to provide a qualitative assessment of the fatigue mechanisms in cast AM60 Mg using *in-situ* environmental SEM microscopy. Particular emphasis is placed on examining the early stages of fatigue, including crack formation and microstructurally small crack propagation. In this discussion we will first assess the observed mechanisms in the context of relevant literature, then will consider the impact of the observations on micro-mechanical modeling of fatigue mechanisms. Before discussing the results we note that caution should be exercised when interpreting surface observations in terms of fatigue mechanisms. It is always possible that the observed damage may only be present at the surface. In all cases we have attempted to find cracks with relatively large opening displacements at maximum load, such that they likely extend reasonably into the bulk microstructure. Nearly all of the results presented here represent significant cracks that contributed to the final fracture path. For example, the crack monitored in Region 3 showed a relatively fast surface growth rate (Figure 2.11), but also showed proportional penetration into the bulk material via post-mortem fractography (Figure 2.13).

In the present study we have observed *in-situ* the formation of fatigue cracks at casting pores in a vacuum environment (Figures 2.3 and 2.4) and a water vapor environment (Figure 2.11). In the vacuum environment, some cracks formed after very few cycles at 10-20 micron pores without appreciable accumulation of cyclic plasticity, via persistent slip band formation, in the surrounding dendrite cells (Figure 2.3). However, we also observed crack formation under vacuum in a region with smaller micropores (2-4 microns) that was preceded by an observable accumulation of cyclic plasticity in the surrounding dendrite cells (Figure 2.4). The existence of *local* plastic strain accumulation via persistent slip bands in the relatively small dendrite cells in Figure 2.4 was uncommon. However, the cyclic plasticity was clearly linked to the presence of porosity coupled with the favorable shearing orientation of primary slip systems in the dendrite cells with respect to the loading axis (approx. 45° angle to the applied loading direction). It is important to note the significant slip incompatibility observed in adjacent dendrite cells near the crack initiation site in Figure 2.4. The presence of slip in some cells and the absence of slip in others, leads to strong plastic strain mismatches and high stresses in the interdendritic regions. All of these factors contributed to the formation of a fatigue crack in this interdendritic region. A previous study [24] has also observed slip features near sites of crack formation in extruded Mg via a post-mortem fracture analysis. In the water vapor environment, cracks started near pores without observable persistent slip band formation (Figure 2.11).

Fatigue cracks were also found to form within large, relatively soft a-Mg dendrite cells in vacuum (Figures 2.5) and water vapor (Figure 2.10) environments. In the vacuum environment, the crack formation was evident at persistent slip bands within relatively large dendrites that are favorably oriented with respect to the loading axis. The large dendrite cell in Figure 2.5 is nearly 60 mm in diameter, compared to an average cell size of 10 mm near the nucleation site in Figure 2.4. Persistent slip band formation and subsequent local surface roughening, as a function of cycles, was frequently observed in large dendrite cells. The extrusions and intrusions at the surface eventually lead to fatigue crack formation as typical for wrought materials. It is interesting that once formed, the crack rapidly reaches the size of the dendrite cell by spanning the weakened shear zone (Figure 2.5). In the vacuum environment, the crack formation life for this mechanism is significantly longer than the formation life near pores. However, if the maximum pore size in a highly stressed region is reduced below a critical level, this traditional persistent slip band mechanism may dominate if large dendrite cells are present.

In contrast to observations in the vacuum environment, crack formation in the water vapor environment was relatively rapid in selected regions without noticeable influence of surrounding porosity. Figure 2.10 shows an example of a fatigue crack that formed in the water vapor environment during precycling. Several similar cracks rapidly formed in the Mg cycled in water vapor that were not connected with porosity or observable persistent slip bands. Apparently, the water vapor accelerates the fatigue crack formation process in the Mg in specific locations. This acceleration of fatigue crack formation does not occur at all microstructural features in the sample, as evident from the smaller total number of cracks growing in the sample cycled in the water vapor environment. However, in selected locations, cracks formed faster in the water vapor environment. We note that relatively large pores, which usually exist in the interior of a larger component, might still facilitate early crack formation compared to traditional surface mechanisms. However, such pores did not exist in this die-casting, and in addition these pores will not be subject to the environmental effects noted here.

Based on crack tip stresses, cracks should preferentially grow in a Mode I direction. However, particularly for microstructurally small cracks, variations in the microstructure can alter the direction of crack growth in an effort to avoid an obstacle or link with a weakened material zone. In the water vapor environment, microstructurally small surface fatigue cracks in the cast magnesium alloy preferentially propagated straight through the dendrite cells. Some crack meandering through the microstructure was discovered when the cracks would propagate through interdendritic regions. However, the meandering of the cracks growing in the water vapor environment was minimal compared to the meandering of the cracks in the vacuum environment. In the presence of the harsh environment, nominally Mode I growth through the dendrite cells was accelerated. The cracks formed in the water vapor environment were only noticeably deterred from straight Mode I growth patterns by interdendritic regions (Figure 2.11) or second phase particles (Figure 2.10). In addition, small fatigue cracks did show some meandering to link with other micro cracks in the near vicinity (Figure 2.11). Meandering is evident from the linkage of the main crack (Figure 2.11b) and a small crack to the lower right of the formation site (Figure 2.11a).

In the vacuum environment, microstructurally small fatigue cracks grew through the dendrite cells, persistent slip bands, and interdendritic regions. Fatigue cracks growing in the vacuum generally grew much more slowly, i.e., more cyclic damage was required to accumulate ahead of the crack tip (Figure 2.14). Previous studies have shown that long fatigue cracks grow more slowly in lower humidity environments [13, 14]. The small fatigue cracks in the vacuum environment were found to propagate preferentially through persistent slip bands formed ahead of the crack tip as has been previously observed in cast Mg [18] and other alloys [25]. Fatigue cracks prefer to propagate along the persistent slip bands because these regions have been weakened by intense dislocation activity and cracking. Fatigue cracks prefer to grow along interdendritic regions when micropores are present to help create a weak crack path (Figure 2.6). In addition, small cracks can propagate in or near the interdendritic regions when slip incompatibility between cells generates high stresses in the interdendritic regions (Figure 2.7).

In previous work we have observed that a fatal internal crack, as observed post-mortem on the fracture surface, prefers to propagate through the Mg dendrite cells at small sizes [17]. Based on the present observations in vacuum and water vapor, we see that this tendency is amplified in the presence of environmental effects. The rationale is that small cracks have a relatively more difficult time propagating through interdendritic regions which contain b particles within a Mg matrix with high levels of Al in solid solution that is relatively stronger then the interior of the dendrite cells. The small fatigue cracks, with very small crack tip plastic zones, prefer to propagate through the relatively soft a-Mg cells. However, the presence of microporosity in the interdendritic regions amplifies the crack tip driving force and cracks in vacuum have been observed to move along interdendritic regions, propagating through these micropores. In addition, the crack tip driving force may be significantly amplified near the interdendritic regions by slip incompatibility between the a-Mg cells. This amplification can cause small cracks to propagate in or near the interdendritic regions where incompatibility of slip is highest.

Micro-mechanical modeling of these phenomena using the finite element method will provide more quantitative information for larger scale modeling efforts and casting design guidelines. Any model that hopes to capture the relevant physics of the problem should account for the low symmetry slip anisotropy in HCP Mg and the effects of the periodic interdendritic regions. Fatigue crack formation and small crack propagation, without environmental influence, is highly dependent on preferential basal slip in a-Mg. This preferential slip can lead to slip incompatibilities between cells and persistent slip bands within cells, both of which are critical for crack formation and small crack propagation. The influence of the environment on the formation and growth of surface cracks also appears to be of significant importance. Based on the present results, introduction of a water vapor environment reduces the resistance to fatigue crack formation and growth in cast Mg. Because of this, rapidly propagating cracks do not meander onto crystallographic planes as often as cracks that are slowly propagating without environmental influence. The presence of the environment weakens the dendrite cell material's inherent resistance to fatigue crack propagation. One possible rationale for this would be hydrogen embrittlement due to the reaction of water vapor with freshly exposed material at the crack tip. However, at present this mechanism is speculative and needs more study. Modeling of this environmental effect may involve a relative weakening of the fatigue resistance of the dendrite cell as a function of environment.

The effect of different local cyclic plasticity levels in the Mg grains near pores needs quantification. Cyclic plastic strain levels necessary to form a fatigue crack may depend on the orientation of the grains near the pores, and the relative size of the dendrite cells and pores. Both large dendrite cells and large pores elevate *local* cyclic plasticity levels. Similarly, the effect of the interdendritic regions on crack propagation needs further quantification with modeling. In the presence of porosity or slip incompatibility, the cracks seem to select the interdendritic regions for growth. However, in some situations, the cracks avoid these regions and grow through the dendrite cells. Clearly, accurate micromechanical models are needed to examine the effect of the Al-rich and b particle-laden interdendritic architecture on small crack growth driving forces. However, more experimental work is required to shed light on the relative strength of these regions as barriers to small crack growth. This could come from quantitative small crack growth studies supplemented by large crack studies on Mg materials with different Al contents, and perhaps nanoindentation.

2.5 Conclusions

1. The presence of a water vapor environment significantly alters the nucleation and small crack propagation characteristics and rates in cast AM60 Mg compared to a vacuum environment.

2. In a vacuum environment, surface fatigue cracks formed rapidly at larger pores, sometimes preceded by observable cyclic slip accumulation. At higher cycle numbers in the vacuum environment, additional cracks were discovered to form at persistent slip bands within relatively large dendrite cells.

3. In a vacuum environment, microstructurally small fatigue cracks were found to follow interdendritic regions in the presence of a high level of microporosity and crystallographic planes in the presence of persistent slip bands ahead of the crack tip. In the absence of these weak microstructural paths, small cracks propagated straight through the dendrite cells and in, or near, interdendritic regions, depending on the local cell arrangement.

4. In a water vapor environment, isolated surface cracks formed rapidly within the Mg cells and at pores. Small cracks in the magnesium cycled in water vapor grew significantly faster than in the vacuum. Small fatigue cracks in the magnesium cycled

in water vapor often propagated straight through the dendrite cells in a Mode I manner. The cracks in the water vapor environment sometimes propagated in, or near, interdendritic regions, but less often compared to cracks growing in the vacuum environment.

5. Small fatigue cracks in the magnesium avoided second phase particles in both vacuum and water vapor environments. The interdendritic regions also caused perturbations in fatigue crack paths in both water vapor and vacuum environments.

6. The effect of porosity on the fatigue mechanisms in cast Mg depends on the relative size and distribution of the pores. Distributed microporosity (1-2 microns) caused a preferential path for small fatigue cracks. Slightly large micropores (10-20 microns) served as crack formation sites.

7. The growth pattern of small cracks (a < 6-10DCS, where DCS is the average dendrite cell size) was more sensitive to microstructural features in the cast Mg compared to the predominantly Mode I growth pattern of cracks longer than about 6-10 DCS.

2.6 Acknowledgements

The authors thank Anja Puda for her careful surface preparation of the cast Mg alloy specimens for *in-situ* studies. This work was performed with the support of Dick Osborne and Don Penrod for the USCAR Lightweight Metals Group.

2.7 References

[1] Jambor A, Beyer M. Mat. Des. 1997; 18:203-209.

[2] Froes FH, Eliezer D, Aghion EL. JOM 1998; 50:30-34.

[3] Makar Gl, Kruger J. Int. Mat. Rev. 1993; 38:138-153.

[4] Alves H, Koster U, Aghion E, Eliezer D. Mat. Tech. 2001; 16:110-126.

[5] Lunder O, Aune TK, Nisancioglu K. Nat. Ass. Corr. Eng. 1987; 43:291-295.

[6] Song G, Atrens A, Dargusch M. Cor. Sci. 1999; 41:249-273.

[7] Ambat R, Aung NN, Zhou W. Cor. Sci. 2000; 42:1433-1455.

[8] Ghali E. Mag. Alloys 2000. Mat Sci. For. 2000; 350:261-272.

[9] Gray JE, Luan B. J. Alloy Comp. 2002; 336:88-113.

[10] Perov SN, Ogarevic VV, Stephens RI. J. Eng. Mat. Tech. 1993; 115:385-390.

[11] Goodenberger DL, Stephens RI. J. Eng. Mat. Tech. 1993; 115:391-397.

[12] Stephens RI, Schrader CD, Lease KB. J. Eng. Mat. Tech. 1995; 117:293-298.

[13] Shibusawa T, Kobayashi Y, Ishikawa K. J. Jap. Inst. Met. 1997; 61:298-302.

[14] Fuchs U, Lipowsky H, Mayer H, Papakyriacou M, Stich A, Tschegg S, Zettl B. Mat. Wiss. Werk. 2002; 33:15-23.

[15] Mayer HR, Lipowsky H, Papakyriacou M, Rosch R, Stich A, Stanzl-Tschegg S. Fat. Frac. Eng. Mat. Struc. 1999; 22:591-599.

[16] Fuchs U, Lipowsky H, Mayer H, Papakyriacou M, Stich A, Tschegg S, Zettl B. Mat. Wiss. Werk. 2002; 33:117-127

[17] Horstemeyer MF, Yang N, Gall K, McDowell DL, Fan J, Gullet P. Fat. Frac. Eng. Mat. Struc. 2002; 25:1-12.

[18] Eisenmeier G, Holzwarth B, Höppel HW, Mughrabi H. Mat. Sci. Eng. A 2001; 319:578-582.

[19] Stephens RI, Grabowski L, Hoeppner DW. Int. J. Fat. 1993; 15:273-282.

[20] Halliday MD, Poole P, Bowen P. Fat. Frac. Eng. Mat. Struc. 1995; 18:717-729.

[21] Halliday MD, Zhang JZ, Poole P, Bowen P. Int. J. Fat. 1997; 19:273-282.

[22] Zhang XP, Wang CH, Chen W, Ye L, Mai YW. Scr. Mat. 2001; 44:2443-2448.

[23] Li WF, Zhang XP. Mat. Sci. Eng. A 2001; 318:129-136.

[24] Shih TS, Liu WS, Chen YJ. Mat. Sci. Eng. A 2002 325:152-162.

[25] Halliday MD, Poole P, Bowen P. Mat. Sci. Tech. 1999; 15:382-390.

3 Creep of Thin Film Au on Bimaterial Au/Si Microcantilevers

We examine creep of thin film Au on curved bimaterial Au/Si microcantilevers. Time-dependent inelastic strains in the Au film lead to gradual changes in the microcantilever curvature over time. Curvature-temperature-time experiments are used to examine the effects of hold temperature and maximum annealing temperature on the inelastic response of the Au films. Experiments reveal inelastic strains in the Au films due to creep, recovery, and microstructural coarsening. At moderate hold temperatures, 30 °C < T < 175 °C, inelasticity in the Au films is observed to be a competition between creep and recovery. Creep strains are driven by tensile stresses in the film and serve to decrease the microcantilever curvature towards the equilibrium curvature of the underlying Si beam. Strains due to recovery of the metastable Au cause contraction of the film and the development of intrinsic tensile film stresses. At higher hold temperatures T > 175 °C, the response of the film is dominated by microstructural coarsening which leads to an expansion of the film, the development of intrinsic compressive film stresses, and hillock formation. The recovery and microstructural coarsening both lead to 'anomalous' changes in microcantilever curvature since the curvature gradually increases or decreases away from the equilibrium curvature of the underlying Si. The inelastic behavior of the Au film is shown to depend on annealing temperature through changes in initial film stress after thermo-elastic cooling and degree of recovery.

3.1 Introduction

Bimaterial microcantilever beams are a critical component in numerous Micro Electro Mechanical Systems (MEMS). Emerging MEMS applications utilizing bimaterial metal/ceramic microcantilevers include infrared light detection [1-3], biohazard detection [4], chemical sensing [5, 6], microelectronic switching [7, 8], photo-thermal sensing/actuation [9, 10], optics [11-13], micromanipulation [14], and microcooling devices [15]. The aforementioned MEMS utilize the bending displacement of a bimaterial microcantilever (Figure 1) to facilitate transduction for sensing or actuation. The means to induce bending in bimaterial microcantilevers depends on the particular MEMS application [1-15]. Although numerous innovative applications depend on bimaterial microcantilevers [1-15], the reliability of these transducers has not been examined in detail.

A two-dimensional schematic of a dual bimaterial cantilever beam is presented in Figure 3.1. The beam length is given as L, while the radius of curvature of the beam is denoted as R. The curvature in the beam, κ, is calculated as the inverse of the radius for a perfect circle. The maximum gap height above the substrate, at the tip of the cantilever, is the summation of the post height and the tip displacement, δ. A contraction of the Au, either due to a differential thermal expansion between Au and Si or a time-dependent inelastic strain in the Au, leads to an increase in curvature of the bimaterial beam (Figure 3.1). On the other hand, an expansion of the Au leads to a decrease in the curvature of the bimaterial beam. Regardless of the MEMS application, it is critical for bimaterial microcantilevers to exhibit consistent and predictable displacements over time. Superfluous displacements of the cantilever alter the gap height between the cantilever and the substrate (Figure 3.1) and can significantly change voltages required for actuation or capacitive sensing values.

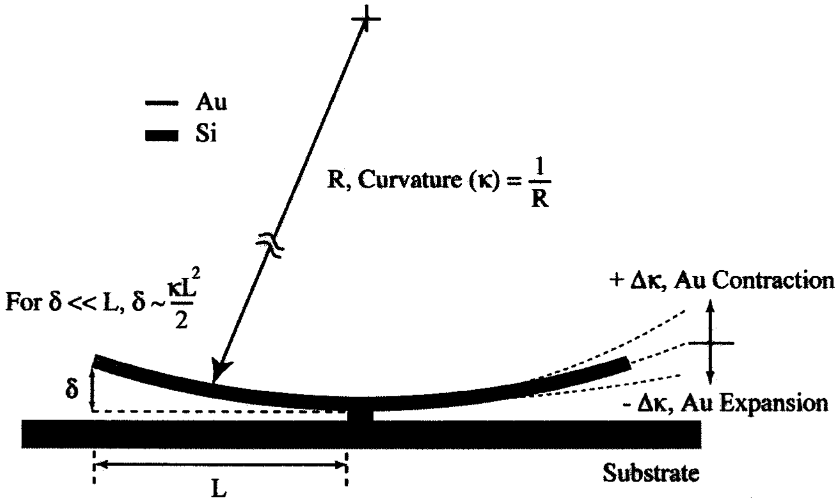

Figure 3.1. Schematic of a bilayer microcantilever beam used for sensing and actuation indicating the implications of dimensional changes in the Au layer.

Bimaterial cantilevers containing a metallic layer may be vulnerable to creep and/or stress relaxation. Several researchers have observed creep and stress relaxation in metallic materials for MEMS including freestanding thin films and bimaterial microcantilevers [16-27]. In bimaterial microcantilevers, moderate creep strain in the metallic layer can lead to a significant change in the position of the transducer over time (Figure 3.1). One recent study discovered that at low stress values, the creep rate of 3.0 μm freestanding thin film copper was three orders of magnitude larger than bulk copper at the same temperature and applied stress [16]. Such extreme creep rates pose a serious reliability concern to bimaterial microcantilevers since they operate at relatively low stresses and their displacements are very sensitive to small inelastic strains in the metallic layer. Although several studies have noted the importance of creep and stress relaxation in metallic MEMS materials, the thermo-mechanics of creep in bimaterial microcantilevers is not fully characterized or understood. As will be further discussed in this introduction, and shown in this paper, fundamental knowledge acquired from previous studies on the thermo-mechanical behavior of thin films does not completely transfer to thin metallic films in microcantilevers.

The deformation of thin films on relatively thick substrates has been extensively studied, motivated by microelectronics applications. The evolution of curvature and stress in thin metallic films on thick Si substrates can occur during film deposition or subsequent thermal holding/cycling [28]. Stresses generated during film growth are typically referred to as "intrinsic stresses" [28]. During film growth, intrinsic tensile stresses are created by the coalescence of expanding grain islands on the deposition substrate [29-32]. Subsequent to island coalescence, the tensile stresses in the film relax via a diffusion-based mechanism at relatively high deposition temperatures [29, 30]. After deposition, the film/substrate are cooled to room temperature and thermal mismatch between the metallic and ceramic layers results in the generation of tensile stresses in the as-deposited films. The as-deposited films often exist in a metastable state since their grain size, defect structure, and crystal structure may be far from equilibrium. High temperature thermal annealing is often employed to obtain a more stable film structure, which is typically the result of recovery, grain growth, and/or crystallization [28].

Numerous researchers have examined stress-relaxation and creep in thin metallic films on thick substrates [33-41]. Most of the studies of thin film creep and stress-relaxation have focused on understanding the complex shape of the stress-temperature curve for film/substrate systems [34, 36-41]. Fewer studies have tracked the evolution of stress/strain in thin films on substrates as a function of time during a temperature hold [36]. In either case, researchers have laid a rather solid foundation for understanding the mechanisms responsible for creep and stress relaxation in thin metal films on thick ceramic substrates. One approach to understanding the mechanisms responsible for creep and stress relaxation in thin metallic films relies on matching experiments and mechanism-based modeling predictions [25, 26, 34, 36, 39]. Models incorporating both diffusion and dislocation creep mechanisms have been successfully employed. One key factor in determining the dominant creep mechanism, aside from loading factors such as stress and temperature, is the presence of a surface passivation layer [34, 36, 39]. A ceramic passivation layer suppresses surface diffusion and results in a thermo-mechanical response that can be reasonably predicted with a power-law (dislocation) creep model [39]. Predicting the creep response of unpassivated thin films generally requires models that capture both diffusion and dislocation mechanisms [39]. It should be noted that in contrast to self-passivating Al, metals such as Cu, Ag, Pt, Au do not form stable oxide films and must be passivated by an externally applied capping layer [35].

Several recent studies have utilized Transmission Electron Microscopy (TEM) to perform direct observations of the mechanisms controlling creep and stress relaxation in thin films on substrates [41] and free-standing thin films [17]. In free-standing Au thin films, Harris and King [17] concluded that diffusion of atoms along grain boundaries and surfaces controlled material creep in a similar manner as described in [42, 43]. In addition, the complete absence of observed dislocation activity in the small grain Au films, coupled with the relatively high zero-creep stress, led the authors to conclude that dislocation processes were not controlling creep rates. A related study on free-standing fine grained Au concluded that dislocation (power-law) creep was the active mechanism based on a stress exponent of approximately 6 ~ 7 in creep tests [26]. A complimentary study demonstrated that coarse-grained thin Au films did not exhibit creep for equivalent stresses and temperatures [25]. Recent *in-situ* TEM observations in Al films determined that both dislocation and diffusion mechanisms can control the thermo-mechanical response of the thin films [41]. The as-deposited Al films contained high dislocation densities and a relatively small grain size. Initial thermal annealing resulted in both recovery (dislocation annihilation) and grain growth. Diffusional processes were determined to play an increasingly important role as dislocation processes were exhausted during thermal exposure [41]. In summary, prior studies have shown that the active deformation mechanism in metallic thin films primarily depends on stress, temperature, time, grain size, film thickness, material, and passivation.

Thin metallic films deposited and pattered onto microcantilevers often share the same initial material structure as thin films deposited onto thicker substrates. However, in released microcantilevers, the ceramic substrate thickness is comparable to the thickness of the metallic layer. Owing to the comparable layer thicknesses, the distribution and magnitude of stresses in the microcantilever's metallic layer is much different than in thin films on thick substrates [44]. For example, the Si layer in the microcantilevers carries a finite fraction of the stresses resulting in stresses as much as 70 % lower in the metallic layer for an equivalent temperature change [44, 45]. It is also important to recognize that bimaterial microcantilevers in MEMS often cannot be thermally annealed to high temperatures typically employed in microelectronic thin film studies, $T >> 200$ °C. High temperature exposure greatly alters the microcantilever initial position and can render it dysfunctional for sensing and actuation. Since the microcantilevers are typically subjected to a low temperature annealing process ($T < 200$ °C) prior to use, the deposited thin metallic film exists in a metastable state during operation. The lower operating stresses and metastable material structure are two key factors differentiating the study of creep and stress relaxation in bimaterial microcantilevers from traditional studies of thin films on thick substrates. Recent work on free-standing metallic thin films is more applicable to bimaterial microcantilevers since the films have been studied in the as-deposited state at lower temperatures and stresses [16, 25, 26].

Previous studies have examined the nonlinear thermo-elastic behavior [44], thermo-mechanical cyclic response [27, 45], and creep behavior [18, 19] of Au/Si microcantilevers and microplates. Prior creep and stress relaxation studies on Au/Si microstructures have examined creep in plates and beams after an annealing temperature of 190 °C and a hold temperature of 120 °C [18, 19]. The effect of different annealing temperatures or hold temperatures was not considered. A power-law creep model was shown to provide reasonable short-term creep and stress relaxation predictions for bimaterial structures with the same thickness of Si [18]. However, when the thickness of the Si was changed, which alters the stress distribution and magnitude in the Au layer, the power-law model was incapable of predicting the creep response using the same Au material properties. A surface passivation layer, in the form of an Atomic Layer Deposition (ALD) coating, was shown to suppress creep and stress relaxation in the Au/Si microcantilevers [19].

In the present study we examine creep in Au films on Au/Si microcantilevers. In order to better understand the fundamental thermo-mechanics of creep, we focus on the effects of hold temperature and initial annealing temperature on creep behavior. Along with companion microstructural observations, the experiments provide insight into the mechanisms controlling creep and stress relaxation in bimaterial microcantilevers. Although the work only considers Au/Si microcantilevers, the results deliver a general framework for understanding the thermo-mechanics of creep and stress relaxation in other metastable micrometer scale metallic films subjected to relatively low stresses and temperatures. We mention that all results are presented using curvature as the basic parameter. Although film stress is the preferred metric, the film stress and curvature are not uniquely linked via the Stoney equation since the film and substrate thicknesses are comparable.

3.2 Materials and Methods

The gold/polysilicon (Au/Si) beam structures were fabricated using the commercially available Multi-User MEMS Process (MUMPS) [46]. The surface micromachining process consists of a series of lithographic, thin-film deposition, and etching processes standardized in the microelectronics industry. The relevant steps of the complete process consist of first doping an n-type (100) silicon wafer with phosphorous from a $POCl_3$ source. The doped wafer is then coated with a 600 nm Si_3N_4 layer through Low Pressure Chemical Vapor Deposition (LPCVD), a process used for all subsequent depositions with exception to the Au layer. This deposition is followed by the deposition, patterning, and etching of a 500 nm Si layer (Poly 0). Subsequently, a 2 μm thick sacrificial film of phosphosilicate glass (PSG) is deposited. Then, a 2 μm thick polysilicon film (Poly 1) is deposited on the PSG, patterned, and etched. A second 200 nm thick PSG film is then deposited and the wafer is annealed at 1050 °C for one hour to dope the polysilicon with phosphorus from both PSG films, and to reduce the residual stress in the polysilicon film. The 200 nm PSG and 2 μm polysilicon films are lithographically patterned and etched to produce the desired microcantilever beam sizes. Another 0.75 μm thick PSG film is then deposited, followed by a second 1.5 μm thick polysilicon film (Poly 2), and another 200 nm PSG film to serve as a mask for patterning and etching the Poly 2 layer to conform to the desired beam shapes. This is followed by another annealing process to minimize residual stresses and stress gradients in the polysilicon layers. Finally, a 99.999% 0.5 μm gold film is e-beam evaporated over a 20 nm chromium layer and lift-off patterned. The substrate temperature is in the range of 70 °C to 110 °C during the deposition of the Au. Finally, the Au/Si microcantilevers are released from the substrate by etching away the sacrificial PSG films in a 49% hydrofluoric acid solution.

Figure 3.2 is a SEM image of Au/Si bimaterial beams that are each 20 micrometers wide with aspect ratios for cantilevers on each side ranging from 1:4 to 1:14. Support posts connecting the beams to the substrate are visible in the center of each beam, creating free-standing cantilever sections on each side of the posts after the release of the beams from the substrate. The center beams consist of 3.5 μm thick polysilicon layers (Poly 1 + Poly 2) coated with a 0.5 μm gold film. The beams on the left and right consist of 1.5 μm thick polysilicon layers (Poly 2) coated with a 0.5 μm gold film. In the present study, we focus on the center beams, which show more moderate displacements as a function of changes in temperature and time. The beam aspect ratio was found to have a negligible influence on the creep behavior, other than facilitating possible premature contact with the substrate for long beams curved in the negative direction. In this paper, results are presented from relatively longer, higher aspect ratio microcantilevers that did not contact the substrate during negative curvature excursions.

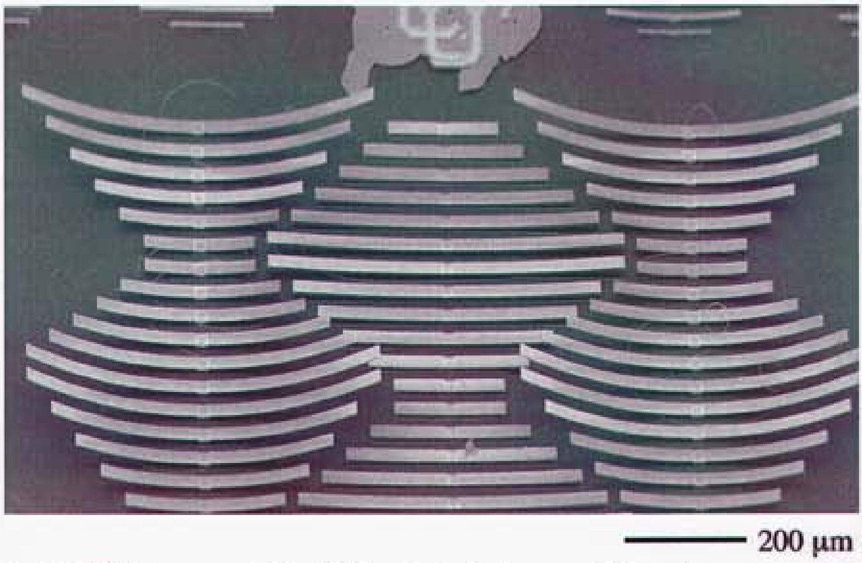

Figure 3.2. FE-SEM images of Au/Si bimaterial microcantilever beams suspended over a Si substrate. The beams in the center have 0.5 μm Au on 3.5 μm Si, while the beams on the left and right have 0.5 μm Au on 1.5 μm Si.

Entire MEMS chips with the bimaterial microcantilevers (Figure 3.2) were placed in a thermal chamber capable of 0.1 °C temperature stability and a temperature range of –160 °C to 600 °C. The chamber has PID feedback controlled heating and cooling rates. Full-field displacement measurements were made *in-situ* as a function of temperature and time with an interferometric microscope. Each measurement takes approximately 2 minutes in order to stabilize the temperature and to obtain two repeat measurements. Measurements were made through a small quartz window in the chamber. The full-field displacements were converted to curvature by fitting a second order polynomial to one-dimensional displacement profiles and then taking the second derivative of the function. The curvature was basically uniform along the beam, justifying a second order polynomial fit. All SEM work was performed using a field emission microscope operated at 10 keV using an in-lens detector for extremely high-resolution imaging (1.6 nm @ 10 keV) before and after thermal holding.

3.3 Experimental Results

Prior to presenting the results of thermal holding studies, we first discuss the initial thermo-mechanical cycle of the Au/Si microcantilevers (Figure 3.3) [44, 45, 52]. After release at room temperature, the beams have an initial curvature denoted by "As Released" in Figure 3.3. During initial heating, the curvature in the beams decreases due to the larger thermal expansion rate in the Au layer relative to the Si layer. The decrease in curvature follows a linear thermo-elastic loading line until a critical temperature is reached. At this critical temperature, the relationship between the curvature and temperature becomes non-linear and the rate of change in curvature as a function of temperature rapidly decreases. The relatively flat curvature-temperature relationship continues until a maximum temperature, T_{max}, is reached and beam cooling is initiated. The cooling response of the beams follows a linear thermo-elastic loading line dictated by the thermal expansion coefficient mismatch between the Au and Si [44, 45].

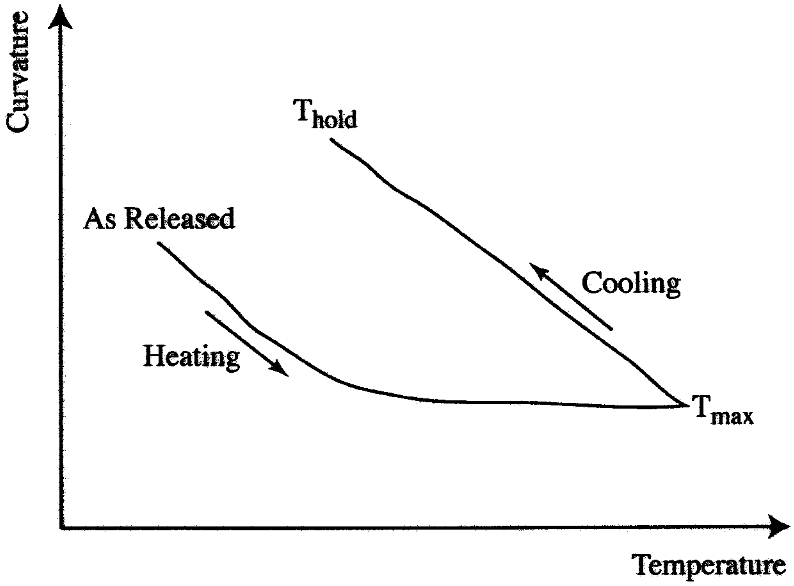

Figure 3.3. Schematic illustrating the initial curvature versus temperature response of a released Au/Si beam.

Cooling is continued until a specified holding temperature, T_{hold}, is reached. The values of T_{max} and T_{hold} will depend on the particular MEMS application. Often, T_{hold} is room temperature, and T_{max} is chosen to tailor the final curvature value at the anticipated operating temperature. In the creep and stress relaxation studies, T_{max} is the "annealing" temperature, while T_{hold} is the creep "testing" temperature. All beams were held at T_{max} for 2 minutes unless otherwise noted.

Experimental data for the first thermal cycle of the Au/Si microcantilevers is shown in Figure 3.4 [45]. In Figure 3.4 the solid dots represent incremental *in-situ* measurements during heating and cooling. In creating Figure 3.4, the temperature was increased to a respective T_{max} value and then decreased to room temperature (25 °C). The value of T_{max} was progressively increased by 25 °C each loading cycle. From a microcantilever design perspective, the plot in Figure 3.4 forms a design space whereby the final curvature of the microcantilever can be can be tailored by adjusting T_{max}. Coupled with a particular beam length, the curvature dictates the gap between the beam and the substrate as well as the tip displacement during actuation. The linear loading and unloading lines can be predicted by considering the thermo-elastic nature of the bimaterial microcantilever [52]. The transition from the initial linear curve during heating and the non-linear flattening of the curvature-temperature response occurs precisely in the temperature range for Au film deposition, 70 °C to 110 °C. It is also worthwhile to note that just past the onset of the nonlinear curvature-temperature response, the curvature rises above zero. In later experiments, the curvature is observed to rise as high as 35 1/m during the initial heating cycle, depending on temperature and hold time. We also conducted a thermal cycling experiment between 25 °C and 190 °C on a bare 3.5 μm polysilicon microcantilever. As expected, the curvature did not change during the thermal cycle, but remained at a constant value of 5 1/m. Consequently, the relaxed curvature of the bare polysilicon layer, with equilibrated stresses, is expected to be approximately 5 1/m.

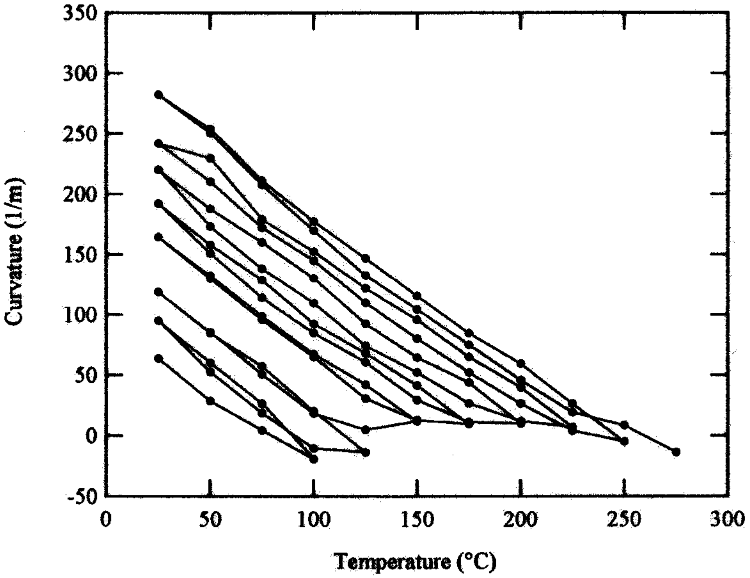

Figure 3.4. Curvature versus temperature as a function of progressively increasing maximum temperature values.

The initial thermal cycle of four duplicate chips is shown in Figure 3.5. The purpose of this plot is to highlight the chip-to-chip variation in the results. The different data points correspond to curvature-temperature measurements on chips all brought to T_{max} = 190 °C to be subsequently cooled to various T_{hold} values. Since the chips show nominally similar responses up to their respective hold temperatures, any variation in the hold behavior is an artifact of the hold conditions. Note that the overall behavior of the chip brought to T_{max} = 190 °C and cooled to T_{hold} = 30 °C envelopes the response of the beam in Figure 4 which includes intermittent thermo-elastic heating and cooling.

Plots of curvature versus time for T_{max} = 190 °C and various T_{hold} values ranging from 30 °C to 150 °C are presented in Figure 3.6. The two different graphs in Figure 3.6 show the results of identical experiments on duplicate chips, showing the same overall trends. The curvature-temperature plots in Figure 3.6 show a decrease in curvature over time up to a hold temperature of approximately 150 °C. The curvature of the beam held at 150 °C decreases a small amount at the beginning of the test and then slowly increases during the remainder of the testing period. Even the beam held near room temperature exhibits a fairly large change in curvature over the 200 hour time period. The different curvature values at the onset of the tests are consistent with the thermo-elastic cooling response of the chips brought to different T_{hold} values in Figure 3.5. In general, the curvature drop over time does not change dramatically with an increase in temperature. Several other experiments were conducted to explore the trends in Figure 3.6, particularly the unique behavior of the beam held at 150 °C.

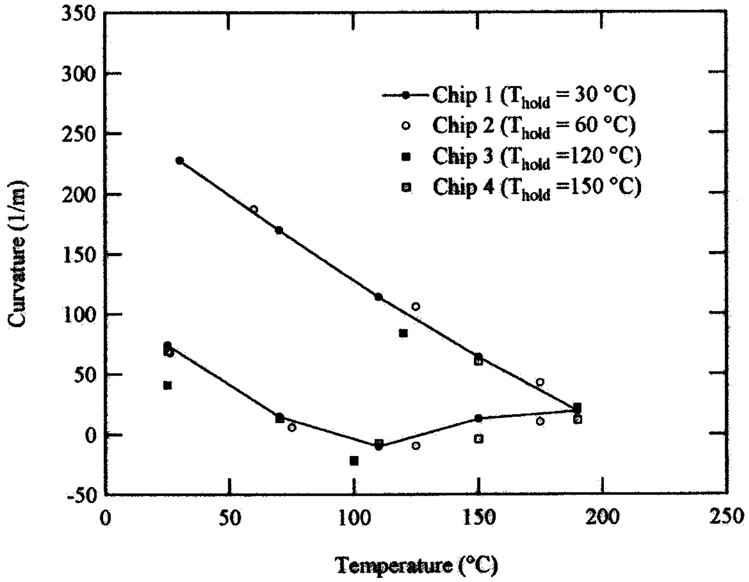

Figure 3.5. Repeatability of the initial curvature versus temperature response in four duplicate chips used in thermal holding experiments.

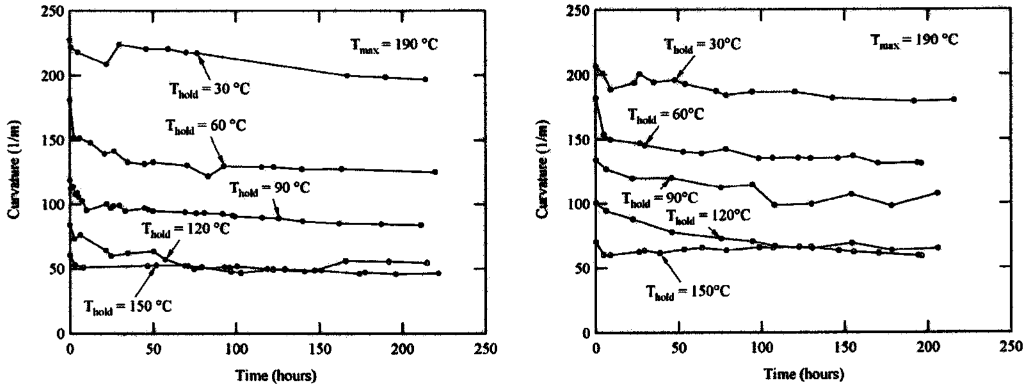

Figure 3.6. Curvature versus time for a maximum temperature of 190 °C and various hold temperatures. The two different graphs show the results of identical experiments conducted on duplicate chips.

Since the beam held at 150 °C did not exhibit a curvature drop at longer times, a complimentary test was conducted with a 400 minute hold at T_{max} = 190 °C rather than the 2 minute hold employed for other measurements (Figure 3.7). During the 400 minute hold at T_{max} = 190 °C the curvature increased approximately 20 1/m, as evident from the different initial curvature values for the two tests in Figure 3.7. The beam subjected to the longer annealing time at 190 °C shows a steady curvature drop during the test, in contrast to the beam given a two minute hold at 190 °C. Towards the end of the test (Figure 3.7) the curvature of the two beams intersects.

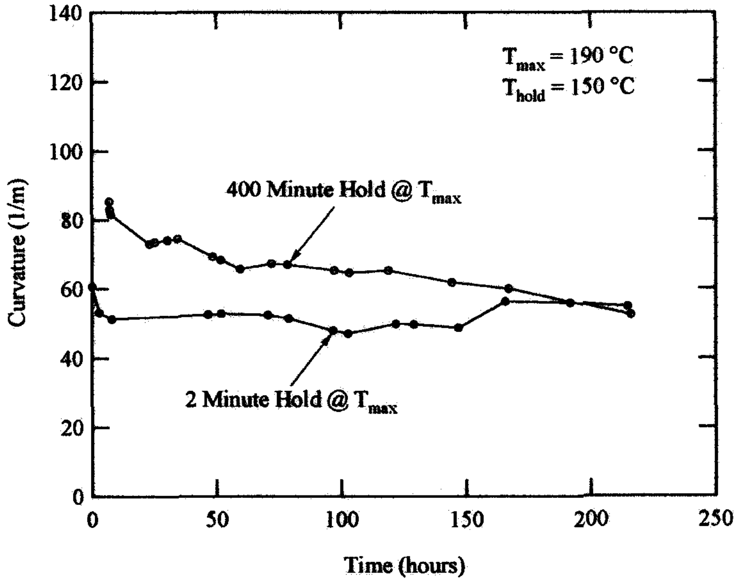

Figure 3.7. Curvature versus time for a hold temperature of 150 °C and two different hold times at 190 °C.

Two other experiments were conducted to explore the effect of T_{max} on the subsequent curvature drop in the beams during creep tests. In Figure 3.8, results are presented for two different T_{max} and T_{hold} values.

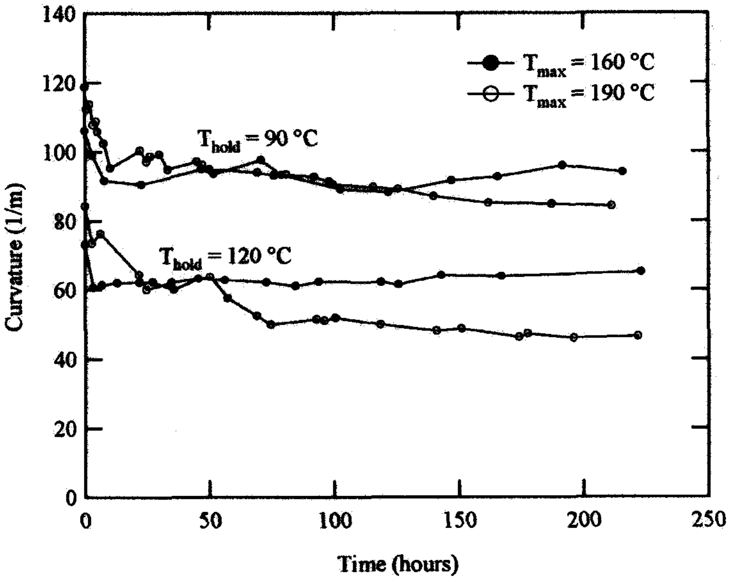

Figure 3.8 Curvature versus time for two different hold times and two different maximum temperatures.

The rate of curvature drop is higher for the beams brought to the higher T_{max}, for both hold temperatures. This result may be expected during the early stages of holding since the curvature, and the thermo-elastic Au film stresses, are higher in the beams brought to a higher T_{max} value. However, at longer hold times, the curvature in the beams brought to T_{max} = 190 °C passes the beams brought to T_{max} = 160 °C. The beams brought to T_{max} = 160 °C only show creep at the very beginning of the thermal hold; for the remainder of the hold, the curvature slightly increases or is or stable. The response of the beams brought to T_{max} = 160 °C in Figure 3.8 is very similar to the beam held at 150 °C in Figure 3.6. The crossing of the creep curves in Figure 3.8 is a repeatable result confirmed on several duplicate chips and beams. Apparently, from the results in Figure 3.8, the annealing temperature, T_{max}, has an effect on the thermal holding behavior aside from increasing the initial Au film stress and microcantilever curvature.

In Figure 3.9, the experiments presented in Figure 3.8 are tested in the limit where T_{max} is equal to T_{hold}.

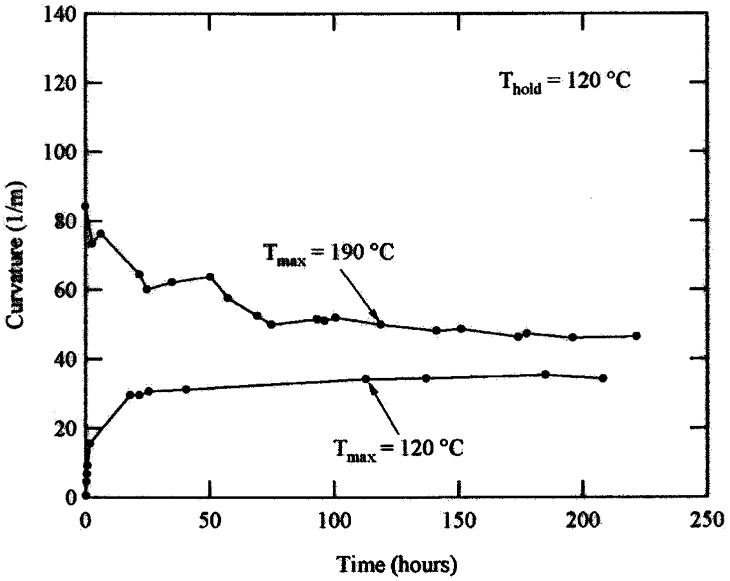

Figure 3.9. Curvature versus time for a hold temperature of 120 °C and two extreme maximum temperatures.

In one experiment, a beam was brought to a T_{max} value of 190 °C and then cooled to a T_{hold} value of 120 °C. In a companion experiment, a beam was brought to a T_{max} value of 120 °C and then held at 120 °C. One of the beams shows a gradual decrease in curvature as a function of time while the other beam shows a gradual increase in curvature as a function of time (Figure 3.9). The beam showing the increase in curvature is particularly interesting since the increase brings the beam away from the equilibrium curvature of the polysilicon layer and thus results in an increase in average tensile stress in the metallic layer. The increase in curvature for beams held under T_{max} = T_{hold} conditions is further explored in Figure 3.10 for extreme temperatures of 90 °C and 190 °C. From Figure 3.10, one observes that the increase in curvature occurs in the same manner, but at dramatically different rates at 90 °C and 190 °C. At 190 °C, an equivalent curvature increase can be realized more than an order of magnitude faster than at 90 °C. This anomalous increase in curvature, which is operating at all relevant temperatures, plays an important role in the creep and stress relaxation of the bimaterial microcantilevers.

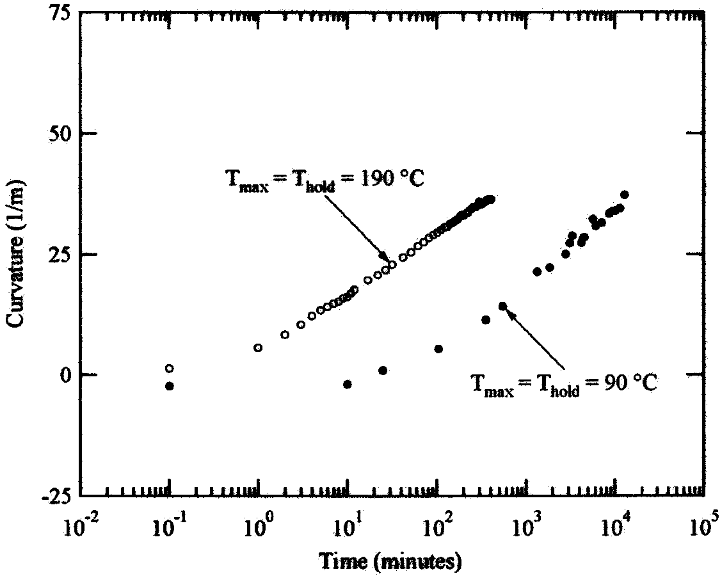

Figure 3.10. Curvature versus log time at two extreme temperatures. At both extremes, the maximum and hold temperatures are equivalent.

This observation is in contrast to traditional thin film-thick substrate *thermal cycling studies* where inelastic strains typically bring the curvature towards a zero curvature point from either the tensile or compressive film stress side, but does not result in the generation of stress [34-36].

Figure 3.11 is a final experiment comparing the hold behavior at T_{hold} = 150 °C and 180 °C, for T_{max} = 190 °C. The behavior of the beam held at 180 °C is much different than beams held at lower temperatures. The beam initially experiences an increase curvature followed by a rapid drop in curvature at longer hold times. Interestingly, the curvature drops below the equilibrium curvature in the Si, well into the negative curvature realm. The development of negative curvatures is again anomalous since this requires average tensile stress *generation* in the nominally flat Si layer (5 1/m) and average compressive stress *generation* in the Au layer. By definition, creep and/or stress relaxation in the Au layer cannot drive these stress increases.

Surface observations were performed with a FESEM on as-released and thermally treated Au cantilevers. Figure 3.12 is an image of the e-beam evaporated Au surface after release. The microstructure contains grains with an approximate size of 500 nm (Figure 3.12a) and a sub-grain texture with a size on the order 10-50 nm (Figure 3.12b). The two different magnifications are essential for elucidating the surface structure at different size scales. We also would like to note that preliminary cross-sectional Transmission Electron Microscopy (TEM) studies on as-released Au films on the microcantilevers have revealed a grain size on the order of the film thickness, an abundance of twins, dislocations, and a pore free structure beneath the surface layer.

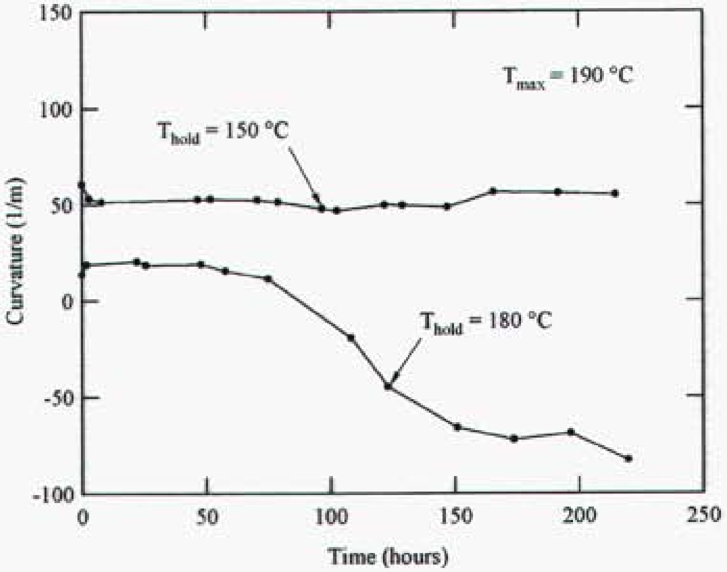

Figure 3.11. Curvature as a function of time for a beam held at 180 °C compared to a beam held at 150 °C. The maximum temperature was 190 °C in both experiments.

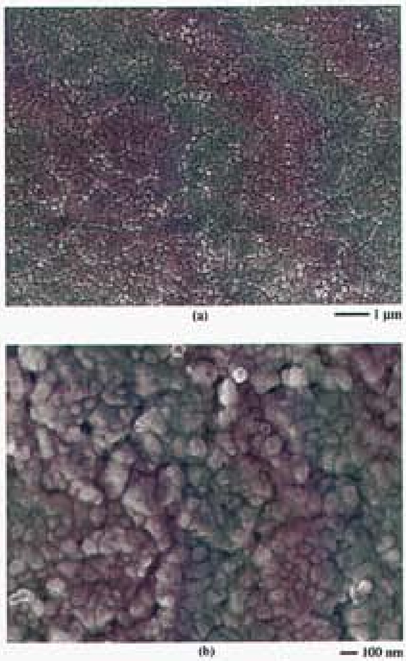

Figure 3.12. FE-SEM images of the as-released Au surface at (a) low and (b) high magnification.

Figure 3.13 presents SEM images of an Au surface on microcantilevers after being exposed to T_{max} = 190 °C and subsequently held at T_{hold} = 150 °C for 200 hours. For a hold temperature 150 °C and T_{max} = 190 °C, the surface structure of the material is basically unchanged from the as-released state (Figure 3.12) at the resolution of the FE-SEM. Images from beams held at temperatures lower than 150 °C also showed no detectable change in surface structure.

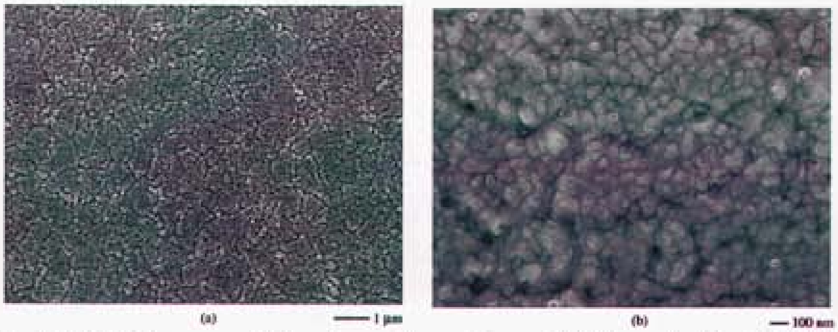

Figure 3.13. FE-SEM images of the Au surface after a 200 hour hold at 150 °C at (a) low and (b) high magnification. The beam was brought to a maximum temperature of 190 °C prior to holding.

Figures 3.14 and 3.15 present SEM images from the Au surface of microcantilevers held at 180 °C for 100 and 200 hours, respectively.

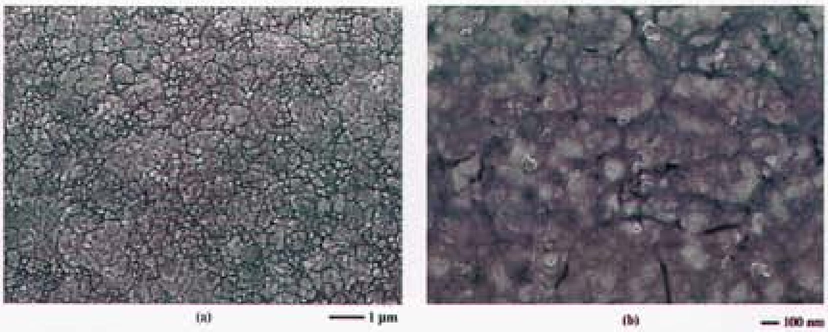

Figure 3.14. FE-SEM images of the Au surface after 100 hours at 180 °C at (a) low and (b) high magnification. The beam was brought to a maximum temperature of 190 °C prior to holding.

In the case of the higher temperature hold, the sub-grain texture coarsens and grooving occurs at the grain boundaries. In addition, hillocks grow out of the Au film, as seen at the top of Figure 3.15a. The appearance of observable microstructural changes in the Au films held at 180 °C is consistent with the anomalous curvature evolution in the beams held at 180 °C (Figure 11). Figure 3.16 presents tilted side view images from (a) an as-released beam and (b) a beam brought to T_{max} = 190 °C and subsequently held at T_{hold} = 180 °C for 200 hours. These images highlight the formation of regular hillocks at the Au surface.

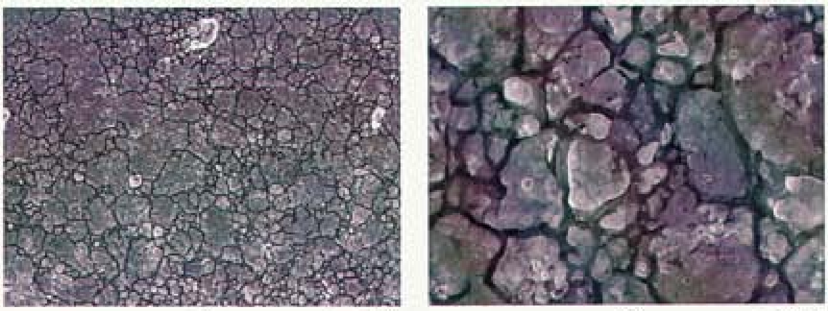

Figure 3.15. FE-SEM images of the Au surface after 200 hours at 180 °C at (a) low and (b) high magnification. The beam was brought to a maximum temperature of 190 °C prior to holding.

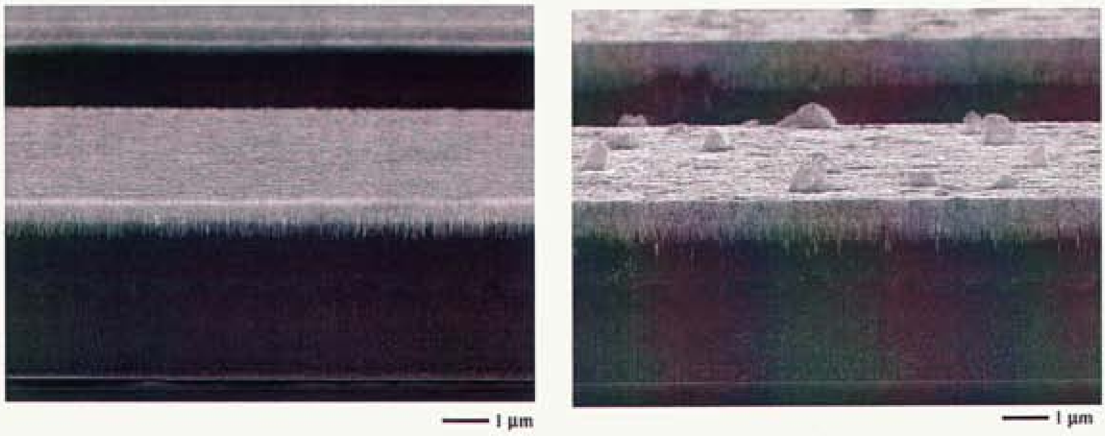

(a) (b)

Figure 3.16. Side view FE-SEM images of the beams (a) as-released and (b) after 200 hours at 180 °C. The Au layer is on the tops while the two different polysilicon layers are apparent. The samples are tilted at slightly different angles so the film thicknesses appear different.

3.4 Discussion

The curvature evolution of bimaterial microcantilevers as a function of time is likely dominated by inelastic strains in the Au film. The Si layer is assumed to be relatively inactive during temperature holds since it has a relatively higher melting temperature and ceramics typically posses a much higher creep resistance compared to metals – recall the Si was annealed at 1050 °C. The accumulation of inelastic tensile creep strains in the Au layer results in an overall expansion of the Au, a decrease in curvature (Figure 3.1), and stress relief in both the Si and Au layers. As a consequence, the creep behavior of bimaterial cantilevers is self-limiting since the accumulation of creep strains decreases the stresses in the Au layer, reducing the driving force for creep. In fact, the active creep mechanism depends on the relative combination of stress and temperature experienced by the material as evident in deformation mechanism maps [47]. Therefore, it is possible for the creep of bimaterial beams to be driven by different deformation mechanisms if the stresses in the Au film sufficiently relax.

To help understand the creep results, it is critical to quantify the relative magnitude of the film stresses in the bimaterial beams. Since the film stresses are not uniquely related to curvature, these stresses are only used as a relative guide rather than for presentation of the results as is commonly done in thin film – thick substrate studies. In Table 3.1 we present an overview of the temperatures and approximate stress values in the Au layer of the beams at the onset of the creep tests, time = 0. The melting temperature (T_m = 1338 K) and shear modulus (μ = 32 GPa) for bulk Au were used in all normalizations. The average tensile stress in the Au film, σ_{ave}, at the onset of the creep tests was calculated by assuming no stress at zero curvature and a temperature of T_{max} = 190 °C. The stress was then estimated at a given hold temperature by assuming the accumulation of stress during cooling at a rate of 1 MPa/°C from recent calculations [44]. The stress value employed is an average value even though a stress gradient exists in the Au film [44]. The average stress is converted to deviatoric stress, σ_s, by dividing by $\sqrt{3}$.

Table 3.1. Homologous temperatures, estimated initial stress values, and normalized shear stress values in the Au film for the various hold tests.

T_{hold} (°C)	T_{hold}/T_m (K/K)	σ_{ave} (MPa) @ time = 0	σ_s/μ
30	0.23	160	2.9×10^{-3}
60	0.25	130	2.3×10^{-3}
90	0.27	100	1.8×10^{-3}
120	0.29	70	1.3×10^{-3}
150	0.32	40	7.2×10^{-4}
180	0.34	10	1.8×10^{-4}

Recently, a creep deformation mechanism map has been constructed for freestanding thin film FCC Cu with a 3 μm grain size [16]. On this map [16], the data in Table 3.1 closely follows the constant creep rate contours for the freestanding Cu films. This overlay of the present stress-temperature data and previous work on freestanding Cu thin films may explain why the curvature changes in Figure 3.6 are not strongly dependent on T_{hold} for 30 °C < T_{hold} < 120 °C. The overall curvature drops at 200 hours for the four experiments at T_{hold} = 30 °C, 60 °C, 90 °C, and 120 °C were 31 1/m, 55 1/m, 35 1/m, and 37 1/m, respectively (Figure 6). From this data it is reasonable to conclude the effects of stress and temperature on creep and stress relaxation balance each other over the ranges experienced by the Au in Table 3.1. On the other hand, the behavior of the beams held at 150 °C and 180 °C deviates from the curvature evolution trends seen in beams held at lower temperatures. In particular, the beam held at 150 °C shows almost no curvature drop while the beam held at 180 °C shows a drastic drop in curvature (Figure 3.11).

The unique curvature evolution of the beams held at 150 °C and 180 °C are the result of intrinsic stress development from microstructural changes (different mechanisms for both hold temperatures). For the beam held at 180 °C, this conclusion is drawn from the large changes observed on the Au surface (Figures 3.14 – 3.16) coupled with the tendency of the beam to pass the equilibrium curvature value of the Si (5 1/m) and generate stresses (Figure 3.11). If extrinsic stresses, such as those induced in the Au and Si by thermal mismatch, drove the curvature drop in the beam held at 180 °C, the curvature would not be expected to become negative, but to approach 5 1/m. The driving force to bend the Si in a negative direction must come from microstructurally forced expansion of the Au. The higher resolution FESEM image of the Au surface (Figure 3.15b) reveals the apparent removal of atoms in the grain boundaries close to the surface. These "corner" atoms are either migrating towards the Au/Si interface or towards the surface of grains. Migration of Au atoms towards the interface would effectively lengthen the Au film and result in the development of negative curvature. The driving force for the diffusion of the atoms in the boundaries is currently unclear. Side view images of the beams after the high temperature hold showed the formation of Hillocks in addition to the aforementioned microstructural coarsening mechanisms (Figure 3.16). Hillock formation generally occurs in an effort to relive compressive film stresses [37, 38]. In this sense, the hillocks are helping to relieve the compressive stresses generated by the aforementioned microstructural coarsening mechanisms during the thermal hold.

The beams held at 150 °C show no curvature drop after a few hours, and even begin to show a gradual increase in the curvature. This experiment, along with others to be discussed, reveals a counterbalancing effect to the creep and stress relaxation of the Au films. This counterbalancing process acts to generate curvature and stress away from the equilibrium curvature of the Si, consequently, it is likely driven by thermally activated microstructural changes. Moreover, the microstructural changes occur without observable evolution of the grain structure (Figure 3.13), in an apparent effort to lower the metastable energy state of the Au. Based on these observations, the process is considered a microstructural thermal "recovery" process. The thermal recovery process is most evident when creep and stress relaxation effects are minimized by lowering curvature and film stresses (Figure 3.9, 3.10), but is presumably active to some degree during all tests. The degree of recovery depends very strongly on the temperature and time (Figure 3.10), and is not likely strongly dependent on stress. At relatively low temperatures ($T < 175$ °C) and hold times, we propose that the time dependent inelastic strain, ε_{in}, of the Au films on the microcantilevers is governed by:

$$\varepsilon_{in} = \varepsilon_c(\sigma, T, t) - \varepsilon_r(T, t) \qquad (3.1)$$

In Equation 3.1, ε_c is the creep strain while ε_r is the recovery strain. The creep strain will change sign based on the applied stress, σ, but the recovery strain will always be subtracted from the total inelastic strain since it acts to spontaneously contract the film and generate positive curvature (Figures 3.1, 3.10). The form of Equation 3.1 is consistent with internal state variable plasticity [48] and temperature dependent constitutive laws that consider a hardening minus recovery format for bulk FCC metals [49]. We will now explain some of the experimental observations based on the above partitioning of the inelastic strain into creep and recovery components. Following this discussion we will present results from a finite element model of the microcantilever beams that uses a constitutive relationship for the Au based on Equation 3.1.

During an isothermal hold experiment, both the creep and recovery terms will be active. The curvature evolution as a function of time will depend on the relative dominance of one inelastic deformation mechanism over the other. At low temperatures and high stress values, creep rates are relatively high and will dominate over recovery rates. On the other hand, at low stress values and high temperatures, recovery rates will dramatically increase and can potentially overcome creep rates. For example, experiments on *as-released* Au/Si microcantilevers held at room temperature, $T_{max} = T_{hold} = 25$ °C, showed a gradual and significant increase in curvature over time, presumably due to recovery, for a hold period of a year [50]. Microcantilevers held at room temperature ($T_{hold} = 25$ °C) after a thermal annealing at $T_{max} = 180$ °C, showed a creep response over the year hold period, consistent with the results here [50]. The curvature increases (decreases) that can be caused by creep (recovery) in the Au films during 200 hour holds have similar orders of magnitude (Figure 3.9). Therefore it is reasonable that recovery in the Au film could serve to counter balance creep for a given combination of stress and temperature. As an example, in Figure 3.7, the beam held at 150 °C shows a very slight overall recovery response after being brought to 190 °C for 2 minutes but an overall creep response after being brought to 190 °C for 400 minutes. According to Figure 3.10, at 190 °C, 2 minutes is enough time to recover a curvature of 8 1/m while 400 minutes is enough time to recover a curvature of 36 1/m. The more complete exhaustion of the Au recovery, coupled with the increase in the average tensile Au film stress during recovery, leads to creep in the beam held for the longer time at $T_{max} = 190$ °C (Figure 3.7). The results in Figure 3.7 help to show the importance of Au recovery in determining the overall curvature change during hold experiments. However, the change in recovery in the experiment in Figure 3.7 is accompanied by a change in initial stress during holding so it is not obvious which change is driving the different response of the beam held at a higher T_{max}.

We believe that recovery in the Au layer dominates the deviation from linear thermo-elasticity observed during the initial thermal heating cycle (Figures 3.4 and 3.5). Recovery initiates near the substrate temperature during deposition (around 70 °C to 100 °C) and progressively increases as the temperature is raised to about 200 °C. At temperatures above 200 °C, such as 225 °C in Figure 3.4, the curvature-temperature response begins to move downwards, marking the end of the recovery period (Figure 3.4). The total amount of recovery due to inelasticity in the Au can be *estimated* by the difference in the curvature at a given temperature during the first thermal cycle and the curvature assuming thermo-elastic deformation during heating. With this, the amount of recovery expended during the first thermo-mechanical cycle will depend on the maximum temperature, and time at that maximum temperature. For example, if a beam is only brought to 160 °C, then the curvature expended due to recovery is smaller than the recovery expended for a beam brought to 190 °C. Based on the above, another advantage of the inelastic strain partitioning in Equation 3.1 is the potential to predict the initial thermo-mechanical cycle in addition to the creep behavior during subsequent holds.

The importance of the competition between creep and recovery in the Au film is most obvious in Figure 3.8. Since the results in Figure 3.8 are qualitatively the same for the two different hold temperatures, we focus here on the beams held at 120 °C. One of the beams was brought to 160 °C prior to cooling while the other was brought to 190 °C prior to cooling. The two maximum annealing temperatures will result in two differences in the beams. First, according to Figure 3.4, the initial curvature (average Au film stress) of the beam brought to a higher temperature will be higher, as is seen in Figure 3.8. Secondly, the beams brought to the higher temperature will experience more recovery in the Au, partially expending this deformation mechanism for the subsequent creep test. During the thermal hold (Figure 3.8) the beam brought to 190 °C experiences more overall creep compared to the beam brought to 160 °C. The curvatures even pass each other around 50 hours, and the beam brought to 190 °C creeps faster despite a smaller stress level. The results in Figure 3.8 decisively demonstrate that recovery in the beam is very critical to determining the overall curvature response during a thermal hold.

The final experimental results to be discussed are presented in Figure 3.11. In Figure 3.11, the curvature evolution at 180 °C demonstrates the rapid exhaustion of recovery in the Au and the subsequent dominance of yet another mechanism dictated by different microstructural evolution. Prediction of the curvature evolution for the 180 °C hold would require the creep and recovery terms in Equation 3.1, along with *another* term to account for the drop in curvature below the equilibrium Si curvature resulting in the generation of average compressive Au film stresses. The incorporation of numerous inelastic strain terms to account for various competing microstructural mechanisms is addressed in the framework of internal state variable theory for metals [48, 49]. Based on the current experiment, it is not certain if the new mechanism operating in the beams held at 180 °C will activate during long holds in beams held at moderate temperatures. However, the curvature response of the beam held at 180 °C does prove that the beams showing a relatively flat curvature time response, can expend the Au recovery and may begin to experience curvature changes during longer hold periods.

The present results provide some insight into the mechanisms controlling both creep and recovery in the Au. From preliminary studies on Au/Si microcantilevers, we know that a ceramic passivation layer will completely suppress creep [19] but have less effect on recovery [45] in the Au layer. The suppression of creep by the passivation layer may imply either a mitigation of surface diffusion or a decrease in dislocation mobility due to surface drag and repelling dislocation image forces. Recent results on thin film Cu [39] concluded that power-law dislocation based creep, by itself, could predict the thermo-mechanical response of passivated films. On the other hand, they revealed that predicting the thermo-mechanical response of unpassivated films required both grain boundary and surface diffusion coupled with a model accounting for dislocation activity. In the Au/Si microcantilevers, it is possible that a combined surface diffusion and dislocation creep model is necessary for predicting the evolution of creep strain, ε_c. Such a combined model seems particularly important since the normalized temperature and stress values lie near the border of power law and diffusional creep regimes on a deformation mechanism map for FCC films [16].

The mechanism responsible for recovery in the Au is linked to the metastable as-deposited structure of the Au. Possibilities for intrinsic stress development due to recovery include grain growth [29-32, 41], dislocation annihilation [41], or possibly twin boundary motion (twins were discovered in the as-released Au film). Currently, transmission electron microscopy (TEM) studies are being performed to ascertain the active deformation mechanism during recovery. Recent TEM studies [41] have show that during thermal exposure, dislocation annihilation rate decreases and diffusional processes become dominant. This observation is consistent with our concept of the recovery being exhaustible for a given exposure to temperature and time. Moreover, a very new study has observed yielding and flow in thin Cu films near zero stress during the first thermomechanical cycle, similar to the curvature-temperature response observed here [51]. The authors in [51] attributed the anomalous thermo-mechanical behavior to the recovery of misfit dislocations.

3.5 Conclusions

1. Bimaterial Au/Si microcantilevers subjected to an isothermal hold experience changes in curvature as a function of time. The curvature of the microcantilever is observed to increase, decrease, and/or remain stable depending on hold time, hold temperature, and maximum annealing temperature. Creep, stress relaxation, recovery, and microstructural coarsening (with hillock formation) in the metallic Au layer control the complex curvature evolution in the bimaterial microcantilevers.

2. At relatively low hold temperatures, 30 °C < T < 175 °C, the inelastic response of the Au film is a combination of creep and recovery. Tensile creep strains in the Au film, at relatively low temperatures and high stresses, results in a drop in positive curvature and a decrease in tensile film stresses. Due to thermo-elastic cooling of the Au/Si bimaterial structures, the stress in the Au layer is larger (smaller) for creep tests performed at lower (higher) temperatures. Consequently, the creep rate of the beams is rather independent of hold temperature up to 120 °C.

3. Recovery in the Au film serves to contract the Au, increase curvature, and result in increased intrinsic tensile stresses in the film. The recovery process is controlled primarily by temperature and time, and recovery becomes significant at moderate hold temperatures (120 °C < T < 175 °C). The amount of recovery in the Au depends on the maximum annealing temperature and recovery can be expended during initial thermal exposure. The relative amount of recovery expended prior to and during a creep test influences the overall curvature evolution in the beams. For particular combinations of thermal annealing treatment and thermal holding, recovery balances the creep and minimal change in curvature is observed over time.

4. At relatively high hold temperatures (T > 175 °C), recovery is rapid and the curvature evolution is dominated by observable microstructural coarsening and hillock formation. The microstructural coarsening is marked by the depletion of the atoms from the region where the grain boundaries intersect the surface. The aforementioned process results in an effective lengthening of the Au film and significant negative curvature development.

3.6 Acknowledgements

A Navy Fellowship supported Neil West during this research.

3.7 References

[1] T. Perazzo, M. Mao, O. Kwon, A. Majumdar, J. B. Varesi, P. Norton, "Infrared vision using uncooled micro-optomechanical camera." *App. Phys. Lett.*, vol. 74 (23), pp. 3567-3569, 1999.

[2] L. R. Senesac, J. L. Corbeil, S. Rajic, N. V. Lavrik, P. G. Datskos, "IR imaging using uncooled microcantilever detectors." *Ultramicroscopy*, vol. 97 (1-4), pp. 451-458, 2003.

[3] P. G. Datskos, S. Rajic, I. Datskou, "Detection of infrared photons using the electronic stress in metal-semiconductor cantilever interfaces." *Ultramicroscopy*, Vol. 82 (1-4): pp. 49-56, 2000.

[4] M. Alvarez, A. Calle, J. Tamayo, L. M. Lechuga, A. Abad, A. Montoya, "Development of nanomechanical biosensors for detection of the pesticide DDT." *Biosens. Bioelec.*, vol. 18 (5-6): pp. 649-653, 2003.

[5] D. R. Baselt, B. Fruhberger, E. Klaassen, S. Cemalovic, C. L. Britton, S. V. Patel , T. E. Mlsna, D. McCorkle, B. Warmack. "Design and performance of a microcantilever-based hydrogen sensor" *Sens. Act. B*, vol. 88 (2): pp. 120-131, 2003.

[6] Z. Y. Hu, T. Thundat, R. J. Warmack RJ, "Investigation of adsorption and absorption-induced stresses using microcantilever sensors" *J. App. Phys*, vol. 90 (1): pp. 427-431, 2001.

[7] C. L. Chang and P. Z. Chang, "Innovative micromachined microwave switch with very low insertion loss." *Sens. Act. A*, vol. 79 (1): pp. 71-75, 2000.

[8] D. C. Miller, W. G. Zhang, V. M. Bright, "Micromachined, flip-chip assembled, actuatable contacts for use in high density interconnection in electronics packaging" *Sens. Act. A*, vol. 89 (1-2): pp. 76-87, 2001.

[9] J. Varesi, J. Lai, T. Perazzo, Z. Shi, A. Majumdar, "Photothermal measurements at picowatt resolution using uncooled micro-optomechanical sensors" *App. Phys. Lett.*, vol. 71 (3): pp. 306-308, 1997.

[10] S. Baglio, S. Castorina, L. Fortuna, N. Savalli, "Modeling and design of novel photo-thermo-mechanical microactuators." *Sens. Act. A*, vol. 101 (1-2): pp. 185-193, 2002.

[11] H. K. Xie, Y. T. Panc, and G. K. Fedder, "Endoscopic optical coherence tomographic imaging with a CMOS-MEMS micromirror." *Sens. Act. A*, vol. 103 (1-2): pp. 237-241, 2003.

[12] S. Schweizer, P. Cousseau, G. Lammel, S. Calmes, P. Renaud, “Two-dimensional thermally actuated optical microprojection.” *Sens. Act. A*, vol. 85 (1-3): pp. 424-429, 2000.

[13] S. Schweizer, S. Calmes, M. Laudon, P. Renaud P, “Thermally actuated optical microscanner with large angle and low consumption,” *Sens. Act. A*, vol. 76 (1-3): 470-477, 1999.

[14] G. Greitmann, R. A. Buser, “Tactile microgripper for automated handling of microparts,” *Sens. Act. A*, 53 (1-3): 410-415, 1996.

[15] R. J. Linderman, P. E. Kladitis, and V. M. Bright, “Development of the micro rotary fan,” *Sens. Act. A*, vol. 95 (2-3): 135-142, 2002.

[16] H. Huang, “Mechanical Properties of Free-Standing Polycrystalline Metallic Thin Films and multilayers,” PhD Thesis, Harvard University, 1998.

[17] K. E. Harris and A. H. King, “Direct Observation of Diffusional Creep via TEM in polycrystalline thin films of gold.” *Acta. Mater.*, vol. 46(17), pp. 6195-6203, 1998.

[18] Y. Zhang and M. L. Dunn, “Stress Relaxation and Creep of Gold/Polysilicon Layerd MEMS microstructures Subjected to Thermal Loading,” Proc. ASME, Nov. 11-16, New York, NY, 2001.

[19] Y. Zhang, M. L. Dunn, J. E. Elam, and S. M. George, “Suppression of Stress Relaxation in MEMS Multilayer Film Microstructures by Use of ALD Nanocoatings,” Proc. ASME, Nov. 17-22, New Orleans, LA, 2002.

[20] M. A. Haque and M. T. A. Saif, “Application of MEMS force sensors for in situ mechanical characterization of nano-scale thin films in SEM and TEM.” *Sen. Act. A,* vol. 97 (8), pp. 239-245, 2002.

[21] I. De Wolf and W. M. van Spengen, “Techniques to study the reliability of metal RF MEMS capacitive switches.” *Microelec. Relab.,* vol. 42 (9-11), pp. 1789-1794, 2002.

[22] A. J. Kalkman, A. H. Verbruggen, G. C. A. M. Janssen, and S. Radelaar “Transient Creep in Free-Standing Thin Polycrystalline Aluminum Films.” *J. App. Phys.,* vol. 92 (9), pp. 4968-4975, 2002.

[23] K. P. Larsen, A. A. Rasmussen, J. T. Ravnkilde, M. Ginnerup, O. Hansen, “MEMS device for bending test: measurements of fatigue and creep of electroplated nickel” *Sen. Act. A,* vol. 103 (1-2): pp. 156-164, 2003.

[24] H. S. Cho, K. J. Hemker, K. Lian, J. Goettert, G. Dirras, “Measured mechanical properties of LIGA Ni structures.” *Sen. Act. A,* vol. 103 (1-2): pp. 59-63, 2003.

[25] R. D. Emery and G. L. Povirk, “Tensile behavior of free-standing gold films. Part I. Coarse-grained films.” *Acta. Mater.*, vol. 51, pp. 2067-2078, 2003.

[26] R. D. Emery and G. L. Povirk, “Tensile behavior of free-standing gold films. Part II. Fine-grained films.” *Acta. Mater.*, vol. 51, pp. 2079-2087, 2003.

[27] K. Gall, M. L. Dunn, Y. Zhang, and B. Corff, “Thermal Cycling Response of Layered Gold/Polysilicon MEMS Structures.” *Mechanics of Materials*, vol. 36 (1-2), pp. 45-55, 2004.

[28] W. D. Nix, “Mechanical properties of Thin Films.” *Metall. Trans.*, vol. 20A, pp. 2217-2245, 1989.

[29] W. D. Nix and B. M. Clemens, “Crystallite Coalescence: A mechanism for intrinsic tensile stresses in thin films.” *J. Mat. Res.*, vol. 14 (8), pp. 3467-3473, 1999.

[30] S. C. Seel, C. V. Thompson, S. J. Hearne, and J. A. Floro, "Tensile stress evolution during deposition of Volmer-Weber thin films." *J. App. Phys.*, vol. 88(12), pp. 7079-7088, 2000.

[31] C. V. Thompson, "Structure evolution during processing of polycrystalline films." *Ann. Rev. Mater. Sci.*, vol. 30, pp. 159-190, 2000

[32] S. C. Seel and C. V. Thompson, "Tensile stress generation during island coalescence for variable island-substrate contact angle." *J. App. Phys.*, vol. 93(11), pp. 9038-9042, 2003.

[33] U. Smith, N. Kristensen, F. Ericson, and J-A Schweitz, "Local Stress relaxation Phenomenon in Thin Aluminum films." *J. Vac. Sci. Tech.*, vol. 9(4), pp. 2527-2535, 1991.

[34] R. P. Vinci, E. M. Zielinski, and J. C. Bravman, "Thermal Stress and Strain in copper thin films." *Thin Sol. Films,* vol. 262, pp. 142-153, 1995.

[35] H. Gao, L. Zhang, W. D. Nix, C. V. Thompson, and E. Arzt, "Crack-like Grain-Boundary Diffusion Wedges in thin metal films." *Acta. Mater.*, vol. 47(10), pp. 2865-2878, 1999.

[36] R. M. Keller, S. P. Baker, E. Arzt, "Stress-temperature behavior of unpassivated thin copper films" *Acta mater,* vol. 47 (2): pp. 415-426, 1999.

[37] D. Kim, W. D. Nix, M. D. Deal, J. D. Plummer, "Creep-controlled diffusional hillock formation in blanket aluminum thin films as a mechanism of stress relaxation." *J. Mater. Res,* vol. 15 (8): pp. 1709-1718, 2000.

[38] D. Kim, B. Heiland, W. D. Nix, E. Arzt, M. D. Deal, J. D. Plummer, "Microstructure of thermal hillocks on blanket Al thin films." *Thin Solid Films,* vol. 371 (1-2): pp. 278-282, 2000.

[39] D. Weiss, H. Gao, E. Arzt, "Constrained diffusional creep in UHV-produced copper thin films." *Acta Mater.*, vol. 49 (13): pp. 2395-2403, 2001.

[40] M. J. Kobrinsky, C. V. Thompson, and M. E. Gross, "Diffusional creep in damascene Cu lines." *J App. Phys.*, vol. 89 (1): pp. 91-98, 2001.

[41] M. Legros, K. J. Hemker, A. Gouldstone, S. Suresh, R. M. Keller-Flaig, E. Arzt, "Microstructural evolution in passivated Al films on Si substrates during thermal cycling," *Acta Mater.*, vol. 50 (13): pp. 3435-3452, 2002.

[42] D. Josell and F. Spaepen, "Determination of the interfacial tension by zero creep experiments on multilayers. 1 theory," *Acta. Metall. Mater.*, vol. 41 (10), pp. 3007-3015, 1993.

[43] D. Josell and F. Spaepen, "Determination of the interfacial tension by zero creep experiments on multilayers. 2 experiemnts," *Acta. Metall. Mater.*, vol. 41 (10), pp. 3017-3027, 1993.

[44] M. L. Dunn, Y. H. Zhang, V. M. Bright, "Deformation and structural stability of layered plate microstructures subjected to thermal loading," *J. MEMS*, vol. 11 (4): pp. 372-384, 2002.

[45] K. Gall, M. Hulse, M. L. Dunn, D. Finch, S. M. George, and B. A. Corff, "Thermomechanical response of bare and Al2O3-nanocoated Au/Si bilayer beams for microelectromechanical systems," *J. Mater. Res.*, vol. 18 (7): pp. 1575-1587, 2003.

[46] D. A. Koester, R. Mahadevan, B. Hardy, and K. W. Markus, 2001, MUMPs Design Rules, Cronos Integrated Microsystems, A JDS Uniphase Company, http://www.memsrus.com.

[47] H. F. Frost and M. F. Ashby, "Deformation Mechanism Maps", Pergamon Press, London, 1982.

[48] J. R. Rice, "Inelastic Constitutive Relations for Solids – An Internal Variable Theory and its Applications to Metal Plasticity," *J. Mech. Phys. Solids.*, vol. 19 (6): pp. 433, 1971.

[49] A. B. Tanner, R. D. McGinty, and D. L. McDowell, "Modeling temperature and strain rate history effects in OFHCCu." *Int. J. Plas.*, vol. 15 (6): pp. 575-603, 1999.

[50] D. C. Miller, "Micromachined, Flip-Chip Assembly, Actuatable, Normally-Closed Contacts for Use in High-Density Electronics Packaging", MS Thesis, University of Colorado, 2000.

[51] S. P. Baker, R. M. Keller-Flaig, and J. B. Shu, "Bauschinger effect and anomalous thermomechanical deformation induced by oxygen in passivated thin Cu films on substrates." *Acta. Mater.*, vol. 51 (10): pp. 3019-3036, 2003.

[52] Y. Zhang and M. L. Dunn, "Deformation of Blanketed and Patterned Bilayer Thin Film Microstructures During Post-Release Thermal and Cyclic Thermal Loading," *J. MEMS*, vol. 12 (6), pp. 788-796, 2003.

4 The Strength of Gold Nanowires

Atomistic simulations are used to investigate the yield strength of experimentally observed atomic and nanometer scale gold wires. The atomistic predictions of strength are quantitatively consistent with discrete experimental measurements and they reveal the mechanisms for increasing nanowire strength with decreasing dimensional scale. Distinct transitions in yield strength and yield mechanism are discovered. At nanometer scales (diameter > 1 nm), the mechanism for strengthening involves the scarcity and low mobility of dislocations coupled with constraint from tensile surface stresses. As the wires approach the atomic scale (diameter < 1 nm), an increase in strength occurs concurrent with a surface-stress-induced change in the stable structure of the nanowires and the absence of dislocation-mediated yield. The results constitute a new fundamental understanding of strength in metallic nanowires spanning technologically relevant dimensional scales.

4.1 Introduction

Strength is one of the most fundamental and significant mechanical properties of a material; it measures the basic capacity to bear load. The yield, or fracture, of a material results in a decrease, or complete loss, of load bearing capacity and, in most cases, loss of functionality. Throughout history, the implementation of stronger materials in technology has assisted the development of smaller, lighter, faster, and more robust devices. Recent advances in experimental tools have facilitated strength measurements in metal nanowires and nanostructures down to single atomic chains[1-10]. The fledging field of nanotechnology provides motivation for a comprehensive understanding of the strength of materials down to nanometer and atomic scales. The realization of devices with nanometer scale elements hinges on the ability of low-dimension materials to sustain mechanical loads during fabrication, assembly, and operation.

For quite some time, theoreticians have opined that smaller is stronger[1]. That is, as the dimensional scale of a material is reduced, yield strength should increase accordingly. A collection of experimental yield strength measurements on 99.99% pure gold (Au) is presented in Figure 4.1[2-10]. In Figure 4.1, stress, the basis for measuring strength, is defined as force per unit cross sectional area[11]. Figure 4.1 reveals a substantial and systematic increase in measured strength with decreasing dimensional scale. Figure 4.1 includes classical and atomistic theoretical predictions of the "ideal" yield strength of bulk single crystal Au in the absence of crystalline defects[1,15]. The classical and ideal theoretical strength is considered an upper bound on yield strength since it is based on the coordinated shearing of two adjacent atomic planes in the absence of defect nucleation from surfaces or structural inhomogeneities[15].

In light of ideal strength predictions, the strength increase observed traversing the micrometer size scale is readily explained based on dislocation mechanics. Drawn microwires and deposited nanofilms both exhibit yield under applied stress[2-4], and possess yield strengths below ideal theoretical predictions for bulk single crystal Au

(Figure 4.1). In polycrystalline drawn metal whiskers or deposited thin films, the tiny grain size and small lateral dimensions restrict dislocation activity, driving an increase in yield strength relative to normal bulk materials. However, nanofilms and microwires ultimately experience dislocation-governed plasticity and thus their yield strength values are below the ideal theoretical values for bulk materials. As the dimensional scale of the Au samples approaches the nanometer range, processing techniques usually result in single crystal structures that demonstrate quantized plasticity or discrete yielding events[5-8]. The measured yield strength of the nanowires undergoing quantized plasticity is typically above theoretical predictions predicated on a seemingly more difficult coordinated shearing of atomic planes[15].

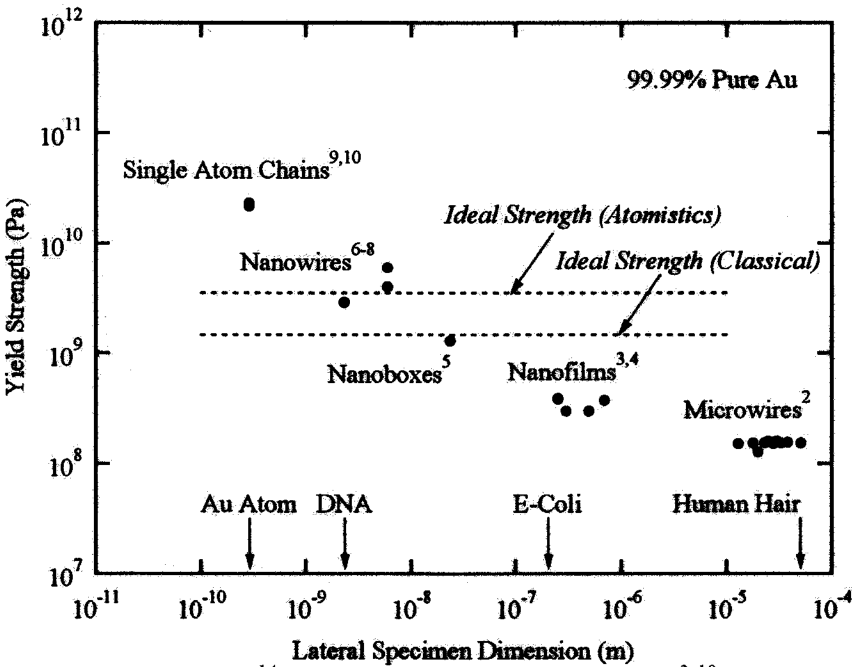

Figure 4.1. Ideal predictions[14] and experimental measurements[2-10] regarding the yield strength of 99.99% pure Au as a function of lateral specimen dimension. The data shows a systematic trend towards stronger materials as the lateral specimen dimension is reduced towards the atomic scale. At discrete experimental length scales, the materials in the nanometer to micrometer range all demonstrate yielding, while single atom chains undergo atomic separation. The relative sizes of various natural substances are included for reference.

The transition from the nanometer to atomic scale provokes another increase in strength and ultimately the departure of quantized yield behavior. As may be expected, single atom chains do not undergo yield *per se*, but rather experience ideal tensile atomic separation. Previous experimental[12,16-21] and theoretical[13,16,18,22-24] studies have examined the formation of a single atom chain through the necking of an atomic point contact. However, prior studies have not analyzed variations in stable nanowire strength with systematically decreasing cross sectional area approaching the single chain wire. As a result, yielding and strength in nanometer and atomic scale wires is not understood from a universal perspective. In particular, it is critical to understand the transition from experimentally observed quantized plastic flow in nanowires to perfect atomic separation in single atom chains.

We study the initial yield of atomic and nanometer scale Au wires using computational atomistic simulations. We focus on initial yield behavior since nanowires experience an instantaneous drop in load carrying capacity[5-8] and functionality, e.g. conductance[8,17-21], upon yielding. The aforementioned behavior contrasts that of bulk materials, which typically experience strain hardening after initial yield up to their ultimate tensile strength. In this sense, the initial yield point of nanowires is analogous to the ultimate tensile strength of bulk materials, both of which occur concurrent with geometric instability (necking). We consider three classes of Au wires which are stable at lateral dimensions spanning individual atoms to nanometers: (1) Atomic wires consisting of single atom chains[9,10,12,13], (2) Multishell wires with cylindrical or helical packing[25-28], and (3) Face-centered-cubic (fcc) <110> wires with a rhombic cross section and {111} transverse surfaces[25,29]. As indicated by respective references, the structural stability of the various wires has been confirmed by experimental observations. However, a seamless understanding of the mechanical behavior and yielding mechanisms for wires spanning these size scales does not exist.

4.2 Materials and Methods

With exception to the single atom chain predictions, all simulations were performed using the Embedded Atom Method (EAM)[30]. Simulation of a single atomic chain with EAM is questionable unless potentials are fit to properties relevant to these extreme low-coordination systems. Results for single atomic chains were extracted from a prior study using *ab initio* simulations[10]. In the EAM framework, the total energy of the atomic system is comprised of a pair potential term and an embedding energy term. The embedding energy is based on the energy required to place a host atom into the background electron density of surrounding atoms. The background electron density in EAM is composed of spherically averaged contributions from neighboring atoms. The EAM framework facilitates computation of relatively larger wires while still capturing electron density coordination *effects* critical to free surfaces and small wires. The EAM potentials for the present simulations were parameterized to fit the sublimation energy, equilibrium lattice constant, elastic constants, and vacancy formation energy in bulk Au[30].

The <110> nanowires were created by initially placing atoms in positions representative of a bulk fcc lattice. We then anneal the nanowires in a molecular dynamics framework by gradually raising the temperature from 2 K to about 300 K, holding, and then gradually lowering the temperature to 2 K. We then further relax the nanowire using an energy minimization method. Larger <110> nanowires retain their fcc structure during the entire process, while smaller nanowires form the experimentally observed multishell structure. The multishell structures generated this way are generally not uniform throughout the length. We examined the shell structures and then created wires with uniform shell structures. Finally, we annealed the wires to determine their equilibrium configurations.

Starting from the equilibrium configurations of the nanowires, we performed uniaxial tensile loading on the nanowires until yield. Specifically, we displaced all the atoms in accordance with a prescribed uniform strain in the length direction, fixed the length and then dynamically relaxed the nanowires at 2 K for 200 *ps* with a 0.004 *ps* per time step to obtain the equilibrium configurations of the nanowires at the prescribed strain. The equilibrium state of the nanowires was determined by allowing the stress to saturate as a function of time. The nanowires typically reach equilibrium after 100 *ps* and the stress averaged over the second 100 *ps* is used as the stress of the nanowires. We use the virial stress for a system of atoms, which is equivalent to the Cauchy stress in the average sense[31-34]. Atoms in the fcc structure were visualized according to the slip vector, which locates atoms that have sheared relative to one another, marking dislocations and stacking faults[35].

4.3 Results and Discussion

Three-dimensional perspective images of representative rhombic and multishell Au wires are shown in Figures 4.2a and 4.2b, respectively.

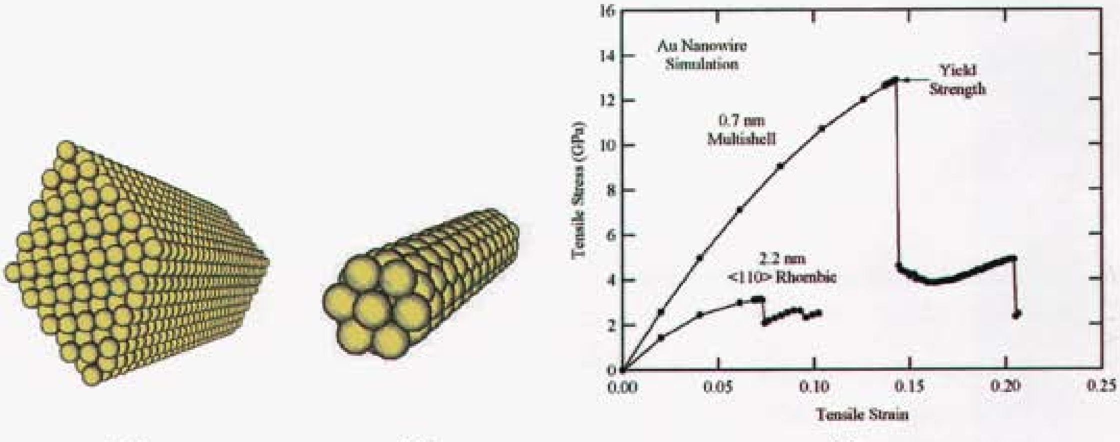

(a) (b) (c)

Figure 4.2. Equilibrium structures for two representative Au nanowires with different lateral dimensions: (a) Relaxed atomic positions of a 2.2 nm rhombic wire with a <110> axis orientation and {111} side surfaces. (b) Relaxed atomic positions of a 0.7 nm multishell wire. The tensile stress-strain responses of the nanowires in (a) and (b) are presented in (c).

Consistent with experimental observations, the wires in Figure 4.2 represent stable structures for respective sizes determined by "annealing" the wires, followed by energy minimization using embedded atom method potentials for Au[30]. The multishell wire in Figure 4.2b was predicted by annealing an original structure resembling a small <110> fcc wire. Although the rhombic wire in Figure 4.2a was created by initially placing atoms in their fcc positions with appropriate orientations, the atomistic model also predicts the formation of the low-energy rhombic wire in Figure 4.2a from a <100> wire through surface-stress-driven reorientation[29]. The rhombic and multishell structures are both highly stable configurations for nanowires because they minimize the total wire energy, which consists of a significant surface energy contribution.

Tensile stress-strain curves for the representative wires in Figures 4.2(a,b) are presented in Figure 4.2c. The rhombic and multishell wires show an elastic loading stage, characterized by monotonically increasing stress with increasing applied strain, followed by a yield point marked by a sudden stress drop. The elastic modulus (slope of the stress-strain curve) for the <110> wire is lower than the modulus of the multishell wire. The calculated elastic modulus of the <110> wire is consistent with continuum mechanics predictions at small strains for this orientation aside from differences due to the existence of the free surfaces and edges. At larger strains, both materials demonstrate nonlinear elasticity as predicted by the curvature in the atomic potential functions at larger atomic separations.

The incipient yield points in the nanowire stress-strain responses (Figure 4.2c) are defined as the yield strengths of the wires. Following yield, and the sudden stress drop, the wires undergo elastic deformation followed by additional yield events or so-called quantized plastic flow[8]. Based on the results in Figure 4.2c, the multishell nanowire is considerably stronger than the fcc rhombic nanowire. Figure 4.3 presents simulation predictions of nanowire yield strength as a function of lateral wire dimension.

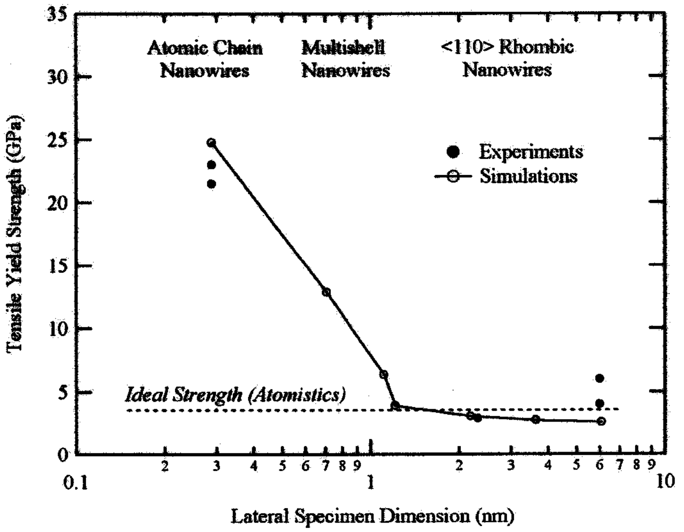

Figure 4.3. Experimental measurements and simulation predictions of tensile yield strength as a function of size scale. All simulation predictions are from an embedded atom model[29] with exception to the single atom chain predictions, which are from ab initio simulations[9]. Experimental measurements and the atomistic ideal strength prediction are the same as shown in Figure 4.1[5-9].

Relevant experimental measurements and ideal strength predictions from Figure 4.1 are included in Figure 4.3, and the stable wire structure is indicated along the top of the figure. The simulation results in Figure 4.3 represent predictions since the potentials were parameterized to bulk properties of Au rather than nanowire specific properties or dislocation properties. The agreement between discrete experimental measurements and modeling predictions is remarkable and supports the utility of semi-empirical atomistic calculations. Experimental strength measurements are currently not available at intermediate wire sizes, particularly the size range where the multishell wires are stable.

For the <110> rhombic nanowires, the simulations predict strength values commensurate with experimental observations (Figure 4.3). Detailed investigation of the simulation results reveals that tensile surface stresses from the {111} side surfaces inhibit nanowire yield. The {111} surfaces naturally contract relative to the nanowire core due to the existence of tensile surface stress. Without any externally applied force, the tensile surface stresses generate an "intrinsic" compressive stress in the wire core[31]. At equilibrium, the tensile forces on the surface balance the compressive forces in the interior of the wire. Although this intrinsic stress exists in all solid materials, its magnitude increases with decreasing dimensional scale and is significant only for nanometer scale materials. For example, the intrinsic compressive stress in a 7 nm <110> nanowire with {111} side surfaces is on the order of 1 GPa based on a {111} surface stress of 1.8 J/m^2. Intrinsic stresses on the order of GPa can alter the yield strength of a nanowire relative to ideal classical or atomistic theories. The surface stress induced intrinsic stress in macroscopic solids, averaged over the large core cross section, is on the order of Pa, a negligible value.

During tensile loading, the stress in the interior of the wire changes from a compressive to a tensile state, and ultimately the wire yields under tension. Thus, the applied tensile force must overcome the surface-stress-induced intrinsic compressive stress in the wire core. The effect of surface stress constraint is not considered in ideal theoretical strength predictions for bulk materials (Figure 4.3). For example, classical and atomistic ideal yield strengths for bulk Au are 1.48 GPa and 3.56 GPa, respectively (Figure 4.1). The classical and atomistic tensile strength values increase by 67% and 28%, respectively, with consideration of an opposing 1 GPa intrinsic compressive stress. Furthermore, the predicted increase in the strength of the <110> rhombic wires, with a decrease in size from 6 nm to nearly 1 nm (Figure 4.3), is caused by an increase in the intrinsic compressive stress, which scales with 1/d, where d is the lateral dimension of the wire. In fact, at very small wire sizes, a properly oriented wire can experience compressive yield under the exclusive influence of surface stresses[29]. Experimental measurements of asymmetric strength in nanowires (lower strength in compression versus tension)[8] partially support the existence of intrinsic compressive stresses in nanowires, although the nucleation of unidirectional partial dislocation systems can also contribute to strength asymmetry. The intrinsic stress effect is only critical at very small nanowire sizes (less than 10 nm in diameter) and other size dependent mechanisms, which alter resistance to plastic flow, are clearly operating as size scale spans nanometers to microns (Figure 4.1).

A somewhat auspicious agreement is discovered between the atomistic predictions of *nanowire* strength and the ideal strength calculated using *bulk* atomistic simulations. In particular, Figure 4.3 shows quantitative agreement between the ideal strength from atomistics and the predicted strength of nanowires in the size range of 1-2 nm. In reality, the predicted strength of the nanowires, relative to ideal theoretical predictions (Figure 4.3), is a counterbalance of strength enhancement from intrinsic surface stress constraint and strength reduction due to the availability of free surfaces and corners for defect nucleation. The free surfaces and corners act as favorable sites for heterogeneous defect nucleation, resulting in a lower predicted strength value relative to homogeneous slip assumed in ideal strength predictions for bulk materials. On the other hand, as wire size increases, the surface-stress-induced intrinsic compressive stress diminishes and the predicted nanowire strength gradually falls below the ideal theoretical value. Additional surface features, such as ledges and steps, can further lower the barrier to dislocation nucleation and decrease the strength of nanowires.

A distinct transition in yield strength is discovered traversing the 1 nm size scale. The strength values for wires smaller than 1 nm are under-predicted by ideal strength theories based on the fcc structure. The drastic increase in yield strength occurs concurrently with a change in wire structure from a fcc rhombic <110> wire to a non-fcc multishell wire. The embedded atom model predicts this structural change in line with experimental observations[25-28]. The systematic strength increases in the multishell nanowires heads towards the strength of the single atoms chain (Figure 4.3). The 1.0 nm multishell wire contains two shells surrounding a single atom chain, while the 0.7 nm multishell wire contains one shell surrounding a single atom chain (Figure 4.2b). Smaller *multishell* structures are not possible because removing the final outer shell results in a single atom chain (Figure 4.2b). The strength level of single atom chains has been previously examined using *ab initio* simulations, which account explicitly for electronic degrees of freedom in calulations[10]. These first principal calculations have reasonable agreement with experimental measurements for single atom chains (Figure 4.3). At present, *ab initio* simulations are impractical for the larger wires in the present study due to computational limitations.

To explain the dependence of strength on wire size, we examine the yield mechanisms in representative nanowires. Figure 4.4 provides a series of images during the initial yield of the <110> rhombic wire in Figure 4.2a. Only a portion of the wire is shown and the wire is viewed edge-on (Figure 4.4a). Blue atoms correspond to atoms that have not been sheared, while colored atoms correspond to slipped atoms. Yielding in the rhombic <110> nanowire is controlled by the nucleation and sudden propagation of partial dislocations from near the wire edge. Figure 4.4b shows the wire at the onset of yield where a small group of edge atoms (colored in green) begin to slip. Almost instantaneously, two leading {111}<112> partial dislocations nucleate and propagate across the wire cross-section on {111} planes leaving stacking faults (Figure 4.4c). Following the onset of yield, a few adjacent planes undergo slip (Figure 4.4d). During the yielding, the sample experiences a reduction in cross-sectional area (necking), evident in Figures 4.4(c-f). Ultimately, stacking faults remain on only one of the initial slip planes (Figure 4.4f). Rhombic <110> nanowires with other sizes studied here yield via the same mechanism presented in Figure 4.4. The yield *mechanisms* in the <110> rhombic nanowires are fundamentally the same as observed plastic flow *mechanisms* in bulk fcc Au. However, the nanowire yield is controlled by the nucleation and propagation of a few partial dislocations, and the wires yield under the combined influence of applied forces and surface-stress-induced intrinsic stresses. The nucleation of dislocations in a perfect <110> nanowire occurs near the edge of the wire, an unavoidable geometrical feature attributed to the faceted nature of small single crystals.

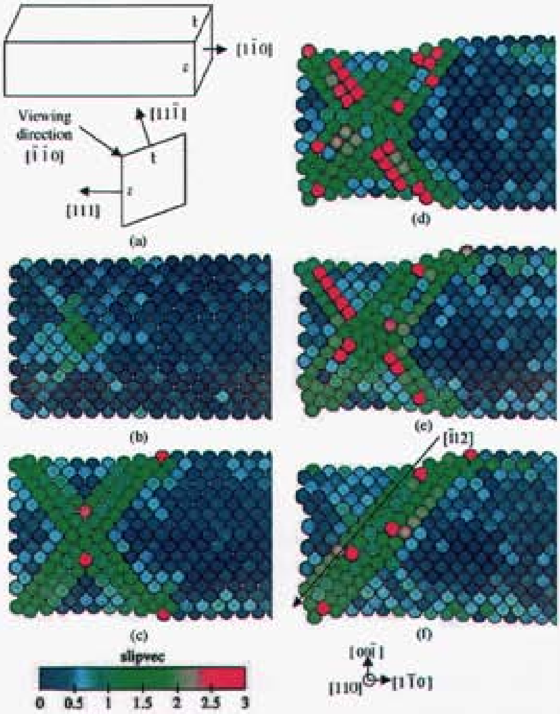

Figure 4.4. Yield mechanism in the 2.2 nm <110> rhombic nanowire. (a) indicates the viewing direction for images in (b-f). Atoms are colored according to their slip vector[35]*, which is equal to 1.67 for partial <112> dislocations and 2.89 for perfect <110> dislocations. Yield occurs by the sudden nucleation and propagation of leading <112> partial dislocations on {111} planes.*

The yield mechanisms in the multishell nanowires are illustrated in Figure 4.5 for the smaller multishell nanowire (one shell and single atom core). Yielding in the multishell nanowire is controlled by local tensile bond fracture at the wire surface, followed by relative shear of surrounding atoms. Figure 4a shows the atomic positions in the multishell nanowire just prior to yielding. Yield nucleates at an atomic triple junction on the wire periphery near the center of the wire (Figure 4.5b). The local tensile fracture of the atomic bond between the three surface atoms results in stress relief along the fractured chain, a reduction in cross sectional area, and the formation of a point-like defect at the wire surface (Figures 4.5(b-e)). Subsequent yield occurs through the shearing of adjacent atoms leading to further wire necking (Figures 4.5(f-j)). Larger multishell nanowires (two shells and single atom core) yield by a similar two-staged mechanism depicted in Figure 4.5. The yield mechanism in the multishell nanowire represents a noteworthy departure from dislocation plasticity observed in bulk fcc solids and larger fcc nanowires. In fact, the yield mechanism in the multishell wires is an intriguing compromise between perfect atomic separation forced in single atom chains and dislocation plasticity in larger fcc nanowires. The unique yield mechanism in the multishell nanowires explains the transitional strength values predicted in this nanowire relative to larger and smaller nanowires (Figure 4.3).

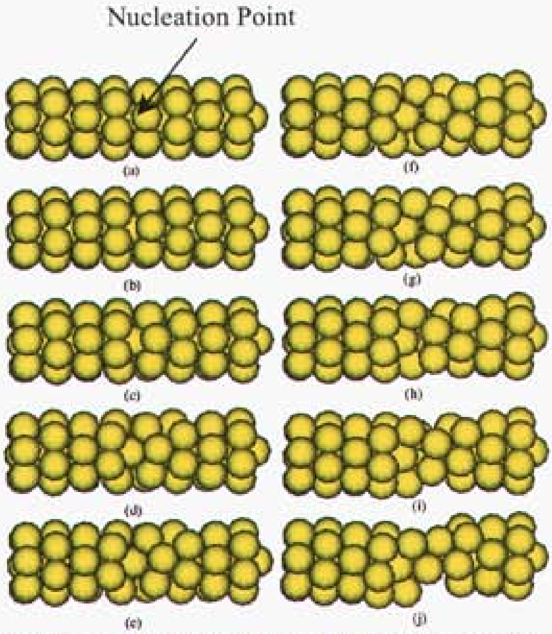

Figure 4.5. Yield mechanism in the 0.7 nm multishell nanowire. Yield occurs by the nucleation of local tensile fracture in an atomic triple junction on the wire periphery (see center of images a-e). Subsequent shearing of adjacent atoms propagates yield across the cross section of the nanowire (f-j).

In closing, we mention that our simulations have only considered perfect single crystal nanowires in a limited size range. It is still necessary to examine nanowires larger than 10 nm as significant size scale effects are observed as wire size traverses the 10 nm to 1000 nm range (Figure 4.1). Additionally, the effect of pre-existing defects and impurities on nanowire strength merits study. Owing to their small overall volume, nanowires are extremely sensitive to defects such as stacking faults[36], pre-existing dislocations, surface ledges, and impurities. For example, Au nanowires are often chemically grown in solution and may contain impurity atoms in their core or on their surface. Knowing the significant influence impurity atoms have on bulk materials, it seems absolutely critical to understand the effect of impurities on the strength of nanowires. It is possible that the aforementioned structural features may change the nanowire yield response significantly from what is predicted herein.

4.4 Conclusions

We have presented a fundamental understanding of the strength of nanometer scale Au wires. Nanowire strength is considerably higher than bulk materials, depends on wire size, and cannot be predicted by ideal bulk strength theories. Atomistic simulations reveal that size-dependent nanowire strengths for wires under 10 nm in diameter, are influenced by wire structure, surface stress, and defect formation mechanism. Free surfaces are critical to the mechanical behavior of nanowires because they lead to intrinsic compressive stresses and dislocation resistant wire structures, both of which drive increases in tensile yield strength consistent with experimental measurements. Free surfaces also serve as favorable nucleation sites for defects in perfect nanowires, driving analogous decreases in tensile yield strength. The quantitative and qualitative agreement between experimental measurements and atomistic predictions highlights the utility of semi-empirical atomistic tools for examining the mechanical behavior of nanometer scale materials.

4.5 References

[1] A. Kelly, Strong Solids, 2nd Edition, Clarendon Press, Oxford, (1973).

[2] ASTM F72-95, Standard Specification for Gold Wire for Semiconductor Lead Bonding, 1-13, ASTM International, West Conshohocken, PA (2001).

[3] H. D. Espinosa and B. C. Prorok, Size Effects on the Mechanical Behavior of Gold Thin Films, J. Mater. Sci. 38, 4125-4128 (2003).

[4] R. D. Emery and G. L. Povirk, Tensile Behavior of Free-Standing Gold Films. Part II. Fine-Grained Films, Acta Mater. 51, 2079-2087 (2003).

[5] W. M. Mook, J. M. Jungk, M. J. Cordill, N. R. Moody, Y. Sun, Y. Xia, and W. W. Gerberich, Geometry and Surface State Effects on the Mechanical Response of Au Nanostructures, Z. Metallkd. 95, 416-424 (2004).

[6] N. Agrait, G. Rubio, and S. Vieira, Plastic Deformation of Nanometer-Scale Gold Connective Necks, Phys. Rev. Lett. 74, 3995-3998 (1995).

[7] A. Stalder and U. Durig, Study of Plastic Flow in Ultrasmall Au Contacts, J. Vac. Sci. Tech. 14, 1259-1263 (1996).

[8] P. E. Marszalek, W. J. Greenleaf, H. Li, A. F. Oberhauser, and J. M. Fernandez, Atomic Force Microscopy Captures Quantized Plastic Deformation in Gold Nanowires, Proc. Nat. Acad. Sci, 97, 6282-6286 (2000).

[9] G. Rubio, N. Agrait, and S. Vieira, Atomic-Sized Metallic Contacts: Mechanical Properties and Electronic Transport, Phys. Rev. Lett 76, 2302-2305 (1996).

[10] G. Rubio-Bollinger, S. R. Bahn, N. Agrait, K. W. Jacobsen, and S. Vieira, Mechanical Properties and Formation Mechanisms of a Wire of Single Gold Atoms, Phys. Rev. Lett. 87, 026101-1 – 026101-4 (2001).

[11] In the atomic regime, the definition of cross sectional area is nontrivial and can be controversial. In Figure 4.1, we assumed the cross-sectional area of the single atom chain to be equal to the projected area of one spherical atom defined by the bulk lattice constants. Experimental measurements[12] and theoretical predictions[13] have shown that the atomic spacing in a single atom chain differs from bulk values in the close packed crystallographic directions. However, reasonable deviations in the assumed load bearing area have no impact on the relative ordering of the strengths in Figure 4.1. However, we must emphasize, when determining other mechanical

properties, such as the elastic modulus, small changes in the assumed cross-sectional area have significant relative impact since modulus values do not span orders of magnitude with size scale[14].

[12] V. Rodrigues and D. Ugarte, Real-time Imaging of Atomistic Process in One-Atom Thick Metal Junctions, Phys. Rev. B 63, 073405-1 – 073405-4 (2001).

[13] E. Z. da Silva, A. J. R. da Silva, and A. Fazzio, How do Gold Nanowires Break?, Phys. Rev. Lett. 87, 256102-1 – 256102-4 (2001).

[14] J. Diao, K. Gall and M. L. Dunn, Atomistic Simulation of the Structure and Elastic Properties of Metal Nanowires, J. Mech. Phys. Solids 52(9), 1935-1962 (2004).

[15] The classical prediction of the ideal theoretical yield strength is based on the shear strength (τ_{max} = 0.74 GPa) of two sliding atomic planes aligned at 45 degrees with respect to the loading axis[1]. The theoretical yield strength, $\sigma_{max} = 2.0\ \tau_{max}$ = 1.48 GPa represents a "lower limit" since single crystals show anisotropy; the orientation of the preferred slip planes may not be 45 degrees (uniaxial Schmid factor m = 0.5, where $\tau_{max} = m\ \sigma_{max}$). The Schmid factor describes the angle between the slip plane and the loading axis, where m = 0 is 90° and m = 0.5 is 45°. The maximum uniaxial Schmid factor for an fcc <110> wire deformed under tension, slipping on {111}<112> systems, is 0.47. This value is only slightly smaller than the maximum value of m = 0.5 for a plane aligned at 45 degrees. The atomistic prediction of ideal theoretical yield strength ($\sigma_{max} = 2.0\ \tau_{max}$ = 3.56 GPa) is based on bulk simulations (periodic in all directions) of the coordinated shearing of two Au {111} planes in <112> directions. Identical EAM Au potentials were used for nanowire simulations and the ideal bulk atomistic yield calculations.

[16] U. Landman, W. D. Luedtke, N. A. Burnham, R. J. Colton, Atomistic Mechanisms and Dynamics of Adhesion, Nanoindentation, and Fracture, Science 248, 454-461 (1990).

[17] M. Brandbyge, J. Schiotz, M. R. Sorensen, P. Stoltze, K. W. Jacobsen, J. K. Norskov, L. Olesen, E. Laegsgaard, I. Stensgaard, and F, Besebbacher, Quantized Conductance in Atom-Sized Wires Between Two Metals, Phys. Rev. B 52, 8499-8514 (1995).

[18] M. Mehrez, S. Ciraci, C. Y. Fong, and S. Erkoc, An Atomistic Study on the Stretching of Nanowires, J. Phys. Condens. Matter 9, 10843-10854.

[19] H. Ohnishi, Y. Kondo, and K. Takayanagi, Quantized Conductance Through Individual Rows of Suspended Gold Atoms, Nature 395, 780-783 (1998).

[20] A. I. Yanson, G. R. Bollinger, H. E. van der Brom, N. Agrait, and J. M. Ruitenbeek, Formation and Manipulation of a Metallic Wire of Single Gold Atoms, Nature 395, 783-785 (1998).

[21] V. Rodrigues, T. Fuhrer, and D. Ugarte, Signature of Atomic Structure in Quantum Conductance of Gold Nanowires, Phys. Rev. Let. 85, 4124-4127 (2000).

[22] G. M. Finbow, R. M. Lynden-Bell, and I. R. McDonald, Atomistic Simulation of the Stretching of Nanoscale Metal Wires, Mol. Phys. 92, 705-714 (1997).

[23] M. R. Sorensen, M. Brandbyge, and K. W. Jacobsen, Mechanical Deformation of Atomic-Scale metallic Contacts: Structure and Mechanisms, Phys. Rev. B 57, 3283-3294 (1998).

[24] A. Nakamura, M. Brandbyge, L. B. Hansen, and K. W. Jacobsen, Density Functional Simulations of a Breaking Nanowire, Phys. Rev. Let. 82, 1538-1541 (1999).

[25] Y. Kondo and K. Takayanagi, Gold nanobridge stabilized by surface structure. Phys. Rev. Lett. 79, 3455–3458 (1997).

[26] Y. Kondo and K. Takayanagi, Synthesis and characterization of helical multi–shell gold nanowires. Science 289, 606–608 (2000).

[27] O. Gülseren, F. Ercolessi, and E. Tosatti, Noncrystalline Structures of Ultrathin Unsupported Nanowires. Phys. Rev. Lett. 80 (17), 3775 (1998).

[28] B. Wang, S. Yin, G. Wang, A. Buldum, and J. Zhao, Novel Structures and Properties of Gold Nanowires, Phys. Rev. Let. 86, 2046-2049 (2001).

[29] J. Diao, K. Gall and M. L. Dunn, Surface Stress Driven Reorientation of Gold Nanowires, *Physical Review B* 70, 075413 *(2004).*

[30] M. S. Daw, and M. I. Baskes. Embedded-atom method: derivation and application to impurities, surfaces, and other defects in metals. Phys. Rev. B 29 (12), 6443 (1984).

[31] J. Diao, K. Gall and M. L. Dunn. Surface-Stress-Induced Phase Transformation in Metal Nanowires. *Nature Materials*, 2 (10), 656 (2003).

[32] T. Egami, K. Maeda, V. Vitek. Structural defects in amorphous solids: a computer simulation study. Philosophical Magazine A 41, 883 (1980).

[33] K. S. Cheung and S. Yip Atomic-level stress in an inhomogeneous system. J. Appl. Phys. 70 (10), 5688–5690 (1991).

[34] M. Zhou. A new look at the atomic level virial stress: on continuum-molecular system equivalence. Proc. R. Soc. Lond. A, 459, 2347 (2003).

[35] J. A. Zimmerman, C. L. Kelchner, P. A. Klein, J. C. Hamilton, and S. M. Foiles, Surface step effects on nanoindentation. Phys. Rev. Lett 87 (16), 165507 (2001).

[36] J. Diao, K. Gall, and M. L. Dunn (2004) Yield Strength Asymmetry in Metal Nanowires. *Nanoletters*. vol. 4, no. 10, pp. 1863-1867.

5 Atomistic Simulations of the Yielding of Gold Nanowires

We performed atomistic simulations to study the effect of free surfaces on the yielding of gold nanowires. Tensile surface stresses on the surfaces of the nanowires cause them to contract along the length with respect to the bulk fcc lattice and induce compressive stress in the interior. When the cross-sectional area of a <100> nanowire is less than 2.45 nm x 2.45 nm, the wire yields under its surface stresses. Under external forces and surface stresses, nanowires yield via the nucleation and propagation of the {111}<112> partial dislocations. The magnitudes of the tensile and compressive yield stress of <100> nanowires increase and decrease, respectively, with a decrease of the wire width. The magnitude of the tensile yield stress is much larger than that of the compressive yield stress for small <100> nanowires, while for small <111> nanowires, tensile and compressive yield stresses have similar magnitudes. The critical resolved shear stress (RSS) by external forces depends on wire width, orientation and loading condition (tension vs. compression). However, the critical RSS in the interior of the nanowires, which is exerted by both the external force and the surface-stress-induced compressive stress, does not change significantly with wire width for same orientation and same loading condition, and can thus serve as a "local" criterion. This local criterion is invoked to explain the observed size dependence of yield behavior and tensile/compressive yield stress asymmetry, considering surface stress effects and different slip systems active in tensile and compressive yielding.

5.1 Introduction

Metal nanowires are of technological importance due to their potential applications in miniaturized electrical, optical, thermal and mechanical systems. Nanowires have a very large surface-area/volume ratio as compared to bulk materials and their structures and properties can be quite different than those of bulk materials [1-17]. The use of nanowires in emerging technologies demands a thorough understanding of their structures and properties.

Mass production of nanowires has been made possible by electrochemical methods using physical templates [18] or by self-assembly [19]. At the same time, advances in the development of the experimental tools have made it possible to evaluate nanometer scale properties and materials. For example, researchers [20-26] have studied the formation of gold nanowires through the necking of atomic point contacts. Marszalek *et al.* [27] measured the quantized plastic deformation in gold nanowires under tension and compression caused by individual slip events using atomic force microscopy. They also identified an asymmetric yield behavior of gold nanowires, i.e., the magnitude of the tensile yield stress is much larger than that of the compressive yield stress in very small nanowires, but did not provide a mechanistic explanation for this yield stress asymmetry.

Atomistic simulations have been used to study the inelastic deformation mechanisms in nanometer scale materials. Horstemeyer [28] studied the length and time scale effects on the plastic flow of fcc metals under a simple shear loading. Liang and Zhou [29] studied the size and strain rate effects in tensile deformation of Copper nanowires. Sorensen [30] demonstrated that for nanometer-scale materials, slip can take place by (at least) two distinct mechanisms: the glide of a dislocation and the homogeneous shear of one plane of atoms over an adjacent plane. These two slip mechanisms are also observed in the atomistic simulation of Kang and Hwang [31]. Liang *et al.* [32] revealed an increase in the tensile yield stress of Copper [100] nanowires with a decreasing cross-sectional area. They qualitatively attributed this size dependence to the initial compressive stress state in the interior of nanowires.

Although various researchers have uncovered interesting phenomena regarding the yield of nanometer scale materials, a comprehensive understanding of the mechanisms leading to the observed behaviors is lacking, especially the quantitative understanding of the surface stress effect. Free surfaces play two important roles in the yielding of nanowires: (i) free surfaces act as preferential nucleation sites for defects; (ii) and surface stresses exist on the surfaces of nanowires. The latter effect of surface stress on the yielding of nanowires can be appreciated by examining the magnitude of the *intrinsic* compressive stress in the interior of the nanowires induced by the surface stress (Figure 5.1).

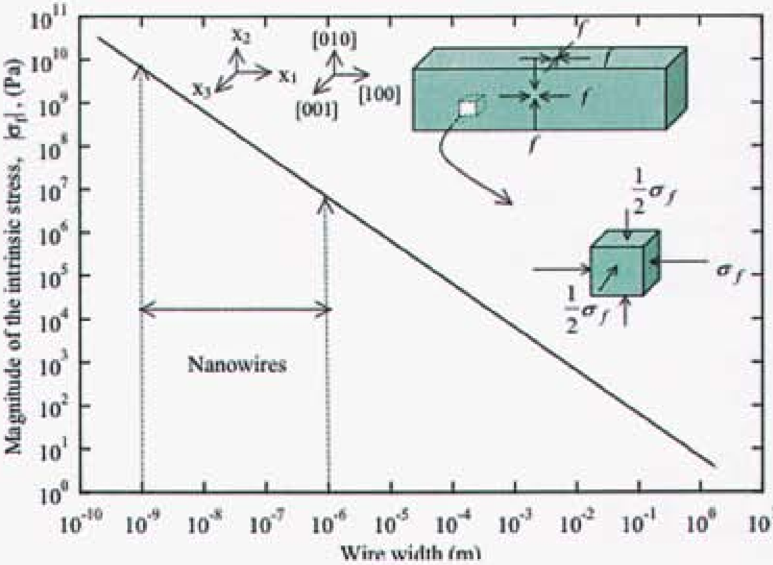

Figure 5.1. Magnitude of the surface-stress-induced intrinsic compressive stress, $|\sigma_f|$, *in fcc gold [100] wires as a function of the wire width.*

Tensile surface stress on metal surfaces induces compressive stress in the interior, and at equilibrium the tensile surface stress and the induced intrinsic compressive stress balance each other. For a [100] wire, with [010] and [001] side surfaces and a square cross-section, the induced stress can be given by continuum estimate to be:

$$\sigma_{0,\mathrm{int}} = \begin{pmatrix} \sigma_f & 0 & 0 \\ 0 & \frac{1}{2}\sigma_f & 0 \\ 0 & 0 & \frac{1}{2}\sigma_f \end{pmatrix} \tag{5.1}$$

with

$$\sigma_f = -4fl/A = -4f/l \tag{5.2}$$

where f is the surface stress, l is the width of the wire, and $A = l^2$ is the cross-sectional area. Figure 5.1 was generated using a value of $f = 1.57\ \ J/m^2$ (Table 5.1), which is the surface stress in an fcc gold {100} surface calculated using an Embedded Atom Method (EAM) potential [33].

Table 5.1. Surface stresses on gold surfaces from the EAM potential (see [15] for details of the calculation), density functional theory (DFT) calculation [41,42], and experiment [43].

Surface (i)	Directions (j)	f_{ij} EAM	f_{ij} DFT	f Experiment
$\{100\}$	Isotropic	1.57	4.57	1.175
$\{111\}$	Isotropic	1.76	2.77	
$\{1\bar{1}0\}$	$\langle 111\rangle$	1.32	—	
	$\langle\bar{1}\bar{1}2\rangle$	1.11	—	
	Shear	-0.31	—	
$\{011\}$	$\langle 100\rangle$	0.89	—	
	$\langle 0\bar{1}1\rangle$	1.54	—	
	Shear	0	—	
$\{\bar{1}\bar{1}2\}$	$\langle 111\rangle$	1.12	—	
	$\langle 1\bar{1}0\rangle$	1.37	—	
	Shear	0	—	

Regardless of the method used to calculate or measure surface stress (Table 5.1), the magnitude of the intrinsic stress, $|\sigma_f|$, in wires of nanometer size is significant, on the order of MPa to GPa, and can alter or drive numerous stress-induced phenomena, such as plasticity.

The objective of this work is to use atomistic simulations to quantitatively study the effect of free surfaces on the yielding of metal nanowires. We will mainly focus on [100] nanowires with a square cross-section because of the high symmetry they possess, which makes them amenable for quantitative study. The main results of surface stress effects apply to nanowires of other orientations and of other cross-sectional shapes. Specifically, we examine the role of the free surfaces in the nucleation of defects in nanowires, study the dependence of the yield stress and yield strain on nanowire size, orientation, and loading conditions (tension vs. compression), and attempt to explain the yielding in terms of the resolved shear stress (RSS) in the observed slip direction on the observed slip plane, which is exerted by both the surface-stress-induced compressive stress and externally applied force. Even though we perform seemingly simple uniaxial loading, the yielding of nanowires is actually a complicated three-dimensional problem due to the surface stresses.

5.2 Simulation Methods

We perform atomistic simulations with the embedded atom method (EAM) potential for fcc gold [33], in which the total energy of a system of atoms is given by

$$U = \sum_i \left(F_i(\bar{\rho}_i) + \frac{1}{2} \sum_{j(\neq i)} \phi_{ij}(r_{ij}) \right) \tag{5.3}$$

where ϕ_{ij} is the pair interaction between atoms i and j whose separation is given by r_{ij}, F_i is the embedding function, which is the energy required to embed an atom of type i into the background electron density $\bar{\rho}_i$ at site i, $\bar{\rho}_i$ is given by a linear supposition of spherically averaged atomic electron densities. The parameters in the EAM potential are fit to the sublimation energy, equilibrium lattice constant, elastic constants, and vacancy formation energy [33].

The slip vector defined by Zimmerman *et al.* [34] is used to quantify and visualize the plastic deformation in nanowires:

$$s^{\alpha} = -\frac{1}{n_s} \sum_{\beta \neq \alpha}^{n} (\mathrm{x}^{\alpha\beta} - \mathrm{X}^{\alpha\beta}) \tag{5.4}$$

where n is the number of the nearest neighbors of atom α, n_s is the number of slipped neighbors, and $\mathrm{x}^{\alpha\beta}$ and $\mathrm{X}^{\alpha\beta}$ are the position vector difference of atoms α and β in the current and reference positions. The slip vector magnitude is 1.67Å for a {111} <112> partial slip and 2.89Å for a perfect {111}<110> slip in gold.

The virial stress for a system of atoms is defined [35-37] as

$$\Pi^{\alpha\beta} = \frac{1}{\Omega}\{-\sum_i m_i v_i^\alpha v_i^\beta + \frac{1}{2}\sum_i \sum_{j\neq i} F_{ij}^\alpha r_{ij}^\beta\}, \tag{5.5}$$

where Ω is the volume of the system, $m_i$and v_i are the mass and velocity of particle i, F_{ij} is the force between atoms i and j, and the indices α and β denote the Cartesian components. The first summation term on the right side of eq. (5.5) is due to the thermal vibration and is zero in static simulations. The second summation term in the right side of eq. (5.5) is due to the inter-atomic force and can be identified with the Cauchy stress in the average sense [36,37]. Since the temperature in our simulations is very low (2 K), the contribution from the first term is negligible and the virial stress is a reasonable measure of the average stress state in the nanowires. Eq. (5.5) can be decomposed into

$$\Pi^{\alpha\beta} = \frac{1}{\Omega}\sum_i \varpi_i \pi_i^{\alpha\beta}, \tag{5.6}$$

with

$$\pi_i^{\alpha\beta} = \frac{1}{\varpi_i}\{-m_i v_i^\alpha v_i^\beta + \frac{1}{2}\sum_{j\neq i} F_{ij}^\alpha r_{ij}^\beta\} \tag{5.7}$$

and $\sum \varpi_i = \Omega$. Eq. (5.7) can be used as a definition of an atomic level stress associated with atom i, with ϖ_i taken as the effective volume of the atom i.

Throughout this paper, four stress measures are employed:

- (i) The stress averaged over the whole system (virial stress, $\mathbf{\Pi}$) as shown in eq. (5.5), which is equivalent to the Cauchy stress. Because we performed uniaxial loading on the nanowires, only $\Pi^{11}$is non-zero and is equal to the external force divided by the cross-sectional area. We will simply denote Π^{11} as $\mathbf{\Pi}$ since all other components are zero.
- (ii) The atomic level stress defined for an individual atom (eq. (5.7)), denoted as $\boldsymbol{\pi}$.
- (iii) The average of the atomic level stress over a subsystem of atoms and denoted as $\hat{\boldsymbol{\pi}}$. Due to the heterogeneous nature of the nanowires, in addition to the stress components, $\pi^{11}$and $\hat{\pi}^{11}$, other components of the stress $\boldsymbol{\pi}$ and $\hat{\boldsymbol{\pi}}$ can be non-zero even for uniaxial loading.
- (iv) The stress used in continuum modeling, denoted as $\boldsymbol{\sigma}$.

To calculate the resolved shear stress (RSS) in a slip direction on a slip plane for a general stress state, we use the Schmidt factor tensor defined as:

$$\alpha^{ij} = \frac{1}{2}(n^i t^j + n^j t^i) \tag{5.8}$$

where ***n*** is the slip plane normal (unit vector) and ***t*** is the slip direction (unit vector) on the slip plane. For uniaxial loading, the RSS corresponding to the stress measures (i), (ii) and (iii) defined above, can be calculated using the Schmidt factor tensor as:

$$T = \sum_i \sum_j \Pi^{ij} \alpha^{ij} = \Pi^{11} \alpha^{11} = m\Pi \tag{5.9}$$

$$\tau = \sum_i \sum_j \pi^{ij} \alpha^{ij} \tag{5.10}$$

$$\hat{\tau} = \sum_i \sum_j \hat{\pi}^{ij} \alpha^{ij} \tag{5.11}$$

In eq. (5.9) we have only one term in the summation since virial stress components other than Π^{11} are zero for uniaxial loading, and m is the uniaxial Schmidt factor. Uniaxial tensile and compressive Schmidt factors, m, for the most favorable {111}<112> partial slip systems in the [100] and [111] nanowires with atoms in bulk lattice are shown in Table 5.2.

Table 5.2. Uniaxial tensile and compressive Schmidt factors, m, for the most favorable {111}<112> partial slip systems in the [100] and [111] nanowires with atoms in bulk fcc lattice.

Orientation	Compressive		Tensile	
	Lead	Trail	Lead	Trail
{100}	0.47 (4 systems)	0.24	0.24 (8 systems)	0.47
{111}	0.16 (6 systems)	0.31	0.31 (3 systems)	0.16

Due to the large yield strain of nanowires, the Schmidt factor tensor at the onset of yield is different than that in the bulk lattice; this is taken into account by using the slip plane normal and slip direction at the onset of yield in calculating the RSS.

Gold nanowires oriented in [100] direction with a square cross-section and (010) and (001) side surfaces were created with atoms in bulk fcc lattice. Periodic boundary conditions (PBCs) are used in the length direction and the periodic length is approximately three times the width of nanowires. For this aspect ratio, the imposed PBCs do not affect the yield behavior of the nanowires. Because of the tensile surface stresses on the {100} side surfaces, the nanowires created in this way are not in equilibrium and contract upon relaxation; we call the resulting strain in the length direction, with respect to the unrelaxed configurations, the equilibrium strain, ε^*. Dynamic relaxations were performed at low temperature (2 K) using molecular dynamics.

Starting from the equilibrium configuration of the nanowires, we next performed uniaxial tensile and compressive loading on the relaxed nanowires until yield. We displaced all the atoms in accordance with a prescribed uniform strain in the length direction, fixed the periodic length in the length direction, and then dynamically relaxed the nanowires at 2 K for 200 *ps* with 0.004 *ps* per time step to obtain the equilibrium configurations of the nanowires at the prescribed strain. The equilibrium state of the nanowires was determined by allowing the virial stress, $\mathbf{\Pi}$, to saturate as a function of time. The nanowires typically reach equilibrium after 100 *ps* and the stress averaged over the second 100 *ps* is used as the stress of the nanowires. For each nanowire, we repeated the loading process until yield with a varying strain increment at each loading step. A large strain increment is used in the first several steps, then the step size is gradually reduced, and the step size is reduced to 0.05% just before yield.

To expedite the simulations, we explored the possibility of using static simulation (conjugate gradient method) as an alternative in the first a few steps well before yielding. We compared the exclusive dynamic uniaxial tensile loading with a mixed static/dynamic uniaxial tensile loading on the 2.65*nm* x 2.65*nm* nanowire. In the mixed uniaxial tensile loading, the nanowire is loaded statically in the first five steps and dynamically in the remaining steps. The two methods show little difference in both yield stress and yield strain, so this mixed approach was used for all simulations. We use dynamic relaxation at low temperature instead of static relaxation in the last a few steps to introduce small thermal noise to facilitate the yielding of the nanowires, and also to observe the detailed yielding process.

We also performed simulations on a [111] nanowire with a nearly square cross-section (4.08 nm x 3.98 nm) with ($\bar{1}\,\bar{1}2$) and ($1\bar{1}0$) side surfaces, and a [100] nanowire with a size of 2.74 nm x 2.74nm and (011) and ($0\bar{1}1$) side surfaces.

5.3 Results

5.3.1 Relaxation of the nanowires

Figure 5.2 shows the strain in the length direction during the dynamic relaxation process, with respect to the initial unrelaxed configurations as a function of relaxation time for two nanowire sizes. The 2.65nm x 2.65nm nanowire shows only the development of elastic strain as a function of time and the saturated strain is the equilibrium strain, ε^*. Figure 5.3 shows the equilibrium strain, ε^*, of the [100] nanowires as a function of the width of nanowires. The magnitude of the equilibrium strain, ε^*, increases with a decrease of the nanowire width. However, as the width of an fcc [100] nanowire decreases below $2.45nm$, yield occurs upon relaxation (fig. 5.2). The $2.24nm \times 2.24nm$ nanowire (fig. 5.2) contracts elastically initially, and when the strain reaches approximately 7.3%, the wire yields. Elastic contraction and yield occur repeatedly during further relaxation.

Figure 5.4 shows the slip planes of the $2.24nm \times 2.24nm$ nanowire in the first yield event (fig. 5.2). Two partial slips occur in the nanowire. Figure 5.5 shows the details of the nucleation and propagation of a partial dislocation on a slip plane shown in fig. 5.4.

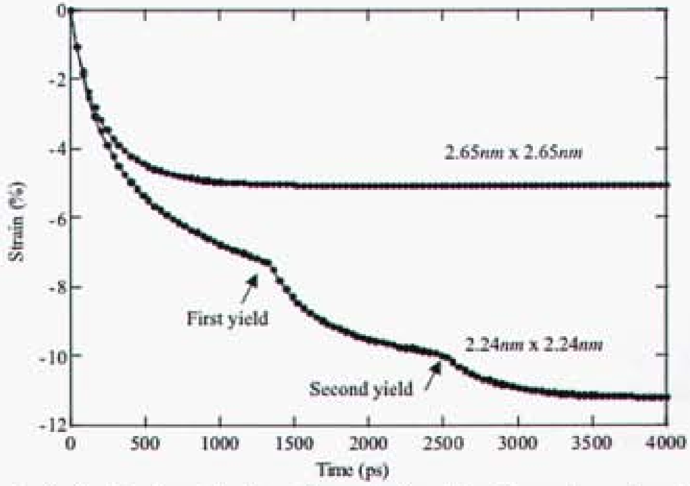

Figure 5.2. The strain in the length direction during the dynamic relaxation process, with respect to the initial unrelaxed configurations as a function of relaxation time for two nanowire sizes.

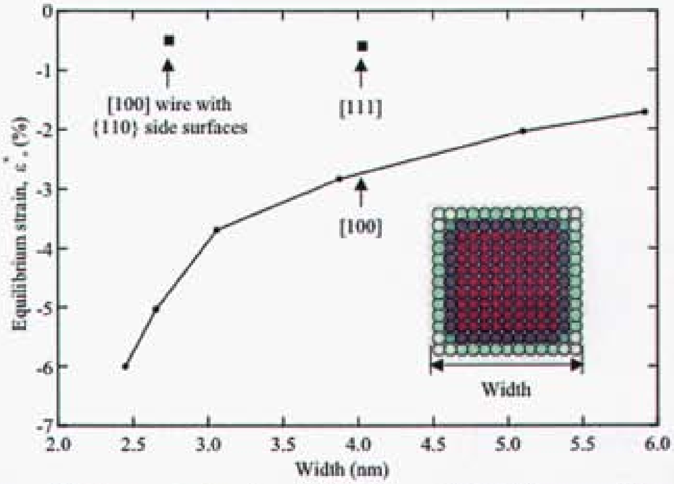

Figure 5.3. The equilibrium strain, ε^*, of the fcc gold [100] nanowires as a function of the nanowire width. The equilibrium strain of the [111] wire and the [100] wire with {110} side surfaces are also shown. Shown in the inset is the cross-section of a [100] nanowire.

The slip vector is $\frac{1}{6}[\bar{2}11]$ in the (111) plane and the partial dislocation nucleates from an edge and propagates along the $[01\bar{1}]$ direction into the nanowire, leaving a stacking fault behind.

The 2.74 nm x 2.74nm [100] nanowire with (011) and $(0\bar{1}1)$ side surfaces has an equilibrium strain of a much smaller magnitude (Fig. 5.3) due to the much smaller surface stress component along the length direction (Table 5.1). The 4.08 nm x 3.98 nm [111] nanowire also has a much smaller magnitude of equilibrium strain (Fig. 5.3) due to the larger modulus in the [111] direction and the smaller surface stress component along the length direction (Table 5.1). There is also a shear deformation in the [111] nanowire caused by the shear surface stress component on the $[1\bar{1}0]$ side surfaces (Table 5.1).

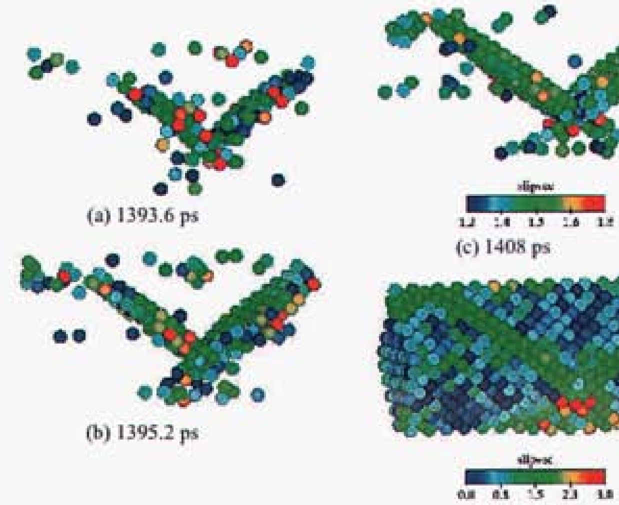

(a) 1393.6 ps

(c) 1408 ps

(b) 1395.2 ps

(d) 1408 ps

Figure 5.4. Slip planes in the first yielding event (fig. 5.2) of the 2.24nm x 2.24nm nanowire upon relaxation. Atoms are colored according to the slip vector magnitude defined in eq. (5.4) and only the atoms that have slip vector magnitude close to that of the {111}/ <112> partial slip are shown in (a,b,c), while in (d) all atoms are shown.

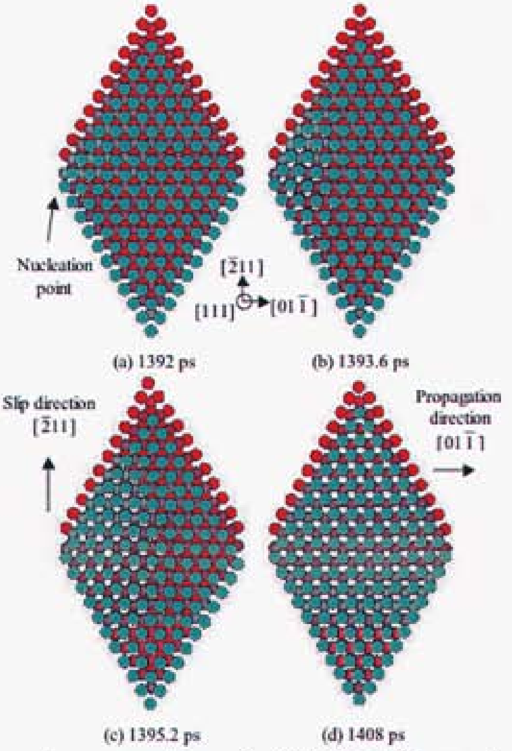

(a) 1392 ps (b) 1393.6 ps

(c) 1395.2 ps (d) 1408 ps

Figure 5.5. Nucleation and propagation of a $\{111\}<112>$ partial dislocation on a slip plane (fig.4) of the $2.24nm \times 2.24nm$ nanowire. Only three adjacent $<111>$ layers are shown and atoms in different layers are shown in different colors.

5.3.2 Tensile and compressive yielding

Figure 5.6 shows representative stress (Π)-strain curves for the [111] and [100] nanowires subject to uniaxial tensile and compressive loading. Both wires deform elastically until a critical point is reached, and the wire yields. This initial yield results in a significant drop in stress under the displacement controlled loading. The strains in Fig. 5.6 are calculated with respect to the relaxed configurations. Note the significant tensile-compressive yield stress asymmetry exhibited by the [100] nanowires.

Figure 5.7 shows the tensile and compressive yield strain as a function of the width of the [100] nanowires. The magnitude of the compressive yield strain decreases as the nanowire width decreases. Also shown is a measure of the compressive yield strain that is calculated with respect to (wrt) the unrelaxed nanowire length; it does not change significantly with the nanowire width. This implies that a smaller nanowire yields at a smaller compressive strain primarily because it has contracted more upon relaxation to equilibrium from its unrelaxed length driven by the surface stresses (fig. 5.3).

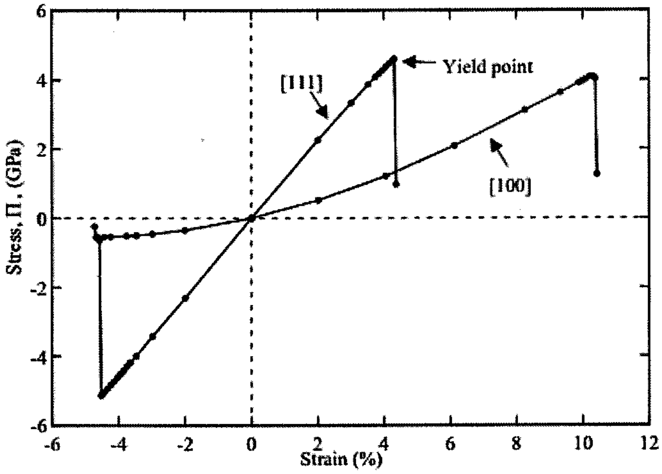

Figure 5.6. Representative stress (Π)-strain curves for [111] and [100] nanowires subject to uniaxial tensile and compressive loading. The nanowire size is approximately 4nm x 4nm.

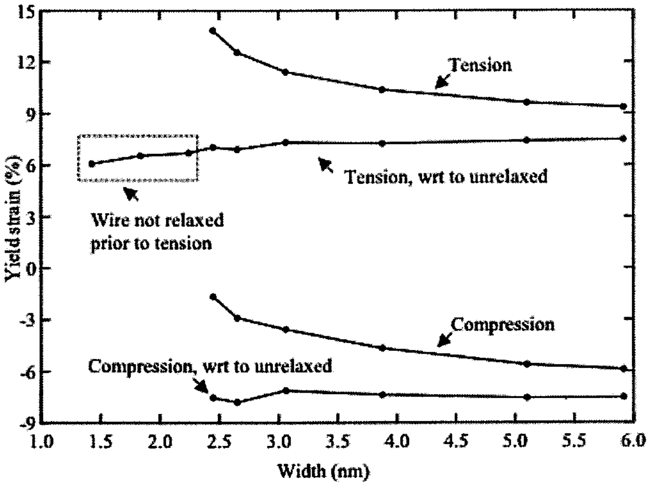

Figure 5.7. Uniaxial tensile and compressive yield strain as a function of the width of the [100] nanowires.

The tensile yield strain increases as the nanowire width decreases. However, the magnitude of the tensile yield strain calculated with respect to the unrelaxed nanowire length does not change significantly with the nanowire width. This implies that a smaller nanowire yields at a larger tensile strain primarily because it has contracted more upon relaxation to equilibrium from its unrelaxed length driven by surface stresses and this larger contraction has to be overcome in tensile yielding. As shown in Fig. 5.2, nanowires smaller than 2.45*nm* x 2.45*nm* yield under their own surface stresses; in order to generate their tensile stress-strain curve we did not relax them, but loaded them directly from their bulk atomic positions. Their tensile yield strains, with respect to the unrelaxed nanowire configurations, are also shown in fig. 5.7.

Figure 5.8 shows the uniaxial tensile and compressive yield stress, Π_y, as a function of the wire width. The tensile yield stress increases slightly with a decrease of the nanowire width, while the magnitude of the compressive yield stress decreases. Again, nanowires smaller than 2.45*nm* x 2.45*nm* yield under their own surface stresses and no external compressive force is necessary. Note that the tensile yield stress is significantly larger than the magnitude of the compressive yield stress for all wire sizes considered, consistent with the representative results in Fig. 5.6.

The yield mechanisms of both the compressive and tensile yielding are the same as in the surface-stress-induced yielding of the $2.24nm \times 2.24nm$ nanowire, i.e., through the nucleation and propagation of {111}<112> partial dislocations (Figs. 5.4, 5.5) from edges of the nanowires.

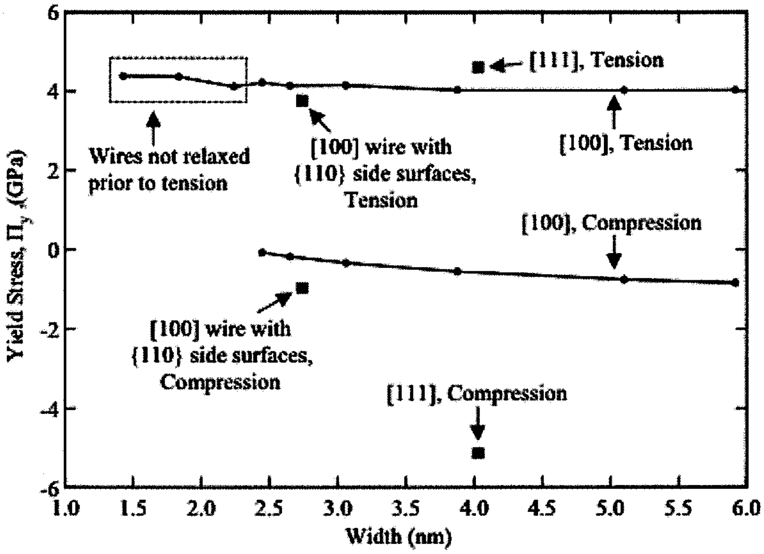

Figure 5.8. Tensile and compressive yield stress, Π_y*, as a function of the [100] nanowire width. Wires smaller than* $2.45nm \times 2.45nm$ *yield upon relaxation under their own surface stresses. These of the [111] nanowires and the [100] nanowires with {110} side surfaces are also shown.*

Figure 5.9 shows the tensile yielding of the 2.65*nm* x 2.65*nm* fcc gold [100] nanowire. We notice that both partial {111}<112> and perfect {111}<110> slip events occur in the tensile yielding of the nanowire. The perfect {111}<110> slip is formed by two sequential (leading and trailing) {111}<112> partial slips that occur on the same {111} planes. The passage of the trailing dislocation in tensile yielding and not in compressive yielding is consistent with the higher uniaxial Schmidt factor of the trailing dislocation under tension, but not under compression (Table 5.2).

The yield mechanism of the [111] nanowire is the same as in the [100] nanowires, i.e. via the nucleation and propagation of {111}<112> partial dislocations from the edges. In the tensile yielding of the [111] nanowires, only partial {111}<112> slip occurs. In the compressive yielding of the [111] nanowires, both {111}<112> and {111}<110> slips occur, and the {111}<110> slip is formed by two sequential (leading and trailing) {111}<112> slips on the same {111} planes. Again, the trailing slip occurs because the uniaxial Schmidt factor is larger in the trailing slip system (Table 5.2).

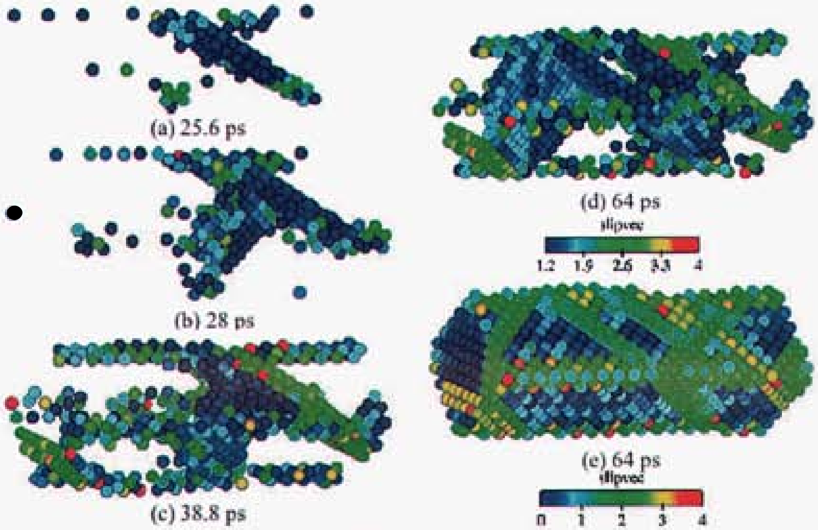

Figure 5.9. Tensile yielding of the 2.65nm x 2.65nm fcc [100] nanowire. Atoms are colored according to the slip vector defined in eq. (5.4) and only the atoms that have slipped are shown in (a,b,c,d), while all atoms are shown in (e).

5.4 Discussion

Table 5.2 summarizes the uniaxial Schmidt factors, m, for the most favorably oriented {111}<112> partial slip systems in the [100] and [111] nanowires under uniaxial tensile and compressive loading. Figure 5.10 shows the critical RSS, T_y, (just before yield) in the observed leading slip direction on the observed slip plane as a function of the nanowire width. The critical RSS, T_y, has a strong size, orientation, and loading direction (tension vs. compression) dependence, and thus cannot serve as a criterion for the yielding of the nanowires. In the pursuit of such a criterion, we next examine the stress state in the nanowire and RSS distribution on the slip planes during the relaxation and loading processes.

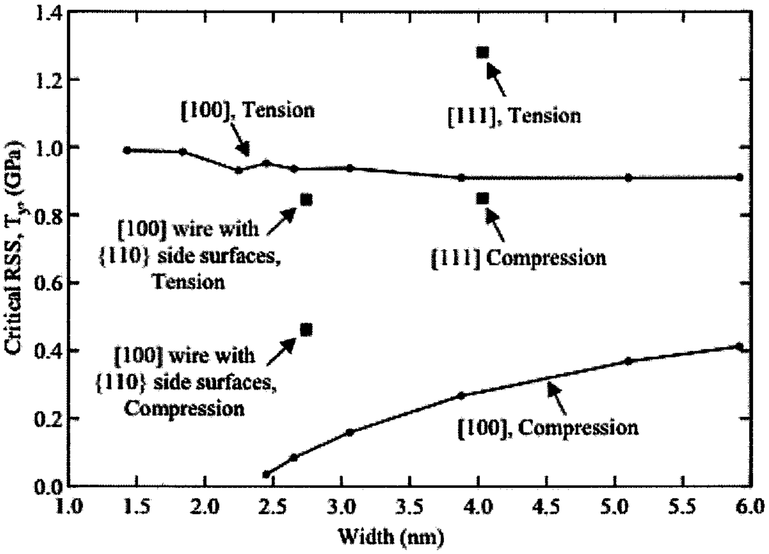

Figure 5.10. The critical RSS, T_y, in the leading slip direction, on the observed slip plane, as a function of the [100] nanowire width, along with those for the [111] nanowire and the [100] nanowire with {110} side surfaces.

5.4.1 Relaxation of the nanowires

Figure 5.11(a) shows the distribution of atomic level stress, π^{11}, on the cross-section of the unrelaxed (non-equilibrium) 2.65*nm* x 2.65*nm* [100] nanowire. The atoms in the outmost two surface layers are in a tensile stress state and the stress in the interior is negligible. The stress in the surface layers is the origin of the surface stress and is the driving force for the relaxation of the nanowires. Upon relaxation, the surface stress induces compressive stress in the interior, and at equilibrium the tensile surface stress and the induced intrinsic compressive stress balance each other. Figure 5.11(b) shows the distribution of the atomic level stress, π^{11}, on the cross-section of the relaxed (equilibrium) 2.65*nm* x 2.65*nm* nanowire. The tensile stress in the outmost two layer decreases upon relaxation, and interior region is in a compressive stress state. The stress, π^{11}, in the interior of the relaxed nanowire is quite uniform and has an average value of $\hat{\pi}^{11}$ = -2.23GPa in the interior (we hereafter define the interior of a nanowire to be all the region excluding the outmost two surface layers), well estimated by the continuum model of eq. (5.1) and (5.2) ($\sigma^{11}_{0,\text{int}} = \sigma_f = -4f/l = -2.32\text{GPa}$). From the continuum model (eqs. 5.1, 5.2), the magnitude of the induced compressive stress scales inversely proportional to the width of the nanowires. The smaller the nanowire, the lager the magnitude of the induced compressive stress, and the larger magnitude of the equilibrium strain, ε^* (fig. 5.3). In the same manner, tensile surface stress components in the x_2 and x_3 directions also induce compressive stress in the interior of the nanowires (fig. 5.1).

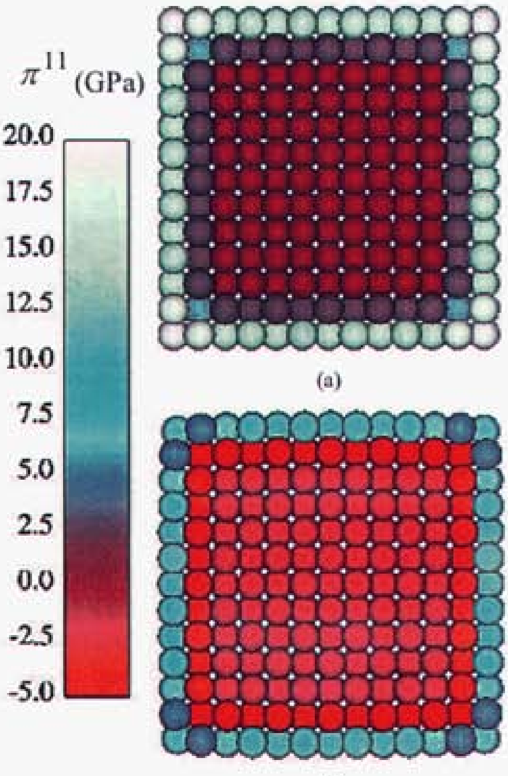

(a)

(b)

Figure 5.11. Distribution of the atomic level stress, π^{11}*, on the cross-section of the (a) unrelaxed and (b) relaxed 2.65nm x 2.65nm [100] nanowire. Only two layers of atoms are shown since the stacking sequence is ABAB in the length direction.*

5.4.2 Tensile and compressive yielding

If we make the simple assumption that the external uniaxial force is uniformly sustained across the cross-section of a nanowire, then the stress in the interior of the nanowire at the onset of yield can be given by continuum estimate to be:

$$\sigma_{y,\mathrm{int}} = \begin{pmatrix} \sigma_f + \sigma_y & 0 & 0 \\ 0 & \frac{1}{2}\sigma_f & 0 \\ 0 & 0 & \frac{1}{2}\sigma_f \end{pmatrix} \qquad (5.12)$$

where $\sigma_y = \Pi_y$ (Fig. 5.8), which is equal to the uniaxial external force divided by the cross-sectional area. Figure 5.12(a) shows the stress, π^{11}, in the interior of the nanowire just before compressive yielding and it is very uniform. Figure 5.12 (b) shows the stress, π^{11}, in the interior of the nanowire just before tensile yielding and it is also quite uniform.

Note that the sign of the stress in the interior is reversed from compressive to tensile during the tensile loading, driven by the externally applied tensile force.

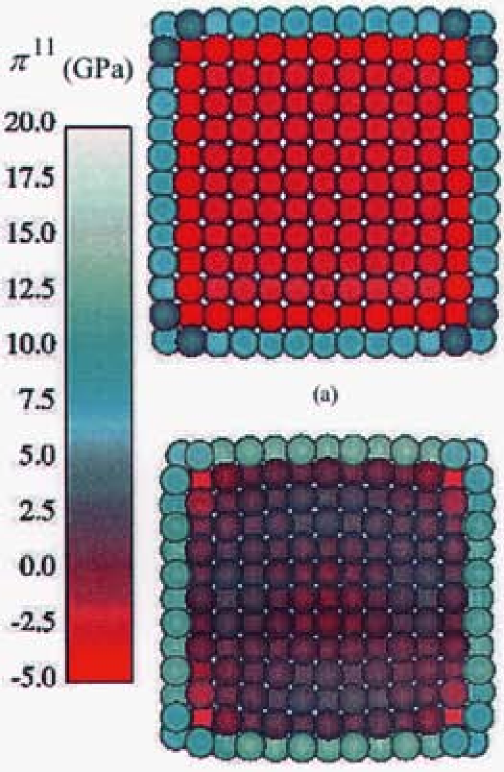

(a)

(b)

Figure 5.12. Distribution of the stress, π^{11}, on the cross-section of the 2.65nm x 2.65nm nanowire just before (a) compressive and (b) tensile yielding.

Figure 5.13 shows the average stresses, $\bar{\pi}^{11}$ and $\bar{\pi}^{22}$, in the interior of the [100] nanowires just before compressive yielding as a function of wire width and the corresponding continuum estimate (Eq. 5.12): $\sigma^{11}_{y,\mathrm{int}}$ and $\sigma^{22}_{y,\mathrm{int}}$. Figure 5.14 shows the average stresses, $\bar{\pi}^{11}$ and $\bar{\pi}^{22}$, in the interior of the [100] nanowires just before tensile yielding as a function of wire width and the corresponding continuum estimate (Eq. 5.12): $\sigma^{11}_{y,\mathrm{int}}$ and $\sigma^{22}_{y,\mathrm{int}}$. The continuum model (Eq. 5.12) predicts well the average stresses in the interior of nanowires except for very small nanowires.

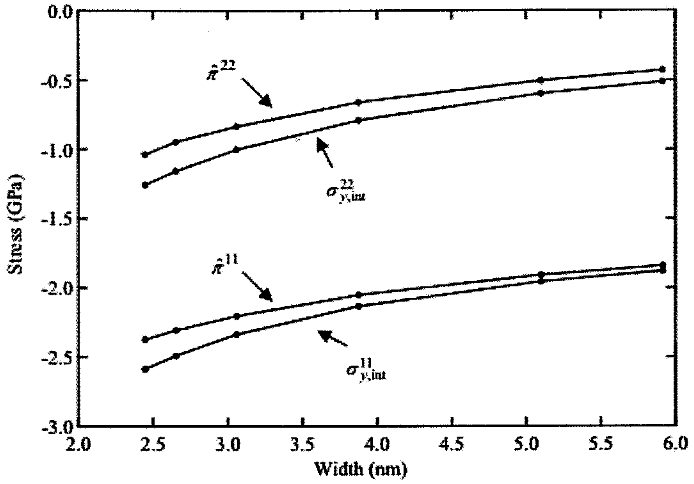

Figure 5.13. The average stresses, $\bar{\pi}^{11}$ and $\bar{\pi}^{22}$, in the interior of the [100] nanowires just before compressive yielding as a function of wire width and the corresponding continuum estimate (Eq. 5.12), $\sigma^{11}_{y,\text{int}}$ and $\sigma^{22}_{y,\text{int}}$.

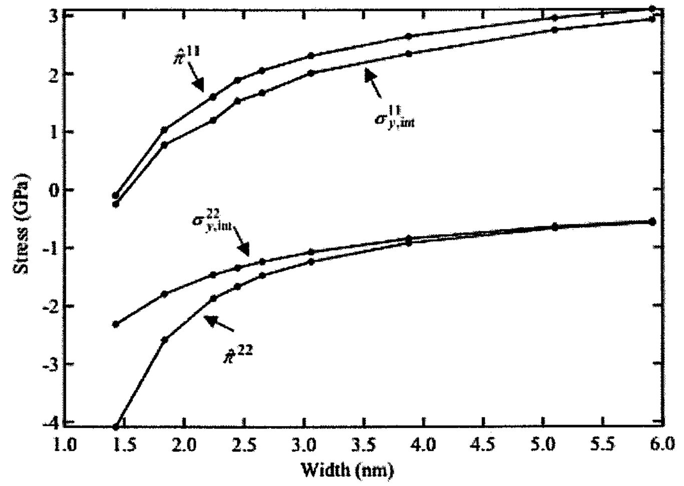

Figure 5.14. The average stresses, $\bar{\pi}^{11}$ and $\bar{\pi}^{22}$, in the interior of the [100] nanowires just before tensile yielding as a function of wire width and the corresponding continuum estimate (eq. 5.12). , $\sigma^{11}_{y,\text{int}}$ and $\sigma^{22}_{y,\text{int}}$.

5.4.3 Resolved shear stress and yield criterion

Figure 5.15 shows the distribution of the RSS, τ, in an observed slip direction on an observed slip planes of the 2.65*nm* x 2.65*nm* nanowire, (a) unrelaxed, (b) relaxed (τ_0) and (c) just before compressive yielding (τ_y), and (d,e,f) during the slip process. The RSS, τ, is essentially zero in the interior of the unrelaxed nanowire, has an average value of $\bar{\tau}_0 = 0.56\text{GPa}$ in the interior of the relaxed nanowire, and increases to $\bar{\tau}_y = 0.66\text{GPa}$ just before compressive yielding. Note that the RSS, τ, in the surface layers is negative and is thus opposite to the observed slip direction; its magnitude decreases when relaxed and decreases further during the compressive loading process. This means that the nucleation and propagation of the partial dislocation is driven by the RSS in the interior, not by that in the surface layers.

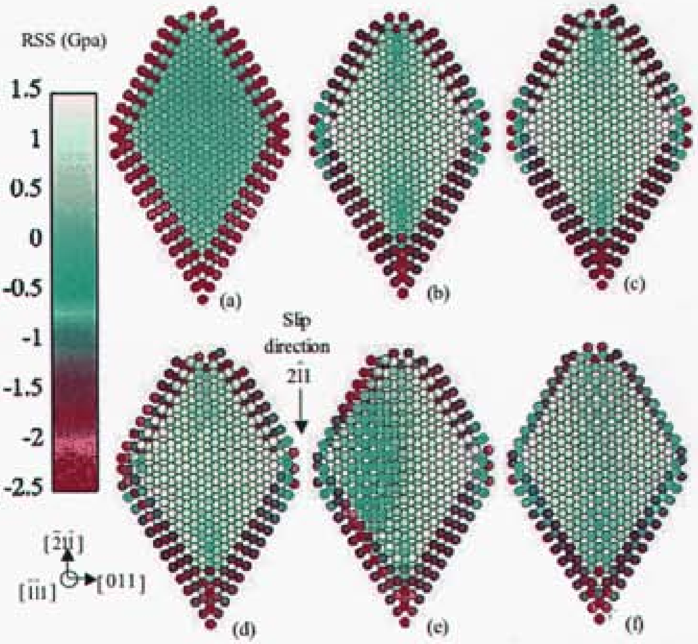

Figure 5.15. Distribution of the RSS, τ, in an observed slip direction on an observed slip planes of the 2.65nm x 2.65nm [100] nanowire, (a) unrelaxed, (b) relaxed (τ_0) and (c) just before compressive yielding (τ_y) and (d,e,f) during the slip process. The slip planes meet the periodic boundary and start from the opposite side, so only parts of the slip planes are shown.

Figure 5.16 shows the RSS, τ, in an observed leading slip direction on an observed slip plane (fig. 5.9) of the 2.65*nm* x 2.65*nm* nanowire, (a) unrelaxed (τ_0), (b) relaxed, (c) just before tensile yielding (τ_y), and (d,e,f) during the slip process. The RSS, τ, in the interior is essentially zero in the unrelaxed nanowire, has an average value of $\bar{\tau}_0 = -0.28\,\text{GPa}$ in the relaxed nanowire, changes from negative to positive during the tensile loading, and has an average value of $\bar{\tau}_y = 0.80\,\text{GPa}$ just before tensile yielding. Note that the RSS, τ, is much larger in the surface layers where the partial dislocation nucleates than in the interior. Dislocation nucleation involves the dislocation moving away from its image at the surface and creating stacking fault, which implies that there is a nucleation barrier at a critical distance from the surface. It is at this distance that the nanowire must attain a critical RSS. An ill-defined dislocation may easily nucleate at a surface with high RSS; a full-fledged dislocation nucleates only after the RSS at a distance from the surface reaches a critical value. Once nucleated, a dislocation will propagate quickly throughout the nanowire since it is much easier to propagate a dislocation.

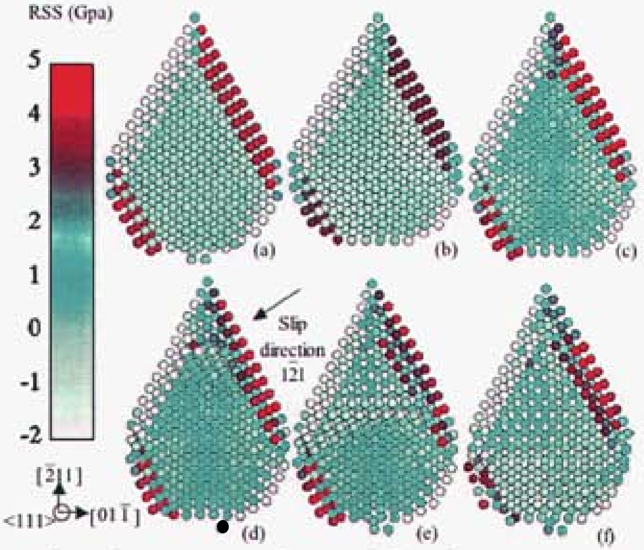

Figure 5.16. RSS, τ, distribution in an observed slip direction on an observed slip plane (fig. 5.9) of the 2.65nm x 2.65nm [100] nanowire, (a) unrelaxed (τ_0), (b) relaxed, (c) just before tensile yielding (τ_y), and (d,e,f) during the slip process. The slip planes meet the periodic boundary and start from the opposite side, so only parts of the slip planes are shown.

While the dislocation nucleation criterion is still a topic of considerable study [38,39], dislocation nucleation in a nanowire seems related to the RSS in the interior for both the compressive and tensile yielding based on the above reasoning. Since the RSS, τ, in the interior of a nanowires is quite uniform, its averaged value over the interior of the nanowire just before yield ($\bar{\tau}_y$) is calculated and shown in fig. 5.17. The critical RSS, $\bar{\tau}_y$, does not change significantly with the nanowire size and can thus serve as a "local" yielding criterion. That is, when the RSS averaged over the interior of a nanowire, $\bar{\tau}$, reaches a critical value $\bar{\tau}_y$, the nanowire yields. This local criterion is enhanced by the fact it also applies to nanowires of different side surfaces; the [100] nanowire with (011) and $(0\bar{1}1)$ side surfaces (fig. 5.17) has almost the same critical RSS', $\bar{\tau}_y$, as in the [100] nanowires with (010) and (001) side surfaces. However, the critical RSS, $\bar{\tau}_y$, still depends on orientation and loading condition (tension vs. compression), suggesting a lack of a universal Schmidt-law-type criterion for the yielding of nanowires.

Since the average stress in the interior of a nanowire is well predicted by the continuum model (Eqs. 5.1, 5.2 and 5.12) except for very small nanowires, so is the average RSS, $\bar{\tau}$, in the interior. This implies that the local criterion can be of practical use if the critical RSS, $\bar{\tau}_y$, is known. That is, the average RSS, $\bar{\tau}$, in the interior of a nanowire, which is exerted by both the surface stress and external uniaxial force, can be estimated from the continuum model and compared with the critical RSS, $\bar{\tau}_y$, to determine if the nanowire will yield.

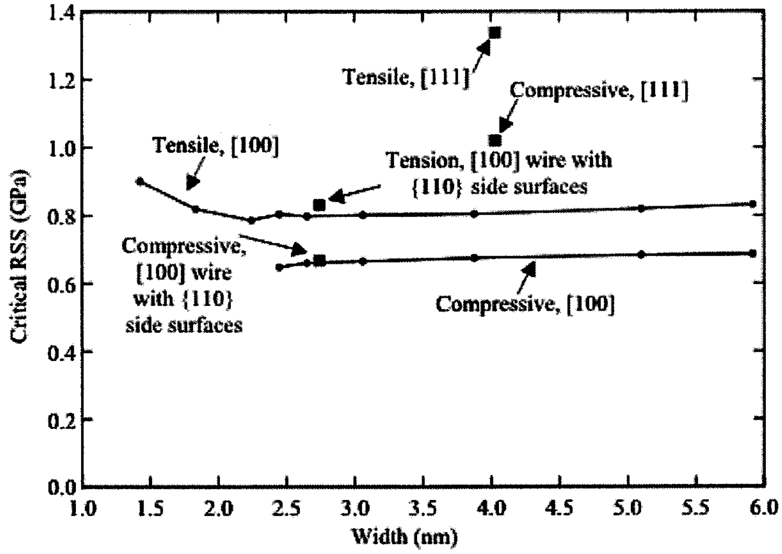

Figure 5.17. The critical RSS, $\bar{\tau}_y$, averaged over the interior of the [100] nanowires just before compressive and tensile yielding. These of the [111] nanowires and the [100] nanowires with {110} side surfaces are also shown.

In an effort to explain the orientation and loading condition (tension vs. compression) dependence of the critical RSS, $\bar{\tau}_y$, we examined the effect of the normal stress on the {111} slip plane on the yielding. We displaced one block of atoms relative to another along a <112> direction on a {111} plane with different normal stresses applied on the {111} slip plane (see ref. [40] for details of the simulation method). With normal stresses comparable to these observed in the nanowire simulations applied, the change in the maximum shear stress is negligible compared to the maximum shear stress itself. So to first order accuracy, the yielding of the nanowires is not strongly influenced by the normal stress on the slip plane. The orientation and loading condition (tension vs. compression) dependence of the critical RSS, $\bar{\tau}_y$, is probably due to the fact that the structures (lattice spacing) of the nanowires before yielding are very different from each other. For example, due to the very large yield strain, the lattice spacing in the length direction of the [100] nanowires just before tensile and compressive yielding is as large as 15% apart (fig. 5.7).

The local criterion can be invoked to explain the size dependence of the yielding. The RSS, $\bar{\tau}$, averaged over the interior of a nanowire has contributions from both the external forces and surface-stress-induced intrinsic compressive stress. For compressive yielding, these two contributions have the same sign and enhance each other. The smaller the nanowire, the larger the contribution from the surface-stress-induced intrinsic compressive stress, and the smaller external force is required to make the nanowire yield. When a [100] nanowire is smaller than 2.45*nm* x 2.45*nm*, the nanowire yields under its own surface-stress-induced intrinsic compressive stress and no external force at all is necessary.

For tensile yielding, the two contributions have opposite signs. The external force must first overcome the surface-stress-induced compressive intrinsic stress to make a nanowire yield under tension. The smaller the nanowire, the larger the magnitude of the intrinsic stress that have to be overcome, and the larger external force is required to make the nanowire yield.

The uniaxial Schmidt factor (Table 5.2) for the most favorable {111}<112> partial slip systems in the [100] nanowires is larger under compression than under tension, and thus makes it easier for [100] nanowires to yield under compression. The surface-stress-induced intrinsic compressive stress also contributes to compressive yielding and has to be overcome in tensile yielding. The critical RSS, $\hat{\tau}_y$, is smaller for compressive yielding (fig. 5.17) than for tensile yielding. These three factors together explain the significant tensile/compressive yield stress asymmetry (fig. 5.6, 5.8) in the [100] nanowires.

For the [111] nanowires, the Schmidt factor for the most favorable {111}<112> partial slip systems is larger under tension than under compression (Table 5.2), thus makes it easier for [111] nanowires to yield under tension; but the surface-stress-induced intrinsic compressive stress contributes to compressive yielding. These two factors cancel each other and the yielding of the [111] nanowires is quite symmetric (Fig. 5.6).

5.5 Conclusions

We have identified two key factors that have to be considered in the yielding of metal nanowires: (1) intrinsic stress in the wire induced by surface stress, and (2) different active slip systems for nucleation and propagation of dislocations. The two factors lead to a much different yield behavior in nanowires relative to bulk single crystal and polycrystalline materials. Our main conclusions are:

1. The tensile surface stresses on the side surfaces of metal nanowires cause them to contract along the length with respect to bulk fcc lattice and induce compressive stress in the interior of the nanowires. Below a critical size, the surface stresses can induce yielding on its own.
2. Nanowires yield via the nucleation and propagation of {111}<112> partial dislocations under external forces and surface stresses.
3. A local yield criterion based on the RSS in the interior of the nanowires is proposed and invoked to explain the observed size dependence of the yielding behavior.
4. The magnitude of the tensile yield stress is much larger than that of the compressive yield stress for very small [100] nanowires, due to the effect of surface stress and different slip systems active in tensile and compressive yielding. For [111] nanowires these two factors cancel each other and the yielding of [111] nanowire is quite symmetric.

5.6 Acknowledgements

We thank Dr. Steve Plimpton for letting us use his ParaDyn code for Embedded Atom Method (EAM) Molecular Dynamics.

5.7 References

[1] Kondo, Y., Takayanagi, K., Synthesis and characterization of helical multi–shell gold nanowires. Science 2000; 289: 606–608.

[2] Kondo, Y., Ru, Q., Takayanagi, K., Thickness induced structural phase transition of gold nanofilm. Phys. Rev. Lett. 1999; 82: 751–754.

[3] Kondo, Y., Takayanagi, K., Gold nanobridge stabilized by surface structure. Phys. Rev. Lett. 1997; 79: 3455–3458.

[4] Hasmy, A., Medina, E., Thickness induced structural transition in suspended fcc metal nanofilms. Phys. Rev. Lett. 2002; 88: 096103.

[5] Gülseren, O., Ercolessi, F., Tosatti, E., Noncrystalline structures of ultrathin unsupported nanowires. Phys. Rev. Lett. 1998 ; 80: 3775.

[6] Tosatti, E., Prestipino, S., Kostlmeier, S., Dal Corso, A., Di Tolla, F. D., String tension and stability of magic tip-suspended nanowires. Science 2001; 291: 288–290.

[7] Hall, B. D., Flüeli, M., Monot, R., Borel, J.–P., Multiply twinned structures in unsupported ultrafine silver particles observed by electron diffraction. Phys. Rev. B 1991; 43: 3906–3917.

[8] Marks, L. D., Surface structure and energetics of multiply twinned particles. Philos. Mag. A 1984; 49: 81–93.

[9] Miller, R.E., Shenoy, V.B., Size-dependent elastic properties of nanosized structural elements. Nanotechnology 2000; 11: 139–147.

[10] Segall, D.E., Ismail-Beigi, S., Arias, T.A., Elasticity of nanometer-sized objects. Phys. Rev. B 2002; 65: 214109.

[11] He, L.H., Lim, C.W., Wu, B.S., A continuum model for size-dependent deformation of elastic films of nano-scale thickness. Int. J. Solids Struct., 2003; 41: 847-857.

[12] Diao, J., Gall, K., Dunn, M. L., Surface-stress-induced phase transformation in metal nanowires. Nature Materials 2003; 2: 656.

[13] Diao, J., Gall, K., Dunn, M. L., Yield strength asymmetry in metal nanowires. Nano Letters 2004; 4: 1863 – 1867.

[14] Diao, J., Gall, K., Dunn, M. L., Surface stress driven reorientation of gold nanowires. Physical Review B 2004; 70: 075413.

[15] Diao, J., Gall, K., Dunn, M. L., Atomistic simulation of the structure and elastic properties of gold nanowires. Journal of the Mechanics and Physics of Solids 2004; 52: 1935-1962.

[16] Gall, K., Diao, J., Dunn, M. L., The strength of gold nanowires, Nano Letters 2004; 4: 2431 – 2436.

[17] Gall, K., Diao, J., Haftel, M., Dunn, M. L., Bernstein, N., and Mehl, M.J., Tetragonal phase transformation in gold nanowires. Journal of Engineering Materials and Technology 2005; 127: 417-422.

[18] X. Y. Zhang, L. D. Zhang, Y. Lei, L. X. Zhao and Y. Q. Mao, Fabrication and characterization of highly ordered Au nanowire arrays, J. Mater. Chem. 2001; 11:1732–1734.

[19] Gates, B., Mayers, B., Cattle, B., and Xia, Y.N., Synthesis and characterization of uniform nanowires of selenium, Adv. Funct. Mater. 2002 ; 12 : 219–227.

[20] Brandbyge, M., Schiotz, J., Sorensen, M.R., Stoltze, P., Jacobsen, K.W., Norskov, J.K., Olesen, L., Laegsgaard, E., Stensgaard, I.. and Besebbacher, F., Quantized conductance in atom-sized wires between two metals, Phys. Rev. B 1995; 52: 8499-8514.

[21] Rubio, G., Agrait, N., and Vieira, S., Atomic-Sized Metallic Contacts: Mechanical Properties and Electronic Transport, Phys. Rev. Lett 1996; 76: 2302-2305.

[22] Rubio-Bollinger, G., Bahn, S. R., Agraït, N., Jacobsen, K.W. and Vieira, S., Mechanical properties and formation mechanisms of a wire of single gold atoms. Phys. Rev. Lett 2001; 87: 026101.

[23] Ohnishi, H., Kondo, Y., and Takayanagi, K., Quantized conductance through individual rows of suspended gold atoms. Nature 1998; 395: 780–783

[24] Rodrigues, V., Fuhrer, T., and Ugarte, D., Signature of atomic structure in quantum conductance of gold nanowires, Phys. Rev. Let. 2000; 85: 4124-4127.

[25] Rodrigues V., and Ugarte, D., Real-time imaging of atomistic process in one-atom thick metal junctions, Phys. Rev. B 2001; 63: 073405.

[26] Yanson, A. I., Bollinger, G. R., van der Brom, H. E., Agrait, N. and Ruitenbeek, J. M., Formation and manipulation of a metallic wire of single gold atoms, Nature 1998; 395: 783-785

[27] Marszalek, P.E., Greenleaf, W.J., Li, H.B., Oberhauser, A.F., and Fernandez, J.M., Atomic force microscopy captures quantized plastic deformation in gold nanowires. PNAS 2000; 97: 6282–6286.

[28] Horstemeyer, M.F., Baskes, M.I., and Plimpton, S.J., Length scale and time scale effects on the plastic flow of fcc metals. Acta mater. 2001; 49: 4363–4374

[29] Liang, W. W., and Zhou, M., Size and strain rate effects in tensile deformation of Cu nanowires. Nanotech 2003; 2: 452–455.

[30] Sorensen, M. R., Brandbyge, M. and Jacobsen, K. W., Mechanical deformation of atomic-scale metallic contacts: structure and mechanisms. Phys. Rev. B 1998; 57:3283–3294.

[31] Kang Jeong-Won and Hwang, Mechanical deformation study of copper nanowire using atomistic simulation. Nanotechnology 2001; 12: 295–300.

[32] Liang, H. Y., Wang, X. X., Wu, H, G., Wang, Y., Acta mecnanica sinica 2002; 34:208–215.

[33] Foiles, S.M., Daw, M.S., Baskes, M.I.,. Embedded-atom-method functions for the fcc metals Cu, Ag, Au, Ni, Pd, Pt, and their alloys. Physical Review B 1986; 33, 7983.

[34] Zimmerman, J. A., Kelchner, C. L., Klein, P.A., Hamilton, J. C., and Foiles, S. M., Surface step effects on nanoindentation. Phys. Rev. Lett. 2001; 87: 165507

[35] Egami, T., Maeda, K., Vitek, V., Structural defects in amorphous solids: a computer simulation study. Philosophical Magazine A 1980; 41: 883.

[36] Cheung, K. S., Yip, S., Atomic-level stress in an inhomogeneous system. J. Appl. Phys. 1991; 70: 5688–5690.

[37] Zhou, M., A new look at the atomic level virial stress: on continuum-molecular system equivalence. Proc. R. Soc. Lond. A, 2003; 459: 2347–2392.

[38] Miller, R.E., Acharya, A., A stress-gradient based criterion for dislocation nucleation in crystals. Journal of the Mechanics and Physics of Solids 2004 ; 52: 1507-1525.

[39] Li, J., Van Vliet, K.J., Zhu, T., Yip, S., Suresh, S., Atomistic mechanisms governing elastic limit and incipient plasticity in crystals. Nature 20002; 418: 307.

[40] Zimmerman, J. A., Gao H. J., and Abraham, F. F., Generalized stacking fault energies for embedded atom FCC Metals. Modelling Simul. Mater. Sci. Eng. 2000; 8: 103–115.

[41] Fiorentini, V., Methfessel, M., Schoffler, M.,. Reconstruction mechanism of fcc transition metal (001) surfaces. Phys. Rev. Lett. 1993; 71: 1051–1054.

[42] Needs, R.J., Godfrey, M.J., Mansfield, M., Theory of surface stress and surface reconstruction. Surface Science 1991; 242: 215–221.

[43] Mays, C.W., Vermaak, J.S., Kuhlmann-Wilsdorf, D., On surface stress and surface tension 2. Determination of the surface stress of gold. Surf. Sci. 1968; 12 :134–140.

6 Incipient Yielding Behavior During Indentation for Gold Thin Films Before and After Annealing

We study the deformation mechanisms and mechanics during indentation of polycrystalline gold thin films at depths below 100 nm. The measured material hardness decreases from 2.1 ± 0.1 to 1.7 ± 0.1 GPa after annealing for 4 hours at 177 °C. Upon closer inspection, the hardness trends in the gold thin films were discovered to vary according to the indentation depth. At nanometer depths, the material hardness was quantified using multiple parameters, some of which are independent of the area calibration for the tip. The annealed specimen was very "hard" at low indentation depths, relatively soft at moderate indentation depths, and finally harder until the grain-size limit was reached. The as-deposited specimen demonstrated a relatively continuous harness trend as function of indentation depth, exhibiting monotonic convergence to Hall-Petch limited behavior. Discrete displacement jump events (excursions or "pop-ins") were frequently observed for the annealed specimen, but not for the as-deposited specimen. Variation in hardness, excursion activity, as well as displacement during the hold at maximum load was observed according to the applied loading, which was parametrically varied at constant strain rates. Hardness results are explained in terms of the population and evolution of defects present within the specimens. The population of point defects is also influential, and critical thermal fluctuations, as well as the thermally activated process of diffusion, are believed to influence hardness at the specimen's free surface and further into its volume. After converging to a monotonic trend (proper tip engagement), the modulus of the gold was measured to be 106.0 ± 12.9 and 101.3 ± 6.0GPa for the respective Au/Cr/Si specimens. These values exceed predictions from the aggregate polycrystalline material theory, a representation used to estimate results for anisotropic single crystals. Exaggerated modulus measurements are explained as the result of the contribution of modulus mismatch with the substrate, pile-up at the indenter tip, residual stress in the films, and crystallographic anisotropy of the gold.

6.1 Introduction

Studies of the instrumented indentation of gold thin films include [1,2,3,4,5,6,7,8,9]. Researchers have also examined the indentation behavior of other thin face centered cubic (FCC) metal films including copper [10,11], aluminum [2], nickel [12], and silver [13,14]. Almost all of these studies demonstrate increased hardness compared to bulk specimens of the same material. Greater hardness is often seen in association with decreased grain size in thin film specimens. Because of the association between strength and grain size, grain size has been systematically altered in studies according to deposition technique [2], deposition conditions [3,6,9], and through the use of post-deposition annealing [3,4,9,10,12,13]. In other studies, hardness was altered by maintaining specimens at elevated temperatures while performing indentation [1,7]. In some instances, the occurrence of discrete deformation events, *i.e.* excursions or "pop-ins", was observed during loading [2,5,8,9]. Such aberrant behavior during indentation has been associated with dislocation formation [5,15], twinning [14], friction between the tip and specimen [16], oxide fracture [17], phase transformation [18], film cracking or delamination [4], or the crushing of surface asperities.

Indentation of polished then annealed single crystals of gold [15,20] or silver [21], for example, has provided evidence of an "indentation size effect" phenomenon. The indentation size effect refers to an initially high hardness at small indentation depths, converging to the bulk value as the indentation into the specimen becomes increasingly deeper. The effect typically applies to indentation depths in the submicrometer range, and is distinctly different than a strain gradient-based size effect, *i.e.* strain gradient plasticity, which may dominate at a larger scale (micrometers) [22]. Even early on [15,19], the indentation size effect was explained according to the sudden nucleation and propagation of dislocations in defect free volumes of material at the specimen's surface as opposed to the inhibited motion of dislocations in an increasingly defect rich material at greater depths within the specimen. It is worth noting that the evolution of dislocations is not the only potential cause of an indentation size effect at nanometer scales. For example, the interaction between the indenter tip and surface of the specimen may also play a role.

Recent work has demonstrated an indentation size effect that is influenced by the occurrence of excursion activity [9]. This study also illustrated a decrease in excursion activity (and maximum contact pressure) near grain boundaries as well as an initial softening of the specimen, followed by hardening in films containing relatively few grains within the sample volume. Others have recently suggested that incipient plasticity may be influenced by point defects [23], therefore any associated excursion activity may not be truly homogeneous in nature. If so, then initial plasticity would always be influenced by the specimen temperature as well as the applied strain rate, because of the thermally activated nature involved in the evolution of point defects. Lastly, the recent compression of ion-milled gold films has suggested the existence of a "dislocation starvation" mechanism [8], where, for specimens of a certain size, dislocations may escape more rapidly than they are formed. These recent insights suggest that the indentation of even basic thin film specimens is not fully understood.

We aim to further understand the deformation of metal films by studying the indentation of Au thin films. Unlike many previous studies we control the properties of the specimen (grain size) by annealing specimens made in the *same* fabrication batch. Also unique to our study, we investigate the effect of the applied loading, *i.e.* the strain rate, for very small sample volumes of material. We also emphasize unique hardness trends at very small indentation depths and demonstrate that hardness can crossover at small depths between as-deposited and annealed materials. The various phenomenon we identify and analyses we perform are critical at very small indentation depths and are useful when it is not possible to perform indentations in relatively soft metals to depths exceeding 100 nm due to physical size limitations. The specific goals of our study are to gain insight into the incipient plasticity mechanisms at (excursions & aberrant activity, loading profile), measure expected material property values (hardness and modulus), and evaluate indentation test procedures (property value convergence, etc.) at sub 100 nm depths. Finally, our study is unique in this regard because we examine "intermediate" polycrystals, and not ideal dislocation free single crystals or defect rich polycrystalline macroscopic materials.

6.2 Experimental Techniques

A series of designated test structures was fabricated using the Multi-User MEMS Process (MUMPs) provided by the MEMSCAP Corporation [24]. The process is most often used to create microelectromechanical systems (MEMS) structures. Here, however, the MUMPs was used to create more traditional thin metal film specimens (of millimeter-sized square geometry) and not miniaturized structures. In one of the final steps of the standardized procedure, a 500 nm thick layer of gold (99.999% purity) is deposited using e-beam evaporation, with the chamber being nominally unheated. After being cut to size, separate specimens were annealed at room temperature or 177 °C for 4-hours. The annealing temperatures are sufficiently low such that the 20 nm thick chromium layer, used to adhere the gold to the polycrystalline silicon underneath, was not observed to diffuse into the other materials [25].

A Nano DCM (MTS Systems Corp.) was used to indent into the specimens with a diamond Berkovitch tip at room temperature. When performed in "continuous stiffness" mode [26], instrumented indentation can be used to obtain the hardness and modulus of a material at discrete instances (unloading events) throughout its thickness, according to the Oliver-Pharr method [27]. Once the tip has engaged the material's surface, the machine is capable of resolving applied load increments lesser than 1 μN, with displacement resolution less than 1 nm. Based on knowledge of the methods as well as the standard deviation of the data sets, instrumented indentation is accurate to within about 5-10% of the measured values, being most repeatable when the results of multiple indentations are averaged.

Specifics details of the indentation experiments are as follows: Immediately prior to the tests, the instrument was calibrated against the elastic modulus of fused silica [27], with the area coefficients for the tip being chosen to achieve a good fit to the CSM data, even at shallow depths, *i.e.* 50 nm. After calibration, the modulus and corrected (Berkovitch) hardness for the fused silica sample were determined to be 73.6 ± 0.8 GPa and 10.5 ± 0.2 GPa, respectively. For the measurements, the sink-in parameter, ε, was assumed to be 0.75 and the tip geometry factor, β, was assumed to be 1.05, based on recent investigations [28]. A series of 15 indents was made at a constant (loading) strain rate [29] of 0.500, 0.100, 0.050, 0.010, or 0.005 s^{-1}. A mismatch exists between the modulus of the gold and that of the silicon, therefore, as proposed in the literature [30], the contact depth of ~10% of the film thickness was observed in order to avoid the effect of substrate compliance. That is, indentation into the specimens was performed no deeper than 60 nm, with material property values extracted at the maximum depth. The test procedure consisted of a "trapezoidal" loading profile, which consists of an applied loading, then a hold at the maximum load for 30 seconds to stabilize the material, then unloading at constant strain rate, and finally a hold at 10% of the maximum load for 30 seconds to obtain a thermal drift correction. To ensure isolation between tests, spacing between indents was at least 75 µm. After testing, the precise location of the specimen surface was manually corrected from the P/h indentation profiles, but was typically already within 3 nm for an automated criterion based on a change in measured stiffness.

Scanning electron microscopy (SEM) was performed using a JEOL 5910 (JEOL Lmtd.). Comparative pairs of secondary- (SEI) and backscatter- electron images (BEI) were captured at five different magnifications. An acceleration voltage of 10 keV at the working distance of 8 mm was used to limit the extent of beam penetration into the specimens, thereby increasing the spatial resolution of the BEI data. The backscatter detector was set to favor compositional contrast. A Dimension 3100 (Veeco Instruments, Inc.) Atomic Force Microscope (AFM) was used to perform surface scans in tapping mode. The radius of curvature of the RTESP (silicon) tips used is nominally 10 nm. The surface locations were measured twice using 3Å~3 µm scans with 512 pixels in each direction (*i.e.*, ~6 nm lateral resolution) and then processed using comparative thermal compensation, plane-fit, and low pass filter routines.

6.3 Data Reduction Models and Methods

Indentation was performed at a constant strain rate according to the applied load, which can be related to the standard (displacement based) indentation strain rate, Equation 6.1, [29].

$$\dot{e}_{ip} = \frac{\dot{P}}{P} = 2\frac{\dot{h}}{h} = 2\dot{e}_{ih} \qquad (6.1)$$

In Equation 1, $\dot{e}_{ip}$ represents the load based strain rate $\{s^{-1}\}$, P the applied load {N}, h the nominal tip displacement into the specimen {m}, and $\dot{e}_{ih}$ represents the displacement based strain rate $\{s^{-1}\}$. The advantages of the constant strain rate loading include the proportionally greater number of data points obtained at lesser indentation depths as well as ideally constant hardness at greater indentation depths [29,48]. Because the Nano DCM is load controlled in a closed-loop manner, the measured strain rate was seen to converge to the specified value before the indenter tip was 2-3 nm into the specimen surface.

The effective modulus can be determined from

$$E_{eff} = \left. \frac{S\sqrt{\pi}}{2\beta\sqrt{A[hc]}} \right|_{\text{unload}}, \tag{6.2}$$

and is evaluated during the unloading of the indenter tip [27]. In Equation 6.2, E_{eff} represents the effective modulus {Pa}, S the unloading stiffness ($\partial P/\partial h$) {N/m}, π the mathematical constant (3.14159), $A[h_c]$ the area function for the tip {m^2}, and h_c the corrected indentation depth {m}.

The effective modulus can be related to the specimen's elastic modulus, given the elastic properties of the indenter,

$$\frac{1}{E_{eff}} = \frac{1-\nu_s^2}{E_s} + \frac{1-\nu_i^2}{E_i}. \tag{6.3}$$

New symbols introduced in Equation 6.3 include ν, which represents the Poisson's ratio {unitless}, the subscript *s,* which represents the specimen and the subscript *i,* which represents the indenter tip. E_i and ν_i were assumed to be 1141 GPa and 0.07, respectively, for the diamond indenter tip. Perhaps most noteworthy, the Poisson's ratio of the specimen must be known *a priori* in order to calculate the modulus from the plain strain modulus, E_{eff}, Equation 3. The modulus of 115.3 GPa and Poisson's ratio of 0.37 might be expected for the gold, based on the <111> anisotropic values, *i.e.* the dominant texture of the gold films [25,31-33]. The indentation of a single crystal has been studied, even for the case of highly anisotropic material [34,35]. These studies suggest that the Hill material property values (the average of the isostress and isostrain conditions) are reasonable estimates, even when indenting anisotropic single crystals. Furthermore, the stress distribution beneath an indenter tip is not purely compressive, rather it is multi-axial. For example, the principle stress magnitudes were seen to vary in a 3:2 proportional for the out of plane relative to the in-plane directions in finite element analysis of a uniform gold alloy material [36]. The strain field can span several grains within a *polycrystalline* material, depending on grain size and indentation contact area. Therefore, modulus of 77.7 GPa and Poisson's ratio of 0.43 were assumed for the gold, based on the polycrystalline aggregate values [37]. Note that the influence of material anisotropy on hardness has been examined in the literature [38].

The mean contact pressure, sometimes referred to as the "universal hardness", is given by

$$H_U = \left.\frac{P}{A[h]}\right|_{\text{instantaneous}} \tag{6.4}$$

In Equation 6.4, H_u represents the contact pressure {Pa}, which may be determined at any instant during indentation from the contact area function. For soft metals, such as gold, the universal hardness is typically very close to the value of the corrected (Berkovitch) hardness.

The area function for the tip is given in [27],

$$A[h] = \sum_{n=0}^{8} C_n (hc)^{2-n} = C_0 hc^2 + C_1 hc + C_2 hc^{\frac{1}{2}} \ldots + C_8 hc^{\frac{1}{128}}. \tag{6.5}$$

The function is primarily based on the tip's projected area of contact [39], with additional terms included for correction, particularly at shallow depths. In our experiments, the first five coefficients were determined and then utilized in data reduction.

The Hertzian fit for elastic contact is described in [40],

$$P_{Hertz} = \frac{4\sqrt{R}h^{\frac{3}{2}}E_{eff}}{3}. \tag{6.6}$$

The equation may be used to approximate the force present for elastic contact between the indenter tip and the specimen at very shallow indentation depths, when the blunted Berkovitch tip typically acts as a spherical indenter. The variable P_{Hertz} represents the Hertz contact force {N}, and R the tip radius {m}. The tip radius was estimated to be 110 nm, when Equation 6.6 was compared to the CSM indentation of the fused silica calibration standard. For CSM data, a single term area function, Equation 6.2 and Equation 6.5, can also be used to determine the tip radius, with the C_1 value being equal to the quantity $2\pi R$, and other C_n values being zero.

The "Berkovitch fit" for fully developed contact is described by

$$P_{Berk} = C_0 h^2 H_{fd}. \tag{6.7}$$

The equation may be used to estimate the force acting on the tip when it has fully engaged the specimen and the blunted tip effect is negligible. In Equation 6.7, P_{Berk} represents the Berkovitch contact force {N}, C_0 the coefficient from the area function at large depths (here 24.5174), and H_{fd} the fully developed hardness {Pa}. In this case, a value of 2.1 GPa was assumed for the gold films based on the maximum (strain hardened) value observed for the as-deposited film.

The mean stress for the case of Hertzian contact is given in [40],

$$\sigma_{H,mean} = \frac{P}{\pi R h} = \frac{4\sqrt{h}E_{eff}}{3\pi\sqrt{R}}. \tag{6.8}$$

In the case of elastic loading, Equation 6.8 may provide a more accurate representation of the local stress than Equation 6.4. Equation 6.8 is of greatest utility when the tip may be approximated as spherical, *i.e.* a good fit for Equation 6.6. Variables used in Equation 6.8 are already defined, except for, $\sigma_{H,mean}$, which represents the local mean stress {Pa}.

6.4 Results

Results of SEM characterization of the gold films are shown in Figure 6.1. The backscattered images demonstrate a nano-scale grain size in the as-deposited material, with secondary (so-called "abnormal") grain growth observed as the result of annealing. During annealing, many grains grow to become sub-micron sized or greater, *i.e.* > 160 μm^2. Note that some abnormal grains are seen even in the as-deposited gold, Figure 6.1. Results for multilayer (Au/Cr/Si) microcantilever structures constructed within the MUMPs fabrication batch are explored in much greater detail in [25]. Briefly, the films featured a dominant <111> crystallographic texture with a minor <001> component. The sub-surface defect structure of the tapered columnar grains contained numerous twins, with relatively few line defects being observed, even after annealing.

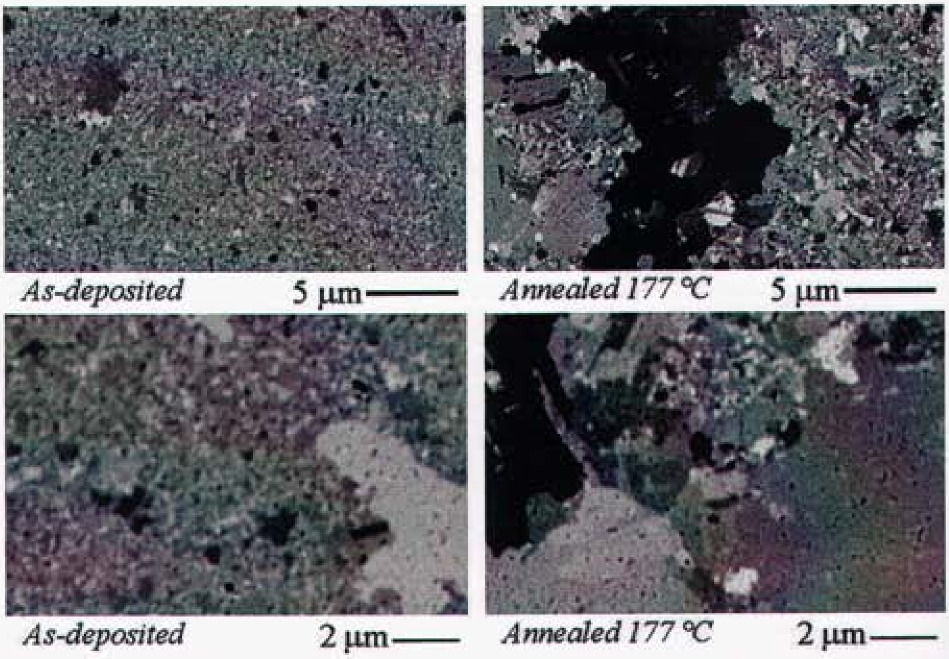

Figure 6.1. Backscattered SEM micrographs demonstrating the grain size and geometry for the as-deposited and annealed gold films. Greater detail is shown in the second (lower) image pair, which was obtained at higher magnification.

AFM surface profiles are shown in Figure 6.2, and are quantified in Table 6.1.

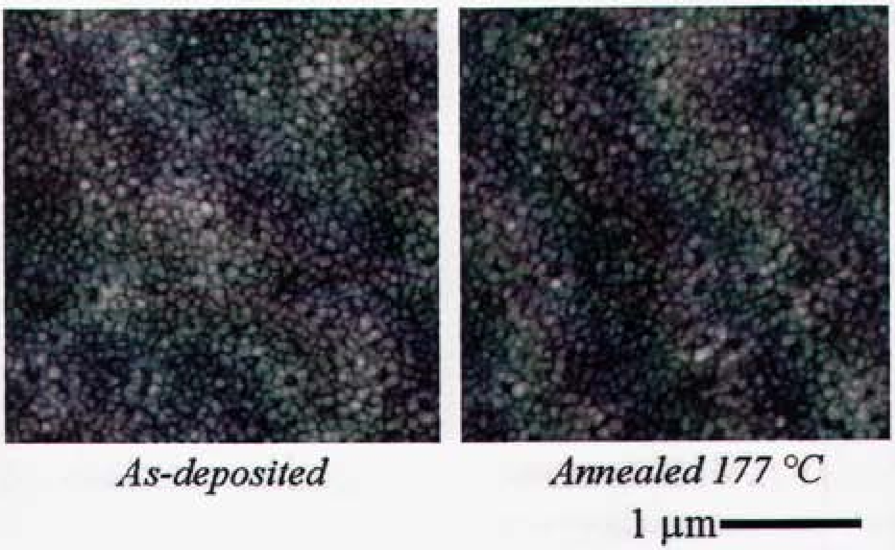

Figure 6.2. AFM profiles of the surface of the as-deposited and annealed gold thin film specimens. The nodular surface texture is virtually identical for both of the specimens.

Table 6.1 Numerical results for AFM characterization. The roughness values suggest that the surfaces shown in Figure 6.2 are indeed very similar.

	Thermal Treatment	
Roughness {nm}	As-deposited	177 C
Ra	3.62	3.74
Rrms	4.52	4.67
Rmax	35.5	44.1

The surface profiles demonstrate a uniform nodular surface texture, with some near-surface porosity, *i.e.* "dimples". In Figure 6.2, the surfaces of the two specimens are not obviously different, despite their different thermal histories and vastly different sub-surface grain structure, Figure 6.1. The similar nature of the surfaces is also apparent in Table 6.1, for both the average and rms (standard deviation) roughness. The nodule and dimple size was found to be 59 ± 13 and 55 ± 14 nm in diameter, respectively [25]. Note that grain boundaries were not observed in Figure 6.2 or in prior AFM characterization [25], where annealing at 225 °C enabled chromium and silicon diffusion and obvious grain delineation was observed only in SEM. The roughness values observed here are, however, ~60% less than those measured previously for microcantilevers made in the same fabrication batch. The difference is attributed to the different instruments used to characterize the films and the values presented here are believed to be more accurate.

Representative indentation profiles are shown in Figure 6.3. Figure 6.3 compares an as-deposited specimen to another annealed at 177 °C for 4 hours.

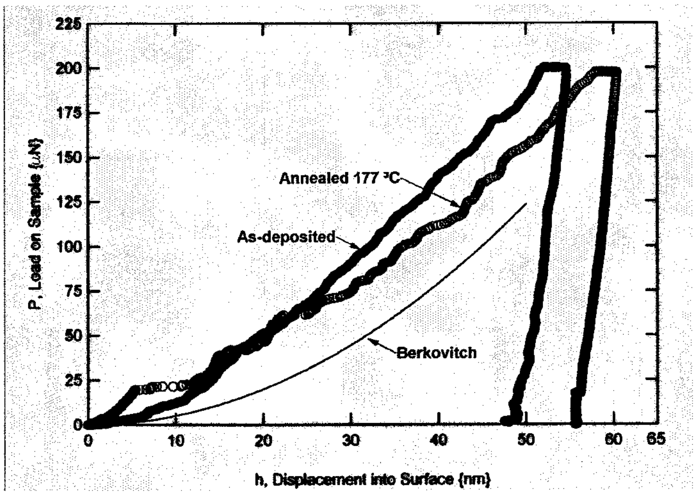

Figure 6.3. Indentation loading profiles for as-deposited and annealed specimens. Note that the profiles intersect for indentation depths between 10 and 30 nm but both become parallel to the Berkovitch fit at deeper depths.

The profiles for the two specimens, both indented at a constant strain rate of 0.050 s^{-1}, are observed to consistently intersect between depths of 10 and 30 nm. The slope of each indentation profile is observed to become parallel to the ideal Berkovitch loading curve at greater depths, Figure 6.3. Note that the Berkovitch fit shown in Figures 6.3 and 6.4 is based on the converged hardness of as-deposited specimen; a second such fit might be separately applied to the annealed specimen, because of its greater grain size and corresponding lesser hardness at large indentation depths. However, at low indentation depths, the Hertzian fit is more appropriate for comparison between the as-deposited and annealed specimens. Each of the illustrated profiles, Figure 6.3 and 6.4, are typical for the two specimens, at the various loading rates utilized. Also, all indentation profiles were observed to occupy the region between the Hertz and Berkovitch fits, which might be considered the upper and lower bounds for the indentation experiments.

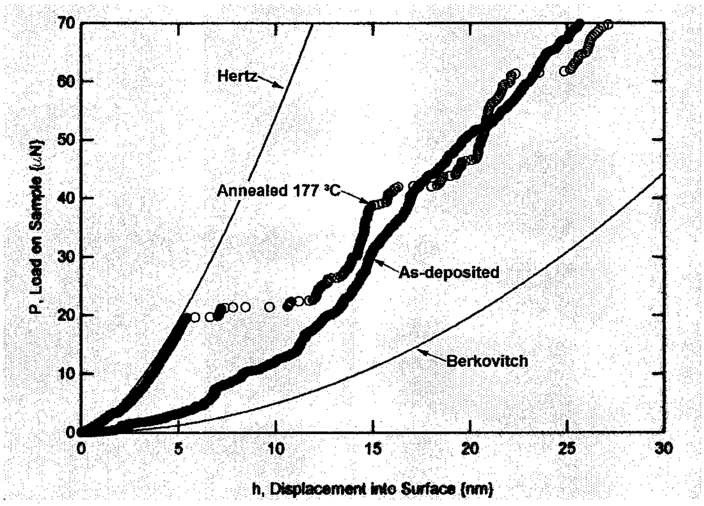

Figure 6.4. Initial portion of indentation loading profiles, Figure 6.3 for the as-deposited and annealed specimens. The annealed specimen adheres well to the Hertz fit, until discrete excursion events are observed in its profile. The as-deposited specimen is more similar to the Berkovitch fit.

The indentation behavior of the two specimens is drastically different at low depths, where the annealed specimen is observed to reproducibly emulate the Hertz fit, Equation 6.6, until step-like excursions occur at the depth of 5 nm, Figure 6.4. The as-deposited sample has a load-depth profile essentially parallel to the Berkovitch fit, Equation 6.7, although it becomes offset from this curve at low depths due to the imperfect shape (finite radius) of the experimental indenter tip. For the as-deposited specimen, excursions are not observed, but the loading profile is somewhat irregular. Aberrant behavior is summarized in Table 6.2. In the table, the total number of profiles demonstrating excursions was tallied, taking into consideration events that were (a) occurring at single force (*i.e.* horizontal) during loading segment, (b) rapid or discontinuous in nature (few or no intermittent data points), and (c) greater than 1 nm in depth. For the annealed specimen, some excursions resulted in sudden 5-10 nm penetrations into the material. It should be noted that for the annealed specimen, at least 2/3 of the observed excursions were of the size range between 1-2 nm. For the as-deposited specimen, no excursions larger than ~1 nm were observed. Table 6.2 demonstrates a significantly greater number of excursion events in the annealed specimen, particularly for the slower loading rates. Loading using constant strain rate was particularly helpful in investigating excursion activity, since more data points are recorded near the material's surface, where excursions most frequently occurred.

Table 6.2. Summary of aberrant behavior for as-deposited and annealed specimens. The annealed specimen demonstrated a significantly more frequent number of excursion events, particularly at slower loading rates.

THERMAL TREATMENT	STRAIN RATE {Hz}	# EXCURSIONS	# TESTS
AS-DEPOSITED	0.005	1	12
	0.010	1	13
	0.050	0	15
	0.100	1	12
	0.500	0	9
TOTAL		3	61
PERCENT		4.9	

THERMAL TREATMENT	STRAIN RATE {Hz}	# EXCURSIONS	# TESTS
ANNEALED 177 DEG C	0.005	9	12
	0.010	8	13
	0.050	9	15
	0.100	5	15
	0.500	2	15
TOTAL		33	70
PERCENT		47.1	

Representative modulus and contact pressure (universal hardness) are shown in Figure 6.5 and Figure 6.6 for an as-deposited and annealed specimen, respectively.

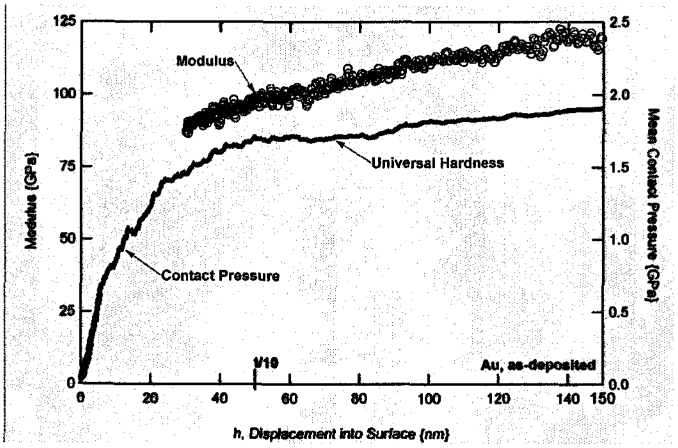

Figure 6.5. Modulus and contact pressure/universal hardness for as-deposited specimen, characterized to deeper depths. Elastic modulus of the specimen is shown only after it has converged to a stable behavior trend.

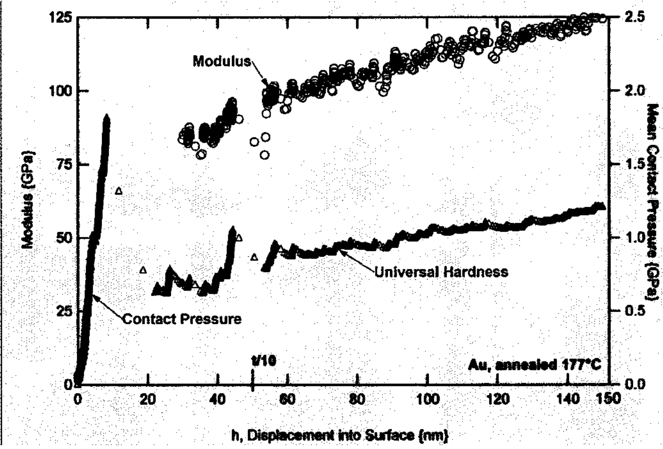

Figure 6.6. Modulus and contact pressure/universal hardness for specimen, annealed at 177 °C. This specimen demonstrates discrete activities (drops in pressure/hardness) near its surface. Elastic modulus of the specimen is shown only after it has converged to a stable behavior trend.

The nomenclature "contact pressure" is used at low indentation depths where hardness is inappropriate in a classical sense. At larger depths, where permanent impressions will result from the indentation testing, the nomenclature "universal hardness" is used. The mean contact pressure and universal hardness are both defined by force divided by instantaneous contact area, Equation 6.4, although the term hardness can be misleading at ultra low depths where samples deform only elastically and the force divided by the projected area approaches at zero as the applied load is decreased towards zero. Both specimens were indented at a constant strain rate of 0.050 s^{-1}, however the particular tests in Figure 6.5 and Figure 6.6 are different than those shown in Figure 6.3 and Figure 6.4. Upon converging to a stable behavior trend at 30 nm, the tip is thought to be properly engaged to the surface, after which the modulus of each specimen is observed to steadily increase (as shown). The measured moduli are nearly identical for both specimens, Figure 6.5 and Figure 6.6. However, differences between the contact pressure/universal hardness are much more significant. For the as-deposited specimen, Figure 6.5, contact pressure is seen to increase until a stable behavior trend is observed at 40 nm. At this point hardness is seen to slightly increase, but remains relatively constant. For the annealed specimen, Figure 6.6, contact pressure is seen to very sharply increase upon initial surface contact. At 10 nm, the contact pressure suddenly decreases at the same depth that an excursion is observed in the loading profile. Contact pressure for the annealed specimen increases once again, until dropping off suddenly at 45 nm into the surface. Beyond this depth, the hardness of the material becomes more constant, but is notably lesser than that of the as-deposited specimen. Note that during the initial contact, Figure 6.6, the universal hardness, Equation 6.4, might be considered a lower limit of the mean stress, whereas the Hertzian mean stress, Equation 6.8, might be considered an upper limit of the mean stress (only universal hardness, Equation 6.4, is shown in Figure 6.6).

Indentation results for all loading rates, Equation 6.1, are averaged and summarized in Table 6.3.

Table 6.3 Summary of indentation parameters for the as-deposited and annealed specimens. Note that modulus and hardness depend on the tip area calibration, whereas the other parameters do not. Standard deviations are 1 σ.

THERMAL TREATMENT		MODULUS	HARDNESS, UNIVERSAL	C1, LOADING	n1, LOADING	Kexp, LOADING	RETAINED ENERGY RATIO	PILE-UP/ SINK-IN RATIO
		{GPa}	{GPa}	{uN}	{unitless}	{GPa}	{%}	{%}
AS-RECEIVED	AVG	106.0	2.1	0.70	1.54	74.3	85.0	80.7
	ST DEV	12.9	0.1	0.37	0.12	24.4	1.3	6.3
ANNEALED 177 DEG C	AVG	101.3	1.7	0.50	1.56	52.7	89.0	86.7
	ST DEV	6.0	0.1	0.19	0.06	9.6	1.4	4.4

The parameters of specimen modulus and hardness are known to depend on the tip's area calibration, Equation 6.2 and Equation 6.4, whereas the other parameters in Table 6.3 may be obtained independent of the tip calibration. The power law fit ($P=C_1h^{n1}$) and Kexp values [42] are obtained from the loading profile. The power law and Kexp values are both influenced by elastic as well as plastic activity occurring during indentation. Kexp may specifically be utilized to decompose the loading profile between elastic and plastic contributions. Note that Kexp should not be confused with the specimen- or machine-compliance. Next, the retained energy ratio and pile-up/sink-in ratio are listed in Table 6.3. The elastic energy during indentation may be determined from the area under unloading profile, whereas the total energy of indentation may be obtained from the area under loading profile. The retained energy ratio is therefore compares the difference between the total elastic and total energy relative to the total energy. Lastly, the pile-up/sink-in ratio (h_f/h_{max}) [27] is given in Table 6.3. The values are greater than 0.7, suggesting that some pile-up may occur during indentation, particularly for the annealed specimen.

One curious result concerns the tip displacement occurring during the hold at maximum load, Table 6.4.

Table 6.4. Summary of universal hardness and displacement during the hold at maximum load at the various applied strain rates. Slightly greater hardness as well as more obviously increased displacement during the creep hold are seen for faster strain rates.

THERMAL TREATMENT	STRAIN RATE	HARDNESS, UNIVERSAL	DISPLACEMENT, CREEP SEGMENT
	{Hz}	{GPa}	{nm}
AS-RECEIVED	0.005	1.9	1.9
	0.010	2.2	2.5
	0.050	2.1	4.4
	0.100	2.1	5.3
	0.500	2.3	9.1
ANNEALED 177 DEG C	0.005	1.8	1.6
	0.010	1.5	2.0
	0.050	1.6	4.0
	0.100	1.6	4.5
	0.500	1.8	7.2

In the table, there is an obvious trend that occurs according to the loading rate. That is, the displacement occurring during the "creep hold" at maximum load increases as the indentation loading rate is increased. This trend is true for both the as-deposited as well as the annealed specimens, being slightly more pronounced for the as-deposited specimen. For the same data, hardness does not strongly vary according to the loading rate, Table 6.4.

Lastly, the retained energy, Table 6.3, is more fully explored in Figure 6.7. In this case, sets of 15 indentations were performed to various specified depths, including 60 nm. In Figure 6.7, a difference between the as-deposited and annealed specimens is seen between the depths of 10 and 70 nm. In this range, the annealed specimen is "more plastic" than the as-deposited specimen, *i.e.* retains a greater amount of the total energy of indentation. At small indentation depths the trend is reversed, the as-deposited specimen retains more energy and thus is more plastic. Figure 6.7 also indicates the key locations for convergence and utility of the various indentation parameters for the Au thin films. For the annealed specimen, the Hertz fit (Equation 6.6) may be used to about 5-10 nm into its surface. Parameters of modulus, hardness, P/S^2 [43], retained energy ratio, pile-up/sink-in ratio, and K converge to stable trends at the indicated depths, Figure 6.7. Not all of the parameters converge at the same depth. Note that P/S^2 is another parameter that is independent of the area calibration for the indenter tip. For both specimens, the loading profile becomes parallel to the Berkovitch fit, Equation 6.7, at about 45 nm. In Figure 6.7, the elastic parameters are seen to converge first, while the plastic and then combined parameters (those depending on both modulus and hardness) converge next. A similar series of events was observed in the fused silica calibration standard, except that the series of convergence activities occurred at greater depths in this ceramic material.

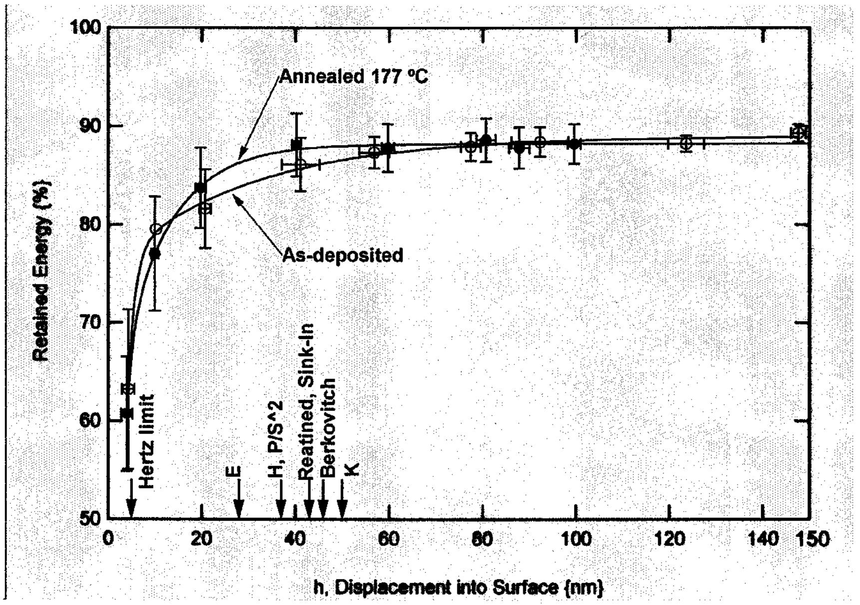

Figure 6.7. Comparison of retained energy, i.e. inelastic deformation, for as-deposited and annealed specimens. Difference in retained energy is observed between 10 and 70 nm into the specimens. Depth locations at which key parameters converge to stable behavior trends are indicated at the appropriate depths.

6.5 Discussion

The experimental results indicate a difference in hardness between the as-deposited and annealed specimens, Table 6.3. At the depth of 60 nm, the greater hardness for the as-deposited specimen might be attributed to its smaller grain size. The grain-size strengthening phenomenon [44,45] is commonly associated with enhanced mechanical strength, for example based on dislocation pile-up at grain boundaries. Grain boundaries are more abundant in smaller grained materials, explaining the greater strength in the as-deposited material. In the literature [3,4,9,10,12,13] grain size strengthening is used to explain the enhanced yield or flow stresses for thin film materials, where the grain size typically falls within the range of the Hall-Petch regime. Based on the Tabor approximation [46], the flow stress of a metal at 8-10% strain can be taken as 1/3 of its indentation hardness. Others have since suggested that the Tabor approximation underestimates the plastic strength, for example when pileup occurs at the indenter tip in non-work hardening materials [47,48]. Therefore, the values of 700 and 566 MPa might be considered a conservative (lower bound) estimate of flow stress for the as-deposited and annealed films, respectively. It should be noted that if the indentation profiles for the annealed specimen not exhibiting excursions are excluded, then the material hardness would be ~ 1.4 GPa, i.e. σ_o, 10% = 466 MPa. All σ_o values mentioned are notably higher than that of bulk gold ~ 120 MPa [48], as might be expected from the grain-size strengthening theory. Note also that the aforementioned σ_o values are greater than the thermally induced stresses observed in previous work [25], further suggesting that dislocation based plasticity was not involved inelastic behavior observed in those thermo-mechanical microcantilever tests. While the values in Table 6.3 confirm conventional wisdom regarding grain size strengthening, Figure 6.3 suggests the results are much more complicated since the hardness values vary according to indentation depth.

Closer examination reveals that, at indentation depths near the specimen surface, greater contact force is required to deform the annealed specimen than the as-deposited specimen, Figure 6.4. For the annealed specimen, contact pressure, as well as Hertzian analysis, Equation 6.8, suggests that the stresses present often increase to within the range from 2 to 7.6 GPa, towards the theoretical limit, *i.e.* 15.3 GPa [5]. On the other hand, maximum contact pressure or Hertzian stress is not seen to exceed 2 GPa for the as-deposited specimen. Therefore, while no plastic flow has yet developed in the annealed specimen, it might be argued that it has a greater load capacity or is more resistant to permanent deformation at initial penetration depths than the as-deposited specimen. Furthermore, the indentation profiles are seen to intersect at 10-30 nm, and beyond this depth the as-deposited specimen requires greater contact force for equivalent indentation depth. When the area of the tip is considered, it is seen that there is a drastic decrease in contact pressure for the annealed specimen between 15 and 20 nm into its surface, Figure 6.6. Additionally, the retained energy for the annealed specimen is seen to exceed that of the as-deposited specimen between a penetration of 10 and 70 nm into its surface, Figure 6.7, suggesting a greater capacity for inelastic deformation. All sources of information therefore indicate that the "hardness" of the annealed specimen has drastically decreased, being less than that of the as-deposited specimen. It should be noted that at these depths the contact pressure measurements are subject to the tip area calibration, however the loading profile (force) and retained energy are not. Lastly, the hardness of the annealed specimen is seen to increase for continued indentation becoming parallel to that of the as-deposited specimen as well as the ideal Berkovitch fit, Figure 6.3. In addition, the retained energy of the annealed specimen is seen to converge and become equal to the as-deposited specimen at greater depths, Figure 6.7. Therefore, it might be said that at greater depths the annealed specimen becomes stronger and of more similar hardness to that of the as-deposited specimen. In summary, the indentation of the annealed specimen is extremely complicated, as the material is initially very "hard" at low indentation depths, becomes softened at moderate indentation depths, and finally hardens during large depth indentation.

Similar evolution of material hardness during indentation was recently reported in the literature [9]. This study focused on thin gold films, except fabricated in multiple batches with varying thickness and grain size. This study also considered the indentation location, relative to the grains boundaries of the material. First, Lilleodden and Nix found that indentation performed adjacent to grain boundaries resulted in a decrease in the maximum load prior to excursion activity, *i.e.* decreased "hardness". This decrease in sustainable applied load was attributed to the grain boundaries, which were seen in atomistic simulations to act as dislocation sources [5]. In our case, no particular attention could be paid to grain boundaries, since they could not be identified (overt grain boundary grooving occurs in our films only at more elevated temperatures, and also in conjunction with inter-diffusion of chemical species [25]). Based on the SEM observations (Figure 1), however, one can analyze the average number of grains in contact with tip during indentation of the as-deposited and annealed specimens studied here, Figure 6.8.

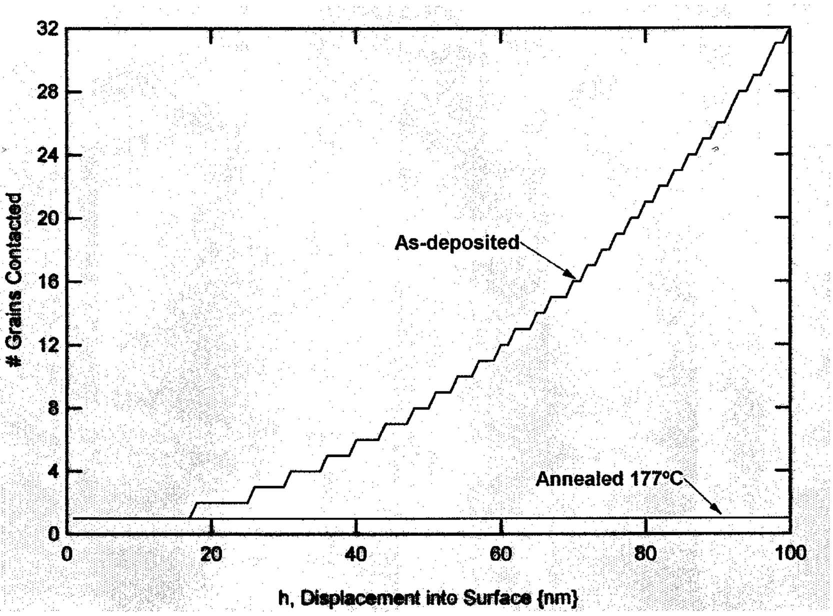

Figure 6.8. Average number of grains in contact with the indenter tip at various depths for the as-deposited and annealed specimens. Grain diameter of 0.1 and 1.0 μm were assumed for the respective specimens, representing a typical grain in the as-deposited specimen and an abnormal grain in the annealed specimen.

To estimate the number of grains in contact with the indenter tip, the area of contact, Equation 6.5, was divided by the area occupied by a 0.1 or 1 μm diameter circle, representing a typical grain in the as-deposited specimen or an abnormal grain in the annealed specimen, respectively. A stark difference exists between the two specimens, where many grains are contacted in the as-deposited film and only 1 grain is typically contacted in the annealed film. Therefore, while not studied explicitly here, there is a significantly greater chance that the indenter tip is outside the proximity of grain boundaries (a defect source) in the annealed specimen.

We show complex depth dependent hardness evolution as well as the advent of excursion activity using material made from the *same* fabrication batch given different heat treatments. The evolution of material hardness can be attributed to the population of defects in the gold specimens [9]. At first, for the annealed specimen, few (or no) dislocations are present, but may become generated through applied loading. In this first regime, Figure 6.9, the material deforms only elastically and may sustain very significant stress (very high contact pressures) prior to dislocation nucleation.

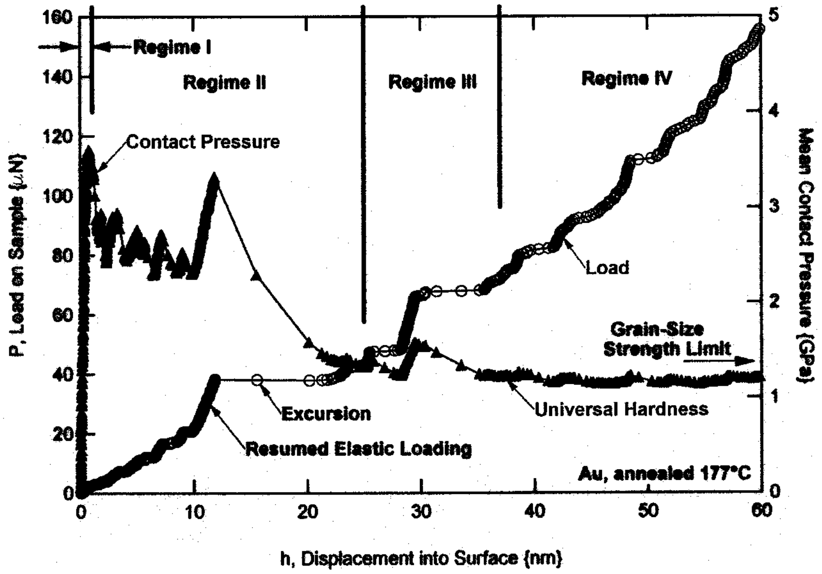

Figure 6.9. Data comparison (load- and contact pressure/universal hardness vs. depth) for annealed specimen, indented again at 0.050 s^{-1}. In Regime I deformation is purely elastic, followed by "softening" (defect formation and propagation) in Regime II, defect accumulation in Regime III, and continued hardening towards the grain size limit in Regime IV. Briefly resumed elastic loading may occur in Regimes II and III, often followed by excursion(s).

Proximity to dislocation sources, such as grain boundaries, surface defects (pores, steps), and internal defects can limit the depth of the initial elastic loading regime. Regime I may end suddenly, which is often indicated by an excursion on the load-depth curve. While not examined explicitly, we believe the aberrant behavior in our study is predominantly associated with line defects. Once dislocations have formed, few such defects are present in the material, and the dislocations propagate readily. In Regime II, Figure 6.9, "hardness" is suddenly diminished or may gradually decrease as defects rapidly advance into the material, motivated by applied loading, annihilation of oppositely-oriented defects, or short-range repulsion (strain fields in the lattice between similarly oriented defects). Depending on the geometry, the material may retain some of its initial hardness as the result of dislocation starvation [8]. In Regime III, Figure 6.9, defect density increases, while at the same time defects become impeded by the grain boundaries. For the third regime, flow stress typically varies in proportion to the square root of dislocation density, as popularized by Taylor and others [32]. The material is therefore hardened as the defect density is increased. Lastly, within Regimes II and III, defect evolution may become less prominent, and the loading may temporarily seem predominantly elastic. For this "resumed elastic loading", typically terminated by aberrant behavior, the indentation (P/h) profile will parallel the Hertzian fit, and the hardness profile will notably increase.

Resumed elastic loading might occur if defects suddenly escape or become annihilated [8]. Perhaps more likely in Figure 6.9, the indenter tip itself or its corresponding and more sizeable strain field come to affect fresh, adjacently located grains. Note also that in Regimes II and II that excursions may occur in association with the spontaneous generation of defects and not just the resumed elastic loading. In Regime IV, Figure 6.9, back-stresses, entanglement, or pileup eventually inhibit defect activity. For most thin films, the defect population becomes limited by grain size, and hardness is achieved as might be predicted by Hall-Petch[1]. Note that the applied strain field exceeds the area of contact, Equation 6.5, therefore the number of grains stressed is underrepresented in Figure 6.8. In very thin films, defect population might also become limited if dislocations are forced up against the substrate interface. It is worth noting that in Regime IV the indentation may affect multiple grains (boundaries) and that the thickness of the film is finite, therefore strain-gradient indentation size effect common to large single crystals deformed to large indentation depths is not realized for thin films. The process of dislocation formation may, however, very much contribute to the indentation size effect observed in larger specimens, where the process is not as limited by the specimen's own volume. Lastly, the effected specimen volume in Regime IV will tend to average out (minimize) resumed elastic loadings as well as excursions because the relative amount of fresh material becomes increasingly smaller as indentation is continued.

While the four regimes described above provide a physical explanation for the variation in hardness observed during indentation, some important details have not yet been considered. First, the interaction between defects and the free surface have not been considered. Gold is a material that can sustain little more than a monolayer of native oxide [50]. A more robust surface oxide may act as a redistributor of the applied load as well as an inhibitor of defect evolution. It is less clear how factors such as surface free-energy, surface chemistry/diffusion, or contamination (discrete particles or monolayers) influence indentation hardness at the small depths performed here, if at all. Surface texture and defects (pores or steps) may influence indentation hardness, particularly if they affect the true contact area at the tip. For example, the unevenness in the loading profile for the as-deposited specimen may result from the crushing of individual surface asperities (nodules), which should become less influential as the depth (sample volume) of indentation increases. At shallow depths, the true shape of the tip, convoluted with the local surface misalignment, may be even more significant than surface morphology. Still, the (partially) annealed specimen demonstrated excursion activity even though the specimen itself was not subject to careful surface preparation, i.e. mechanical polishing followed by annealing, followed by electro-chemical polishing.

In addition to surface features, the influence of point defects has not yet been considered. Recall that vacancy clusters have recently been linked to incipient plasticity [23]. Thin

---

[1] Using the σ_o, 10% values as σ_y and corresponding grain sizes ("d") for the gold thin film specimens, a Hall-Petch fit [32] yields $\sigma_o = 357.8$ MPa and k = 108.2 MPa $\mu m^{0.5}$. These values are somewhat different than $\sigma_o = 78$ MPa and k = 250 MPa $um^{0.5}$, the Hall-Petch coefficients in [41], obtained based on the *yield* strength of freestanding tensile specimens.

films often contain many excess vacancies as the result of their formation process, e.g. sputtering or evaporation [51,52]. To some extent, our specimens may be dissimilar because excess vacancies, which contribute to dislocation nucleation, may have been removed in the annealing process. Lastly, the presence of pre-existing twins was not considered in the literature [9,23]. From previous work [25], it is known that our specimens contain multiple through-thickness twins in both the as-deposited and annealed condition. The interaction between defects and twins or stacking faults is not well studied in thin film materials. For that matter, the interaction between strain and so-called "annealing" twins, as well as the twins' own deformation mechanisms, have not been studied extensively in the literature. It is unclear, for example, if the twins here will aid (source) or hinder defect activity. In Figure 6.4, for example, it is possible that excursions may occur in association with twin boundary motion. Study of the influence of point defects and twins remains for future work, for example in-situ nanoindentation microscopy studies.

As in the literature for larger indentation volumes [19], our experiments suggest that the hardness of very small volumes exhibits a dependence on loading rate, Table 6.4. Based on the literature [23], the lower applied strain rates might be expected to result in a reduction in maximum load prior to excursion activity. A lesser initial "hardness" for lower applied strain rates is expected because the more prolonged loading duration allows more time for a critical thermal fluctuation (vacancy activity) to occur, facilitating dislocation formation. Indeed, a greater number of excursions was typically seen in the annealed specimen for slower indentation rates, Table 6.2, where the greater loading period increases the likelihood of defect initiation. Once formed, the slower loading rates also allow greater time for the defects to propagate, which is likewise a thermally activated process. Therefore enhanced initiation and propagation of defects are both expected to result in a decreased hardness for slower loading rates. Ignoring the outlying data points at the lesser strain rates, a slight hardness trend was observed, Table 6.4, although the trends are not strong. Decreased displacement during the creep hold for lesser strain rates, Table 6.4, is a more prominent trend believed to be related to thermal activation, which is more likely to have occurred during more prolonged loading periods. The influence of strain rate upon hardness may not be as prominent or it simply may be overwhelmed by other factors, including regions locally populated by many small grains as well as the variability of measurement. It should be noted that a better distinguished correlation (between strain rate, hardness, displacement during the creep hold, and even Kexp) of the type suggested was seen in experiments (not shown here) performed on the near-surface indentation of silver and nickel single crystals. These results suggest that the effect of strain rate extends to very small volumes of material.

As opposed to the hardness measurements, the modulus measurements should be more straightforward. Material modulus is not expected to change in response to annealing unless considerable inter-diffusion of the Au/Cr/Si layers occurs or the preferred crystallographic texture is altered. Therefore the change in the power-law fit parameters

(C_1, nl) as well as Kexp, Table 6.3, are attributed to change in the inelastic behavior of the gold specimens. The measured modulus values of 106.0 ± 12.9 and 101.3 ± 6.0GPa for the as-deposited and annealed specimens are the same, within the range of error. However, the values are more similar to that of <111> oriented gold, *i.e.* 115.3 GPa, than the value predicted by polycrystalline aggregate theory, *i.e.* 77.7 GPa, which might be expected for large sample volumes in single crystals [34]. For comparison, the modulus of gold thin films measured in the literature is 84.9 [1], 111.3 [3] 115 [4], 99.2 [5], 76.5 [6], and 88.6 [7]. Several of these values presented in the literature are also outside of the isostress and isostrain limits (68.4 and 87.0 GPa, respectively [33,37]), and are similar to our values.

To begin with, the extraction of measured parameters at 10% of the thickness is an approximation, and more precise techniques exist for extrapolating the modulus to a material's surface, thereby decoupling a thin film from its substrate [53]. Because the modulus does not converge to a monotonic value, Figure 6.5 and Figure 6.6, the modulus mismatch between the film and substrate is likely present at very shallow depths in both specimens causing the modulus of the film to be overestimated during indentation. Second, some pile-up at the indenter tip is expected, as gold is a soft metal and not prone to work-hardening. Pile-up around the tip would result in a greater area of contact than is anticipated by the measurement technique, therefore modulus and hardness would be exaggerated, Equation 6.2, Equation 6.4. Third, consider also that a tensile residual stress exists within the gold film, which is greatly enhanced by the annealing process [25]. Analysis in the literature suggests the presence of tensile stress in a thin film specimen will reduce its hardness and modulus [54], counteracting the first two effects. Lastly, the anisotropic nature of the thin films may influence the modulus measurements. To begin with, by considering the raw displacement and the lateral space between indents, the surface of the gold was aligned to the axis of loading by 4.6 ± 0.6° and 3.2 ± 0.2° for the as-deposited and annealed specimens, respectively. The <111> primary texture, common to many FCC thin metals films, is the most elastically rigid of the lower order crystallographic orientations, whereas the <001> sub-component is the most compliant [32]. At this point the measured modulus for small indentation volumes has not been studied in great detail for anisotropic single- or poly-crystals, where for example stress and strain may be accommodated grain boundaries of differently oriented grains [55]. The exact contribution of modulus mismatch, pile-up, residual stress, and material anisotropy remains for future research.

6.6 Conclusions

We have studied the sub 100 nm indentation of Au thin films before and after annealing. Key results include:

1. The nominal material hardness was seen to decrease from 2.1 ± 0.1 to 1.7 ± 0.1 GPa after annealing. Discrete loading events (excursions, or "pop-ins") were also seen as the result of annealing the films. Upon closer inspection, the hardness of the gold was found to vary in a complex manner, according to the indentation depth. The depth-dependent variation in hardness (high load capacity, softening, hardening, then size-limited hardness) for the annealed specimen is explained according to its defect structure. For the annealed film, defects must first be generated, then transmitted, until the defect population achieves its limit, based on the grain size or layer thickness. Interaction with other grains of fresh material may manifest itself as "resumed elastic loading" activity followed by excursions, which become less prominent as the sample volume increases. In the as-deposited film, the defect population limit is more readily achieved because of its much smaller grain size and the force required to load the indenter tip increases in a more uniform manner. Also, a greater number of grain boundaries, which may act as defect sources, are immediately contacted for the as-deposited specimen.

2. Variation in hardness as well as displacement during the "creep hold" at maximum load was observed according to the applied strain rate. Also, a greater number of excursions were seen in the annealed specimen for slow loading rates. This demonstrates that the importance of loading rate extends to very small volumes. The prolonged loading period at lesser strain rates statistically favors defect enabling critical thermal fluctuations. Greater hardness and displacement during the creep hold was seen for the faster loading rates. This variation is also thought to be greatly influenced by the population of point defects within the material. Critical thermal fluctuations influence defect generation, *i.e.* initial "hardness", while thermal activation enables defect propagation, *i.e.* continued hardness. The influence of twin defects, regarding depth-dependent hardness or strain rate, is even less understood than point defects.

3. The modulus was found to be 106.0 ± 12.9 and 101.3 ± 6.0GPa for the respective specimens. These values are about 33% greater than the value of 77.7 GPa predicted from the aggregate theory, applicable to large sample volumes. Measured values may be artificially increased by the modulus mismatch with the substrate, pile-up at the indenter tip, the anisotropic film texture, as well as the grain size. Modulus would be expected to be decreased by the tensile stress present in the gold specimens. The impact of the crystallographic texture as well as the extent of contribution from each of these factors for small sample volumes remains for future research.

6.7 Acknowledgements

The authors would like to acknowledge the Analytical Materials Science group at Sandia National Laboratories, including Nancy Yang, Miles Clift, and Jeff Chames for their help with microscopy and further materials characterization. We would like to acknowledge the helpful discussion with Erica Lilleodden and William Nix of Stanford University concerning interpretation of the results, John Jungk of Sandia National Laboratories for discussion of more recent simulation work with James Knapp, as well as Erik Herbert of MTS Systems Corporation concerning the Nano DCM instrument and test procedure.

6.8 References

[1] J.F. Smith, and S. Zheng, "High Temperature Nanoscale Mechanical Property Measurements", Surf. Eng, **16** (2), 2000, pp. 143-146.

[2] T. Ohmura, S. Matsuoka, K. Tanaka, and T. Yoshida, "Nanoindentation Load-displacement Behavior of Pure Face Centered Cubic Metal Thins Films on a Hard Substrate", Thin Sol. Films, **385**, 2001, pp. 198-204.

[3] C. Xie, R.D. Emery, S.Y. Yang, and W. Tong, "Mechanical Properties and Stresses in Thin Gold Films on a Silicon Substrate", Proc. Mat. Res. Soc., **695**, 2002, pp. L52.1-L52.6.

[4] N.R. Moody, D.P. Adams, T. Headley, N. Yang, and A. Volinsky, "Effects of Diffusion on Interfacial Fracture of Gold-Chromium Hybrid", Int. J. Fract, **119** (4), 2003, pp. 407-419.

[5] E.T. Lilleodden, J.A. Zimmerman, S.M. Foiles, and W.D. Nix, "Atomistic Simulations of Elastic Deformation and Dislocation Nucleation During Nanoindentation", J. Mech. Phys. Solids, **51**, 2003, pp. 901-920.

[6] C. San Marchi, N.R. Moody, M.J. Cordill, G. Lucadamo, J.J. Kelly, T. Headley, and N. Yang, "Structure-property Relationships of Au Films Electrodeposited on Ni", Proc. Mat. Res. Soc., **821**, 2004, pp. P2.8.1-P2.8.6.

[7] A.A. Volinsky, N.R. Moody, and W.W. Gerberich, "Nanoindentation of Au and Pt/Cu Thin Films at Elevated Temperatures", J. Mater. Res. **19** (9), 2004, pp. 2650-2657.

[8] W.D. Nix, J.R. Greer, G. Feng, and E.T. Lilleodden, "Deformation at the nanometer and Micrometer Length Scales: Effects of Strain Gradients and Dislocation Starvation", *In press*, Acta Mat.

[9] E.T. Lilleodden, and W.D. Nix, "Microstructural Length-scale Effects in the Nanoindentation Behavior of Thin Gold Films", Acta Materialia, **54** (6), 2006, pp. 1583-1593.

[10] P. Shukla, A.K. Sikder, P.B. Zantye, A. Kumar, and M. Sanganaria, "Effect of Annealing on the Structural, Mechanical, and Tribological Properties of Electroplated Cu Thin Films", Proc. Mat. Res. Soc., **812**, 2004, pp. F3.16.1-F3.16.7

[11] V. Srinivassarao, R. Jayaganthan, V.N. Sekhar, K. Mohankumar, and A.A.O. Tay, "Nanoindentation Study of the Sputtered Cu Thin Films for Interconnect Applications", Proc. IEEE Elect Pack Tech, 2004, pp. 343-347.

[12] J.A. Knapp, and D.M. Follstaedt, "Hall-Petch Relationship in Pulsed-laser Deposited Nickel Films", J. Mater. Res. **19** (1), 2004, pp. 218-227.

[13] A. Shugurov, A. Panin, H.G. Chun, and K. Oskomov, "Surface Morphology, Microstructure and Mechanical Properties of Thin Ag Films", Proc. KORUS, **11**, 2003, pp. 21-29.

[14] R.E. Winter, "Effect of Thickness on the Plastic Deformation of (100) Silver Films", Phil. Mag., **29** (3), 1974, pp. 513-520.

[15] T.F. Page, W.C. Oliver, and C.J. McHargue, "The Deformation Behavior of Ceramic Crystals Subjected to Very Low Load (Nano)indentations", J. Mater. Res. **7** (2), 1992, pp. 450-473.

[16] J.D. Kielly, and J.E. Houston, "Nanomechanical Properties of Au (111), (001), and (110) Surfaces", Phys. Rev. B, **57** (19), 1998, pp. 12588-12594.

[17] D.E. Kramer, K.B. Yoder, and W.W Gerberich, "Surface Constrained Plasticity: Oxide Rupture and the Yield Point Process", Phil. Mag. A, **81** (8), 2001, pp. 2033-2058.

[18] V. Domnich, D. Ge, and Y. Gogotsi, "Indentation-Induced Phase Transformations in Semiconductors", in High-Pressure Surface Science and Engineering, IOP: Philadelphia, 2004.

[19] N. Gane, and J.M. Cox, "The Micro-hardness of Metals at Very Low Loads", Phil. Mag., **22**, 1970, pp. 881-891.

[20] J.B. Pethica, R. Hutchinson, and W.C. Oliver, "Hardness Measurement at Penetration Depths as Small as 20 nm", Phil. Mag. A, **48** (4), 1983, pp. 593-606.

[21] G.M. Pharr, and W.C. Oliver, "Nanoindentation of Silver – Relations Between Hardness and Dislocation Structure", J. Mater. Res., **4** (1), 1989, pp. 94-101.

[22] J.W. Hutchinson, "Plasticity at the Micron Scale", Int. J. Sol. Struct, **37**, 2000, pp. 225-238.

[23] C.A. Schuh, J.K. Mason, and A.C. Lund, "Quantitative Insight into Dislocation Nucleation from High-Temperature Nanoindentation Experiments", Nat. Mat., **41**, 2005, pp. 617-621,

[24] D. Koester, A. Cowen, R. Mahadevan, M. Stonefeild, B. Hardy, Poly-MUMPs Design Rules: Revision 10, MEMSCAP Inc., (2003).

[25] D.C. Miller, C.F. Herrmann, H.J. Maier, S.M. George, C.R. Stoldt, and K. Gall, "Thermomechanical Evolution of Multilayer Thin Films, Part 2: Microstructure Evolution in the Metallic Layers". *Submitted to Thin Solid Films.*

[26] D. L. Joslin and W. C. Oliver, A new method for analyzing data from continuous depth-sensing microindentation tests, J. Mater. Res., **5** (1990) 123-126.

[27] W.C. Oliver and G.M. Pharr, "Measurement of hardness and elastic modulus by instrumented indentation: Advances in understanding and refinements to methodology", J. Mater. Res., 19, 2004, pp. 3-20.

[28] J. H. Strader, S. Shim, H. Bei, W. C. Oliver, and G. M. Pharr, "An Experimental Evaluation of the Constant ß Relating the Contact Stiffness to the Contact Area in Nanoindentation," Proc. Mat. Res. Soc. Symp., **841**, pp. R1.4.1-R1.4.6, 2005.

[29] B.N. Lucas, and W.C. Oliver, "Indentation Power-Law Creep of High Purity Films", Met Trans A, **30**, 1999, pp. 601-610.

[30] G. M. Pharr and W. C. Oliver, "Measurement of Thin-Film Mechanical-Properties Using Nanoindentation," MRS Bulletin, **17**, pp. 28-33, 1992.

[31] T.D. Ridney, "Residual Thermoelastic Stresses in Bonded Silicon Wafers", J. Appl. Phys., **32** (3), 1961, pp. 454-460.

[32] M.A. Meyers, and K.K. Chawla, Mechanical Behavior of Materials New Jersey: Prentice-Hall, 1999, pp. 88-91.

[33] M. Levy, Handbook of Elastic Properties of Solids, Liquids, and Gases: Volume II Elastic Properties of Solids, San Diego: Academic Press, 2001.

[34] J.J. Vlassak, and W.D. Nix, "Measuring the Elastic Properties of Anisotropic Materials by Means of Indentation Experiments", J. Mech. Phys. Solids, **42** (8), 1994, pp. 1223-1245.

[35] J.J. Vlassak, M. Ciavarella, J.R. Barber, and X. Wang, "The Indentation Modulus of Elastically Anisotropic Materials for Indentors of Arbitrary Shape", J. Mech. Phys. Solids, **51**, 2002, pp. 1701-1721

[36] J.A. Knapp, D.M. Follstaedt, S.M. Myers, J.C. Barbour, T.A. Friedmann, „Finite-Element Modeling of Nanoindentation", J. Appl. Phys., **85** (3), 1999, pp.1460-1474.

[37] R. Hill, "The Elastic Behavior of Crystalline Aggregate", Proc. Phys. Soc. A **65** (389), 1952, pp. 349-354.

[38] R. Nowak, and M. Sakai, "The Anisotropy of Surface Deformation of Sapphire: Continuous Indentation of Triangular Indenter", Acta. Mat., **42** (8), 1994, pp. 2879-2891.

[39] A. Fischer-Cripps, Nanoindentation. New York: Springer, 2002.

[40] K.L. Johnson, Contact Mechanics, Cambridge: Cambridge University Press, 1985.

[41] R.D. Emery and G.L. Povirk, "Tensile Behavior of Free-Standing Gold Films. Part I. Coarse Grained Films", Acta. Mat., **51**, 2003, pp. 2067-2078.

[42] M. R. McGurk and T. F. Page, "Using the P-δ2 Analysis to Deconvolute the Nanoindentation Response of Hard-coated Systems, J. Mater. Res., **14**, 1999, pp. 2283-2295.

[43] T.F. Page, G.M. Pharr, J.C. Hay, W.C. Oliver, B.N. Lucas, E. Herbert, and L. Riester, "Nanoindention Characterization of Coated Systems: P:S2 – A New Approach Using The Continuous Stiffness Technique", Proc. Mat. Res Soc., **522**, 1998, pp. 53-64.

[44] E.O. Hall, Proc. Phys. Soc. B, **64**, 1951 pp. 742-747.

[45] N.J. Petch, JISI, **173**, 1953, pp. 25-28.

[46] D. Tabor, The Hardness of Materials, Oxford: Claredon Press, 1951, pp. 174.

[47] A. Bolhshakov and G.M. Pharr, "Influence of Pileup on the Measurement of Mechanical Properties by Load and Depth Sensing Indentation Techniques", J Mater. Res., **13** (4), 1998, pp. 1049-1058.

[48] http://www.matweb.com

[49] Y.T. Cheng, and C.M. Cheng, "What is Indentation Hardness?", Surf. Coat. Tech., **133-134**, 2000, pp. 417-424.

[50] H.N. Wagar in W. Everitt, Integrated Device and Connection Technology, Volume III Prentice-Hall: Englewood Cliffs 1971 pp. 469-473.

[51] R. Mitra, R.A. Hoffman, A. Madan, and J.R. Weertman, "Effect of Process Variables on the Structure, Residual Stress, and Hardness of Sputtered Nanocrystalline Nickel Films", J. Mater. Res., **16** (4), 2001, pp. 1010-1027.

[52] R.E. Winter, "Effect of Thickness on the Plastic Deformation of (100) Silver Films", Phil. Mag, **29** (3), 1974, pp. 513-520.

[53] J. Mencik, D. Munz, E. Quandt, and E.R. Weppelmann, "Determination of Elastic Modulus of Thin Layers Using Nanoindentation", J. Mater. Res., **19** (9), 1997, pp. 2475-2484.

[54] K.F. Jarausch, J.D. Kiely, J.E. Houston, and P.E. Russell, "The Correlation of Stress-State and Nano-Mechanical Properties in Au", Proc. Mat. Res. Soc. Symp., **522**, 1998, pp. 119-124.

[55] S.P. Baker, A. Kretschman, and E. Artz, "Thermomechanical Behavior of Different Texture Components in Cu Thin Films", Acta. Mat., 49, 2001, pp. 2145-2160.

Distribution

External:

Prof. Ken Gall
Love Bldg., Room 282
School of Materials Science and Engineering
Georgia Institute of Technology
Atlanta, GA 30332-0250

Prof. Martin L. Dunn
Department of Mechanical Engineering
University of Colorado at Boulder
427 UCB
Boulder, CO 80309-0427

Prof. Philip Gullett
Mailstop 9546
Walker Bldg., Rm 235 M
Mississippi State University
Mississippi State, MS 39762

Prof. Mark F. Horstemeyer
Mailstop 9552
Carpenter Engineering Bldg, Rm 206
Mississippi State University
Mississippi State, MS 39762

Prof. David L. McDowell
MRDC, Room 4105
George W. Woodruff School of Mechanical Engineering
Georgia Institute of Technology
Atlanta, GA 30332-0250

Internal:

1	MS 0372	J. Pott, 1524
1	MS 0372	D.C. Hammerand, 1524
1	MS 0380	H.S. Morgan, 1540
1	MS 0824	W.L. Hermina, 1510
1	MS 0825	C.W. Peterson, 00003
1	MS 0847	J.M. Redmond, 1526
1	MS 0886	J.V. Cox, 1526
1	MS 0888	R.S. Chambers, 1526
1	MS 0888	E.D. Reedy Jr., 1526

1	MS 1070	P.L. Reu, 1526
1	MS 1070	H. Sumali, 1526
1	MS 1303	G.S. Grest, 1114
1	MS 1322	J.B. Aidun, 1435
1	MS 1411	H.E. Fang, 1814
1	MS 1411	C.C. Battaile, 1814
1	MS 1411	M.E. Chandross, 1814
1	MS 1411	S.M. Foiles, 1814
1	MS 1411	A.L. Frischknecht, 1814
1	MS 1411	E.A. Holm, 1814
1	MS 1411	J.J. Hoyt, 1814
1	MS 1411	D. Olmsted, 1814
1	MS 1411	V. Tikare, 1814
1	MS 1411	E.B. Webb III, 1814
1	MS 1415	C. Gutierrez, 1114
1	MS 1415	P.J. Feibelman, 1114
1	MS 1415	J.E. Houston, 1114
1	MS 1415	J.W.P. Hsu, 1114

1	MS 9001	P.J. Hommert, 8000
1	MS 9001	P.A. Spence, 8000
1	MS 9004	J.M. Hruby, 8100
1	MS 9035	W.R. Even Jr., 8220
1	MS 9042	A.A. Brown, 8774
1	MS 9042	E.P. Chen, 8776
1	MS 9042	D.J. Bammann, 8776
1	MS 9042	J.W. Foulk III, 8776
10	MS 9042	J.A. Zimmerman, 8776
1	MS 9161	A.E. Pontau, 8750
1	MS 9161	S.W. Allendorf, 8756
1	MS 9161	I. Arslan, 8756
1	MS 9161	N.C. Bartelt, 8756
1	MS 9161	J.C. Hamilton, 8756
1	MS 9161	E. Marquis, 8756
1	MS 9161	K.F. McCarty, 8756
1	MS 9161	D.L. Medlin, 8756
1	MS 9161	J.P. Pierce, 8756
1	MS 9161	R.R. Stumpf, 8756
1	MS 9161	J.L. Lee, 8759
1	MS 9161	F. Leonard, 8759
1	MS 9401	A.A. Talin, 8759
1	MS 9402	J.E.M Goldsmith, 8772
1	MS 9402	N.R. Moody, 8758

1	MS 9402	K.A. Nibur, 8758
1	MS 9402	J.D. Puskar, 8758
1	MS 9402	C.W. San Marchi, 8758
1	MS 9402	B.P. Somerday, 8758
1	MS 9402	N.Y.C. Yang, 8758
1	MS 9402	X. Zhou, 8776
1	MS 9403	T.J. Shepodd, 8778
1	MS 9403	S.H. Goods, 8758
1	MS 9404	D.M. Kwon, 8770
1	MS 9405	R.W. Carling, 8700
1	MS 9405	S. Aubry, 8776
1	MS 9405	T.D. Nguyen, 8776
1	MS 9409	R.E. Jones, 8776
1	MS 9409	C.D. Moen, 8757
1	MS 9409	G.J. Wagner, 8757
2	MS 0899	Technical Library, 4536
2	MS 9018	Central Technical Files, 8944
1	MS 0123	D. Chavez, LDRD Office, 1011